



CHALMERS
UNIVERSITY OF TECHNOLOGY



Structural Optimization of Mechanical Systems

Topology optimization with parametrization of hardpoint positions

Master's thesis in Applied Mechanics

Aliki Berndtsson
Andreas Mattiasson

MASTER'S THESIS 2019

Structural Optimization of Mechanical Systems

Topology optimization with parametrization of hardpoint positions

ALIKI BERNDTSSON
ANDREAS MATTIASSON



CHALMERS
UNIVERSITY OF TECHNOLOGY

Department of Industrial and Materials Science
Division of Material and Computational Mechanics
CHALMERS UNIVERSITY OF TECHNOLOGY
Gothenburg, Sweden 2019

Structural Optimization of Mechanical Systems
Topology optimization with parametrization of hardpoint positions
ALIKI BERNDTSSON
ANDREAS MATTIASSON

© ALIKI BERNDTSSON, 2019.
© ANDREAS MATTIASSON, 2019.

Supervisor: Robin Larsson, Volvo Cars
Examiner: Martin Fagerström, Department of Industrial and Materials Science

Master's Thesis 2019
Department of Industrial and Materials Science
Division of Material and Computational Mechanics
Chalmers University of Technology
SE-412 96 Gothenburg
Telephone +46 31 772 1000

Cover: Wheel suspension system of the the second generation Volvo XC90.

Typeset in L^AT_EX
Printed by Reproservice
Gothenburg, Sweden 2019

Structural Optimization of Mechanical Systems
Topology optimization with parametrization of hardpoint positions
ALIKI BERNDTSSON
ANDREAS MATTIASSON
Department of Industrial and Materials Science
Chalmers University of Technology

Abstract

This is the report for a master's thesis project on structural optimization of mechanical systems, at Volvo Cars. The shift towards electric propulsion and high cost of battery capacity puts further need for lightweighting since it can bring significant cost advantages in terms of price per range. Topology Optimization (TO) is a method that finds its true potential in context with additive manufacturing due to high level of design freedom, but it can also be beneficial in context with other manufacturing techniques such as casting. Previous thesis projects at Volvo Cars have emphasized TO in the context of casted components and it is widely used today. However, TO is often used to refine the geometry relatively late and applied to single components with predetermined boundary conditions such as joint loads and joint positions, i.e. constraints that narrows the solution space. The main idea for this project is therefore to broaden the solution space by introducing TO on system level together with an outer parametric loop for joint positions. This method can be applied to mechanical systems in general, but the main focus is to provide a prestudy for applications within automotive wheel suspension systems.

A Finite Element (FE) model of a rear wheel suspension system is developed and validated with respect to force signals from an existing, dynamic, full vehicle model. The linkages are then optimized with respect to stiffness and weight based on current joint positions. The proposed scheme for parametrization of joint positions is limited to a two-component system.

Over all, the FE-model correlates well with respect to force signals, but there are still room for improvements, especially with respect to modeling of dampers. In order to introduce proper stiffness constraints during optimization, there is also a need for correlation of the FE-model with respect to displacements. The future potential for TO on system level seems promising. In addition to a broader solution space through parametrization of joint positions the relative mass distribution between different components are treated within one single system optimization.

Keywords: Structural optimization of a multibody systems, Topology optimization, Parametrization of joint positions.

Acknowledgements

The report consists of documentation from a Matser's thesis project at Volvo Cars. The work was carried out during the spring of 2019, by two students from the master program in Applied Mechanics at Chalmers University of Technology.

We would like to thank our supervisor Robin Larsson for great support during the entire project, Joakim Zakrisson for support regarding Road Load Data and Åsa Sällström as well as the rest of the group *CAE Body, Chassis and RLD* for good input during the project. Furthermore, a great thanks to Anton Jurinic from Dassault Systèmes for a nice introduction course in Tosca Structure.

Last but not least, we would also like to thank our optimization guru Harald Hasselblad, our examiner Martin Fagertröm and our manager Per Sjövall for believing in this project and for recognizing the potential of system level optimizations.

Aliki Berndtsson & Andreas Mattiason, Gothenburg, June 2019

Contents

List of Figures	xi
List of Tables	xv
1 Introduction	1
1.1 Background	1
1.1.1 Earlier studies	3
1.2 Aim	3
1.3 Limitations	4
1.4 Specification of issue under investigation	4
2 Theory	7
2.1 Technological platforms	7
2.2 Finite Element Method	10
2.2.1 Strong format	10
2.2.2 Weak format	11
2.2.3 FE-format	11
2.3 Topology Optimization	12
2.3.1 TO example: Minimum compliance using SIMP	12
2.3.2 TO in Tosca	13
2.4 FE-modeling in Abaqus	14
2.4.1 Connector elements	14
2.4.2 Coupling constraints	14
3 Methodology	15
3.1 Prestudy	16
3.1.1 Strength events	16
3.2 Finite Element Analysis	16
3.2.1 FE-model	16
3.2.1.1 Bushing attachments and material models for com- ponents	17
3.2.1.2 Steel sheet components	17
3.2.1.3 Aluminum cast components	18
3.2.1.4 Boundary conditions	18
3.2.1.5 Assembly	19
3.2.1.6 Linear elastic bushing characteristics	19
3.2.1.7 Damper loads	19

3.2.1.8	Drawing state loads and pretension forces	20
3.2.2	Verification with respect to force signals	21
3.2.3	Sensitivity Analysis: Bushing Stiffness	21
3.2.4	Sensitivity Analysis: Component Stiffness	22
3.3	Structural Optimization	22
3.3.1	Two-component problem	22
3.3.2	TO of the wheel suspension system	24
3.3.2.1	Design volumes of the linkages	24
3.3.2.2	Concept load cases	25
3.3.2.3	Topology optimization configuration	25
4	Results	27
4.1	Verification of FE-model	27
4.1.1	Force signals with poor correlation	30
4.1.2	Static analysis and dynamic events	31
4.1.3	Sensitivity analysis: Bushing stiffness	32
4.1.4	Sensitivity analysis: Component stiffness	35
4.2	Structural Optimization	36
4.2.1	Optimization of the two-component model	36
4.2.2	TO of the wheel suspension system	38
4.2.2.1	Case 1	39
4.2.2.2	Case 2	40
5	Discussion	43
5.1	FE-model of the wheel suspension system	43
5.1.1	Rigid bushing attachments	43
5.1.2	Quasi-static analysis with linear assumptions	44
5.1.3	Boundary conditions and bushing stiffness	44
5.2	TO on system level	45
5.2.1	Load distribution during optimization	46
5.2.2	Optimization strategies	46
6	Conclusion	47
6.1	Further work	48
	Bibliography	49
A	Linearization of bushing characteristics	I
B	Results from verification of FE-model	V
C	Results from sensitivity analysis: bushing stiffness	XXIII
D	Additional Results from TO of the system model	XXV
E	Proposed workflow for development	XXVII

List of Figures

1.1	Proposed scheme	2
1.2	Current workflow	2
2.1	Five links constraining one DoF each	7
2.2	The studied rear wheel suspension system; an integral link rear axle, viewed from behind	8
2.3	System components and hardpoints for linkages	9
2.4	Bushing	9
2.5	Loaded body and kinematically admissible displacements	10
3.1	Overview of project and methodology	15
3.2	Snapshots from studied strength events	16
3.3	Toelink	17
3.4	UCA	17
3.5	Subframe	17
3.6	LCA	18
3.7	Knuckle	18
3.8	Boundary conditions similar to a chassis rig test fixture	18
3.9	Assembly and global reference frame	19
3.10	Damper force	20
3.11	Pretension forces from the leaf spring at drawing state	20
3.12	Two-component model: Problem definition and Abaqus FE-model	23
3.13	Linkages as design volumes	24
3.14	LCA design volume	24
3.15	UCA design volume	24
3.16	Toelink design volume	24
4.1	Force signals in HP6 during BIP, FE-model (— —) vs RLD (—)	27
4.2	High RMS ^{norm} : BIP and DOC, FE-model (— —) vs RLD (—)	30
4.3	High RMS ^{norm} : SAC, FE-model (— —) vs RLD (—)	30
4.4	Non-physical deflections caused by peak damper loads during DOC	31
4.5	F_z^{RH} for DOC: HP12 and 14, FE-model (— —) vs RLD (—)	31
4.6	System response of bushing stiffness in HP 3 local y-direction	33
4.7	System response of bushing stiffness in HP 31-32 local y-direction	34
4.8	Change in peak force in HP4 for DOC when changing the stiffness of the LCA	35
4.9	Performance plot: Minimize mass (rigid bushings)	36

4.10	Topology evolution: Minimize mass (rigid bushings)	36
4.11	Performance plot: Minimize mass (flexible bushings)	37
4.12	Topology evolution: Minimize mass (flexible bushings)	37
4.13	Strain energy	38
4.14	Tip Displacement	38
4.15	Topology evolution: Minimize strain energy (flexible bushings)	38
4.16	Topology of the optimized components for case 1 with all load cases, BIP, DOC and SAC	40
4.17	Topology of the optimized components for case 2 with all load cases, BIP, DOC and SAC	41
5.1	Straight UCA	45
5.2	Boundary for hardpoint position during parametric optimization	45
A.1	Bushing characteristics: HP1 & 7, FE-model (— —) vs RLD (—)	I
A.2	Bushing characteristics: HP3, FE-model (— —) vs RLD (—)	II
A.3	Bushing characteristics: HP4, FE-model (— —) vs RLD (—)	II
A.4	Bushing characteristics: HP12 & 14, FE-model (— —) vs RLD (—)	III
A.5	Bushing characteristics: HP18, FE-model (— —) vs RLD (—)	III
A.6	Bushing characteristics: HP31 & 32, FE-model (— —) vs RLD (—)	IV
A.7	Bushing characteristics: HP33 & 34, FE-model (— —) vs RLD (—)	IV
B.1	F^{norm} in HP1 during BIP, FE-model (— —) vs RLD (—)	VI
B.2	F^{norm} in HP3 during BIP, FE-model (— —) vs RLD (—)	VI
B.3	F^{norm} in HP4 during BIP, FE-model (— —) vs RLD (—)	VII
B.4	F^{norm} in HP6 during BIP, FE-model (— —) vs RLD (—)	VII
B.5	F^{norm} in HP7 during BIP, FE-model (— —) vs RLD (—)	VIII
B.6	F^{norm} in HP12 during BIP, FE-model (— —) vs RLD (—)	VIII
B.7	F^{norm} in HP14 during BIP, FE-model (— —) vs RLD (—)	IX
B.8	F^{norm} in HP18 during BIP, FE-model (— —) vs RLD (—)	IX
B.9	F^{norm} in HP31-32 during BIP, FE-model (— —) vs RLD (—)	X
B.10	F^{norm} in HP33-34 during BIP, FE-model (— —) vs RLD (—)	X
B.11	F^{norm} in HP1 during DOC, FE-model (— —) vs RLD (—)	XII
B.12	F^{norm} in HP3 during DOC, FE-model (— —) vs RLD (—)	XII
B.13	F^{norm} in HP4 during DOC, FE-model (— —) vs RLD (—)	XIII
B.14	F^{norm} in HP6 during DOC, FE-model (— —) vs RLD (—)	XIII
B.15	F^{norm} in HP7 during DOC, FE-model (— —) vs RLD (—)	XIV
B.16	F^{norm} in HP12 during DOC, FE-model (— —) vs RLD (—)	XIV
B.17	F^{norm} in HP14 during DOC, FE-model (— —) vs RLD (—)	XV
B.18	F^{norm} in HP18 during DOC, FE-model (— —) vs RLD (—)	XV
B.19	F^{norm} in HP31-32 during DOC, FE-model (— —) vs RLD (—)	XVI
B.20	F^{norm} in HP33-34 during DOC, FE-model (— —) vs RLD (—)	XVI
B.21	F^{norm} in HP1 during SAC, FE-model (— —) vs RLD (—)	XVIII
B.22	F^{norm} in HP3 during SAC, FE-model (— —) vs RLD (—)	XVIII
B.23	F^{norm} in HP4 during SAC, FE-model (— —) vs RLD (—)	XIX
B.24	F^{norm} in HP6 during SAC, FE-model (— —) vs RLD (—)	XIX
B.25	F^{norm} in HP7 during SAC, FE-model (— —) vs RLD (—)	XX

B.26	F^{norm} in HP12 during SAC, FE-model (— —) vs RLD (—)	XX
B.27	F^{norm} in HP14 during SAC, FE-model (— —) vs RLD (—)	XXI
B.28	F^{norm} in HP18 during SAC, FE-model (— —) vs RLD (—)	XXI
B.29	F^{norm} in HP31-32 during SAC, FE-model (— —) vs RLD (—)	XXII
B.30	F^{norm} in HP33-34 during SAC, FE-model (— —) vs RLD (—)	XXII
C.1	Sensitivity analysis of bushing stiffness in HP3 and HP4 showing RMS ^{Event} vs bushing stiffness for all events		XXIII
C.2	Sensitivity analysis of bushing stiffness in HP31-32 and HP33-34 show- ing RMS ^{Event} vs bushing stiffness for all events		XXIV
D.1	Topology of the optimized components for case 1 with only BIP		XXV
D.2	Topology of the optimized components for case 1 with only DOC		XXV
D.3	Topology of the optimized components for case 1 with only SAC		XXVI
D.4	Topology of the optimized LCA with $M \leq [0.6 - 0.9]\bar{M}^{\text{Ref}}$		XXVI
D.5	Topology of the optimized UCA with $M \leq [0.6 - 0.9]\bar{M}^{\text{Ref}}$		XXVI
D.6	Topology of the optimized Toelink with $M \leq [0.6 - 0.9]\bar{M}^{\text{Ref}}$		XXVI
E.1	Proposed workflow		XXVII

List of Tables

3.1	Configuration of TO of case 1	25
3.2	Configuration of TO of case 2	26
4.1	RMS ^{norm} for all force signals during the BIP event, with subtraction of drawing state loads	28
4.2	RMS ^{norm} for all force signals during the DOC event, with subtraction of drawing state loads	29
4.3	RMS ^{norm} for all force signals during the SAC event, with subtraction of drawing state loads	29
4.4	Summary of the system response with respect to bushing stiffness	32
4.5	Results from optimization case 1 with all load cases, BIP, DOC and SAC	39
4.6	Results from optimization case 2, $M \leq \bar{M}^{\text{Ref}}$	41
4.7	Results from optimization case 2, with $M \leq [0.5 - 0.9]\bar{M}^{\text{Ref}}$	42
B.1	RMS ^{norm} for all force signals during the BIP event, with subtraction of drawing state loads	V
B.2	Comparison of mean RMS ^{norm} during BIP	V
B.3	RMS ^{norm} for all force signals during the DOC event, with subtraction of drawing state loads	XI
B.4	Comparison of mean RMS ^{norm} during DOC	XI
B.5	RMS ^{norm} for all force signals during the SAC event, with subtraction of drawing state loads	XVII
B.6	Comparison of mean RMS ^{norm} during SAC	XVII

1

Introduction

This is the report for a master's thesis project on structural optimization of mechanical systems, at Volvo Cars. This chapter defines and motivates the study. It also covers the main ideas behind the project.

1.1 Background

The shift towards electric propulsion of automotive vehicles brings higher demand for lightweight structures since the high prices of battery capacity put further need on energy efficiency. Lightweighting is one among several ways, e.g. reduce drivetrain losses, aerodynamic drag and rolling resistance, to improve energy efficiency and it can bring significant cost advantages in terms of price per range [1–4].

Product development using structural optimization tools plays an essential role in the process of decreasing weight while maintaining mechanical performance. Lightweighting often involves substitution towards high-strength, lightweight materials [4], but it can also refer to optimization of material distribution, i.e. Topology Optimization (TO), a method that finds its true potential in context with additive manufacturing due to high level of design freedom [5–7]. However, TO can also be beneficial in context with other manufacturing techniques such as casting [6]. Previous thesis projects at Volvo Cars have emphasized TO in context of casted components (see [8, 9]) and it is widely used today.

Computer Aided Engineering (CAE) is a key component during the product development process and there is a demand for improved structural optimization methods. Looking at wheel suspension system design, Finite Element (FE) based optimization techniques (e.g. TO) are often used to refine the geometry relatively late in the development process. It is applied to single components with predetermined boundary conditions such as joint loads and joint positions, i.e. constraints that narrows the solution space. In fact, an optimization is generally performed in subject to some constraints and the end result will never be better than what is allowed by those constraints. Hence, it is relevant to explore methods for structural optimization in context with early phase system design.

The main idea for this project is to broaden the solution space by introducing FE-based optimization earlier in the concept phase and by adopting a perspective on system level rather than on component level. The sooner these techniques can be applied, the less parameters (e.g. joint positions) have to be considered as fixed during optimization.

In Figure 1.1 a scheme is proposed on how to combine TO with an outer loop of parametrization, which may become a powerful tool for targeting structural performance during concept generation. The proposed scheme updates the input parameters in the outer loop according to a predefined Design Of Experiments (DOE), which is a systematic method to determine the relations between input and output variables. The topology optimization result is then saved for each set of parameter values and can be studied as a function of the parameters, used as input for conceptual decisions. This method can be applied to mechanical systems in general, but the main focus of this project is to provide a prestudy for application within chassis.

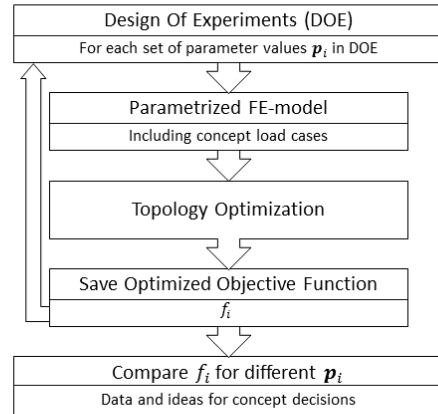


Figure 1.1: Proposed scheme

Two main loops can be identified within the durability and vehicle dynamics parts of the product development process. A simplified overview of the current workflow is presented in Figure 1.2. Today, TO is merely used during the component phase but the idea is to provide a tool that can introduce TO earlier on, i.e. during the system phase. Hence, with the proposed methodology, it may be possible to target system weight at an earlier stage, i.e. when hardpoint positions (joint positions) are not considered as fixed. The hardpoint positions can then be used as input parameters in the outer loop in Figure 1.1.

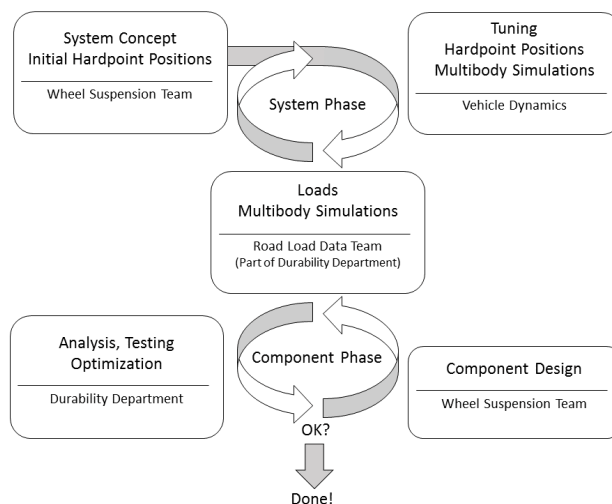


Figure 1.2: Current workflow

1.1.1 Earlier studies

There are plenty of studies on TO of multibody systems (e.g. [10–13]) and a previous thesis work covered parametrization of design volumes with components that competes for packaging volume [14]. However, non of these involves parametrization of joint positions. One of the most relevant studies found involves TO of a ski binding with parametrization of bolt hole positions [15], but application was limited to a one-component TO.

Only a few papers have been found that cover TO of multiple components combined with parametrization of joint positions (see e.g. [16–20]). In 1997, Chickermane and Gea [16] proposed a method to address the issue of multicomponent topology optimization in context with layout of joint positions. However, the proposed method involved overlapping design domains that defines admissible joint positions as well as applications to very simple structures. Similar approaches have been adopted by Qing and Steven [19] in 2001 and by Qian and Ananthasuresh [18] in 2004, but applications were still limited to rather simple and overlapping structures. Later attempts have been made by Yildiz and Saitou [20] in 2011 and Liu [17] in 2016, but applications were still merely academic, involving very simple FE-models for both structures and joints.

Other papers cover optimal layout of support structures with constraints on joint loads [21, 22]. Qian and Ananthasuresh [18] covered optimal embedding of components where they adopted a similar approach as for the embedded joints. This was later developed by Gao et. al [23] in 2015, with applications to more advanced FE-models. However, the TO was limited to the supporting structure, i.e. a one-component TO. Thus, there are seemingly not many publications covering a suitable methodology for this project.

Earlier studies have either been limited to a one-component TO or with applications that are merely academic, i.e. only covering very simple structures. Hence, methods from earlier studies may be hard to extend into industrial level applications for chassis components, i.e. 3D-structures where potential intersections between components have to be avoided. The proposed scheme in Figure 1.1 may be computationally demanding, but it fits existing commercial softwares, i.e. a combination between tools for parametrization [24–26] and tools for TO [27–29]. Therefore this project is not only right in time by considering lightweighting within the automotive industry. It is also highly relevant with respect to the rapid development within generative design (see e.g. [30–32]).

1.2 Aim

The purpose is to study structural optimization of multibody mechanical systems, especially an automotive wheel suspension system. The main goal is to provide a basis for concept generation of multibody systems using FE-based structural optimization. In particular, this work aims to:

- Establish a simplified system model of an automotive wheel suspension system in *Abaqus* [33] and link it to the optimization tools in *Tosca* [28].
- Verify the simplified system model against load data from an existing, dynamic, complete vehicle model in *Adams Car* [34].
- Perform sensitivity analysis with respect to system characteristics such as stiffnesses of components and bushings.
- Propose concept load cases for the wheel suspension system and optimize the material distribution for linkages with respect to weight and stiffness.
- Implement structural optimization for a simple two-body system and propose methods for TO with parametrization of hardpoint positions.

1.3 Limitations

The project is limited to involve:

- TO with simplified FE-modeling and linear assumptions.
- Verification with respect to force signals, i.e. not with respect to other quantities such as moments, displacements, stresses or strains.
- External loads that are assumed to be constant during optimization, i.e. not updated with respect to hardpoint positions or system weight.

Hardpoint positions and system weight may affect external loads, but with consideration to computational effort this iteration in *Adams Car* is left outside the scope of this study. Also note that non-linearities, i.e. geometrical non-linearities and non-linear material models, are left out since it is generally recommended to start with linear FE-models for new TO-problems. However, these limitations may put a need for further development and follow-up projects in the future.

1.4 Specification of issue under investigation

The following questions are addressed in this work:

- What characteristics of components and joints needs to be included in the system FE-model and what can either be simplified or left out in order to benefit the phase of concept generation?
- What load cases are essential in order to capture key characteristics of the rear wheel suspension system during the concept phase?
- How sensitive is the load response of the FE-model with respect to modeled characteristics of bushings?

- How does component stiffness affect internal loads in the system FE-model?
- What measures and requirements are essential for the wheel suspension system at an early stage of development?
- What optimization setup, e.g. objective function and constraints, are suitable for the proposed methodology in Figure 1.1?
- What magnitude of hardpoint repositioning is relevant to study with respect to requirements from other disciplines?
- What is the future potential for topology optimization applied on system level?

By addressing these questions the aim is to provide a good foundation for future use and development of structural optimization on mechanical systems.

2

Theory

This chapter presents the theoretical framework for this project, starting with car chassis and a brief description of the studied rear wheel suspension system. Thereafter some fundamental frameworks within Finite Element Method (FEM) and Topology Optimization (TO) are presented. Later parts involve some specifics about TO in *Tosca* and FE-modeling in *Abaqus* .

2.1 Technological platforms

Traditionally car chassis consisted of a horizontal ladder framework on which other chassis components were mounted, such as suspensions, wheels, steering system, brake systems and transmission. Hence, a *body on frame* structure was used, similar to the configuration for most trucks [35]. Today most cars use a *unibody* structure where part of the chassis structure cannot be distinguished from the body floor. This allows for a stiffer and lighter design, but at the expense of some modularity. In order to keep up product diversification at reasonable costs, car manufacturers standardize through *technological platforms* which include parts of the body as well as the remaining chassis components [35].

The suspension system links the wheels to the body and its main task is to enhance ground contact as well as ride comfort while distributing loads [35]. The kinematics of a functional wheel suspension system should constrain five (out of six) Degree of Freedom (DoF) of each hub. Hence, only allowing for vertical travel. From a rigid body dynamics perspective, this can be achieved through linkages, e.g. five bars with spherical hinges (see Figure 2.1) that constrains one DoF each. Some of the bars are often combined to more advanced links that constrains more than one DoF. See for example the concepts of *McPherson* or *Short Long Arm (SLA)*/ *Double wishbone* suspension systems [35].

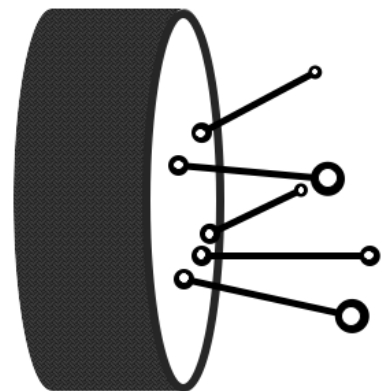


Figure 2.1: Five links constraining one DoF each

The studied system is called an *integral link axle* [36] (see Figure 2.2). This configuration of a rear wheel suspension system is beneficial in terms of packaging volume which is good for boot space. However, the system is rather difficult to understand and thereby tricky to tune and develop.

Each side of the system includes two simple links (upper control arm and toe link) and one H-arm (lower control arm). An H-arm with both outer joints directly connected to the knuckle, i.e the part that connects the links to the wheel, would constrain four dofs on its own. To allow for one more dof, these type of suspension systems are often equipped with an integral link between the knuckle and the outer front hinge of the H-arm. However, for the studied system, that relative movement is instead permitted by one of the bushings.



Figure 2.2: The studied rear wheel suspension system; an integral link rear axle, viewed from behind

It should be noted that, in addition to the integral link, some other differences may be encountered between different concepts within this category of suspension systems; e.g. some have coil springs and two upper control arms on each side. However, the studied system consists of the following components:

1. Two (one for each side) *knuckles* containing the hubs and attachments to the suspension links.
2. Two (one for each side) *upper control arms* that acts as two point (upper) links between the subframe and the corresponding knuckle.
3. Two (one for each side) *lower control arms* that acts as an H-arm between the subframe and the corresponding knuckle. Recall the bushing that acts as an intermediate integral link between the lower control arm and the knuckle.
4. Two (one for each side) *toelinks* that acts as two point links (at the lower front) between the subframe and the corresponding knuckle.
5. A *subframe* that attaches the inner side of the links (opposite from the knuckles) to the body structure.
6. A *leaf spring* that acts as a beam between the lower control arms and the subframe. It mainly stiffens the system with respect to relative vertical motion between the knuckles and the subframe.

7. Two (one for each side) *dampers* that acts between the car body and and the lower control arms to decelerates the wheels during vertical shocks.
8. An *anti-rollbar* that acts as a torsion bar and mainly stiffens the system with respect to rolling motion.

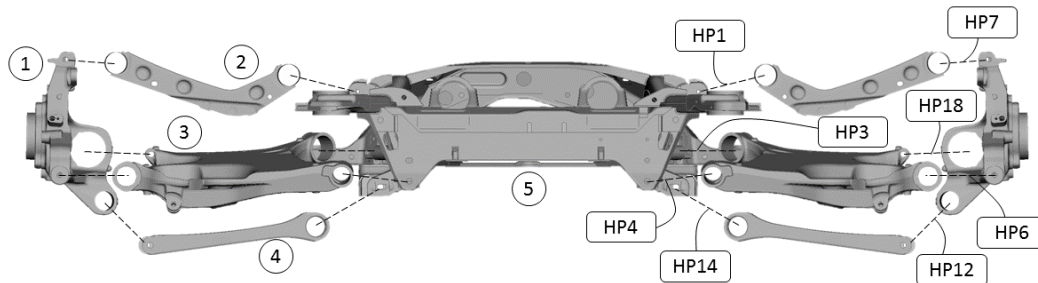


Figure 2.3: System components and hardpoints for linkages

Components 1-5 are marked with circles on the left hand side of Figure 2.3. The main joints between the components consists of ball joints and elastic bushings. The theoretical centers of these joints, i.e. the pivot points between the moving parts, are often called hardpoints (see the right hand side of Figure 2.3) and their relative positions determines much of the suspension system's kinematic properties. It should be noted that the figure only shows hardpoints for the linkages and that each of these hardpoints has a counterpart on the left hand side with the same hardpoint number. Section 3.2.1 shows all hardpoints that are essential for this project.

A ball joint is simply a spherical joint that permits free rotations while preventing translations and these are used in HP6, i.e. the rear joint between the lower control arm and the knuckle.

The rest of the joints involve bushings. These consists of an inner body that connects to one component and an outer body that is fixed to the other. In-between the fixed bodies is a layer of vulcanized rubber that determines the stiffness characteristics of the bushing.

Bushings were initially introduced to avoid lubrication of the joints and the elastic characteristics was mainly seen as a drawback. Today they are used to enhance the elasto-kinematic behavior of the system and to mitigate noise in the coupe [35]. Figure 2.4 shows a principle sketch of a typical bushing. The rotational stiffnesses are usually relatively small in order to allow sufficient link motion. For this example, the translational stiffness in the x -direction is governed by compression of the rubber beam whilst the other directions are governed by its bending characteristics. Moreover, the bending motion in the y -direction is limited; contact between the inner and outer rubber acts as a spring and increases the stiffness [35].

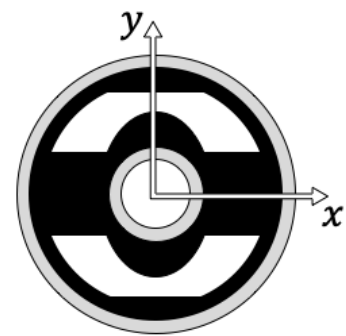


Figure 2.4: Bushing

2.2 Finite Element Method

Finite Element Method (FEM) is a method for solving differential equations numerically with a discretized approximation and is often used to analyze complex mechanical problems. The domain is subdivided into elements defined by a mesh while the field of interest (e.g. displacement) is approximated by piece-wise polynomials that make up a continuous function over the (discretized) domain [37, 38].

2.2.1 Strong format

Consider the body in Figure 2.5 with domain Ω , boundary $\Gamma = \Gamma_D \cup \Gamma_N$ and outwards pointing normal vector \mathbf{n} . It is loaded with the body force \mathbf{b} and traction \mathbf{t}_p .

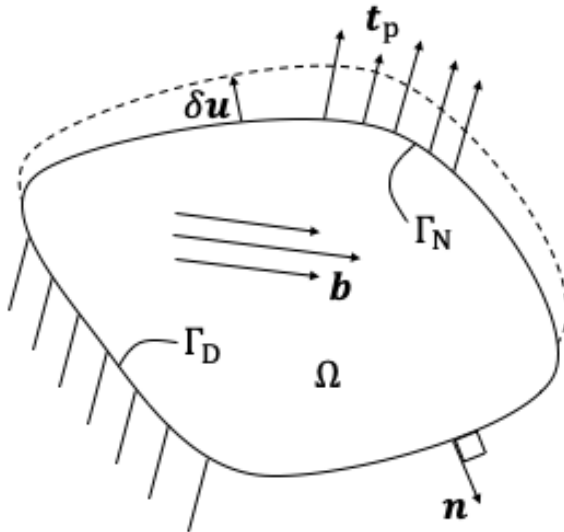


Figure 2.5: Loaded body and kinematically admissible displacements

The strong form for quasi-static linear elasticity reads

$$\begin{cases} -\boldsymbol{\sigma} \cdot \boldsymbol{\nabla} = \mathbf{b} & \text{in } \Omega \\ \mathbf{u} = \mathbf{u}_P & \text{on } \Gamma_D \\ \boldsymbol{\sigma} \cdot \mathbf{n} = \mathbf{t}_P & \text{on } \Gamma_N \end{cases} \quad (2.1)$$

where \mathbf{u} is the displacement vector and $\boldsymbol{\sigma}$ is the second order Cauchy stress tensor [38]. The constitutive relation reads

$$\boldsymbol{\sigma} = \mathbf{E} : \boldsymbol{\epsilon} \quad (2.2)$$

where $\boldsymbol{\epsilon} = \boldsymbol{\epsilon}[\mathbf{u}] = [\mathbf{u} \otimes \boldsymbol{\nabla}]^{\text{sym}}$ is the second order strain tensor and \mathbf{E} is the fourth order stiffness tensor for isotropic linear elasticity [38].

2.2.2 Weak format

Consider an infinitesimal, kinematically admissible, virtual displacement $\delta \mathbf{u}$ (later called test function) of the body in Figure 2.5. The weak format can then be derived from the stationary condition in the principle of minimum total potential energy (see for example [38, 39]) and is stated as; find $\mathbf{u} \in \mathbb{U}$ such that:

$$a(\mathbf{u}, \delta \mathbf{u}) = l(\delta \mathbf{u}) \quad \forall \delta \mathbf{u} \in \mathbb{U}^0 \quad (2.3)$$

with the variational forms

$$\begin{aligned} a(\mathbf{u}, \delta \mathbf{u}) &= \int_{\Omega} \boldsymbol{\epsilon}[\mathbf{u}] : \mathbf{E} : \boldsymbol{\epsilon}[\delta \mathbf{u}] \, d\Omega \\ l(\delta \mathbf{u}) &= \int_{\Omega} \mathbf{b} \cdot \delta \mathbf{u} \, d\Omega + \int_{\Gamma_N} \mathbf{t}_P \cdot \delta \mathbf{u} \, d\Gamma \end{aligned} \quad (2.4)$$

as well as the trial and test spaces

$$\begin{aligned} \mathbb{U} &= \left\{ \mathbf{v} \mid \int_{\Omega} [|\mathbf{v}|^2 + |\mathbf{v} \otimes \nabla|^2] \, d\Omega < \infty, \mathbf{v} = \mathbf{u}_P \text{ on } \Gamma_D \right\} \\ \mathbb{U}^0 &= \left\{ \mathbf{v} \mid \int_{\Omega} [|\mathbf{v}|^2 + |\mathbf{v} \otimes \nabla|^2] \, d\Omega < \infty, \mathbf{v} = \mathbf{0} \text{ on } \Gamma_D \right\} \end{aligned} \quad (2.5)$$

2.2.3 FE-format

Consider the FE-approximation \mathbf{u}_h as

$$\mathbf{u} \approx \mathbf{u}_h = \sum_{k=1}^n \underline{\mathbf{N}}_k(\mathbf{a})_k = \underline{\mathbf{N}} \mathbf{a} \in \mathbb{U}_h \subset \mathbb{U} \quad (2.6)$$

where the shape functions $\underline{\mathbf{N}}$ and the nodal displacements \mathbf{a} reads

$$\begin{aligned} \underline{\mathbf{N}} &= \begin{bmatrix} N_1 & 0 & 0 & N_2 & 0 & 0 & \dots & N_n & 0 & 0 \\ 0 & N_1 & 0 & 0 & N_2 & 0 & \dots & 0 & N_n & 0 \\ 0 & 0 & N_1 & 0 & 0 & N_2 & \dots & 0 & 0 & N_n \end{bmatrix} \\ \mathbf{a} &= [u_{x,1} \quad u_{y,1} \quad u_{z,1} \quad u_{x,2} \quad u_{y,2} \quad u_{z,2} \quad \dots \quad u_{x,n} \quad u_{y,n} \quad u_{z,n}]^T \end{aligned} \quad (2.7)$$

The FE-format is obtained by introducing the approximation in Equation (2.6) into the weak format; Equations (2.3)-(2.4). On abstract form it reads

$$a(\mathbf{u}_h, \delta \mathbf{u}_h) = l(\delta \mathbf{u}_h) \quad \forall \delta \mathbf{u}_h \in \mathbb{U}_h^0 \subset \mathbb{U}^0 \quad (2.8)$$

which is equivalent to the well known matrix equation

$$\underline{\mathbf{K}} \mathbf{a} = \underline{\mathbf{f}} \quad (2.9)$$

where $\underline{\mathbf{K}}$ is the global stiffness matrix and $\underline{\mathbf{f}}$ is the global (external) force vector [37, 38].

2.3 Topology Optimization

As described in [40], the general structural optimization problem takes the form

$$\begin{cases} \text{minimize } f(\boldsymbol{\xi}, \boldsymbol{\eta}) \text{ with respect to } \boldsymbol{\xi} \text{ and } \boldsymbol{\eta} \\ \text{subject to } \begin{cases} \text{design constraints on } \boldsymbol{\xi} \\ \text{state constraints on } \boldsymbol{\eta} \\ \text{equilibrium constraint} \end{cases} \end{cases} \quad (2.10)$$

where f is the objective function, $\boldsymbol{\xi}$ are design variables and $\boldsymbol{\eta}$ are state variables (both vectors in a general case). Structural Optimization is a wide term including, Size, Shape and Topology Optimization. Here the focus is on the latter, which is a tool that finds the optimal material distribution in a design space, given an optimization goal and a set of constraints, e.g. minimizing weight whilst maintaining stiffness requirements. TO can either be gradient-based (i.e. optimization with gradient techniques), or non gradient-based. The former is widely used and is arguably more efficient when it comes to solving fine-resolution problems, although one disadvantage is that the result may be a local extrema rather than the global optimum [41]. Non-gradient based methods uses global search and refers to heuristic algorithms, e.g. *evolutionary algorithms* such as the genetic algorithm [42] and *swarm intelligence* such as ant colony [43] or particle swarm [44].

Two common algorithms for gradient-based TO are the Method of Moving Asymptotes (MMA) and the Optimality Criteria (OC). MMA was originally introduced by Krister Svanberg in 1987 [45] and has since then been developed further. The method is iterative and in each step a strictly convex approximating subproblem is generated (with respect to the so called 'moving asymptotes') and solved using a gradient method. The OC method uses Lagrange multipliers to define the topology optimization where compliance is minimized under a volume constraint. In order to handle inequality constraints Lagrange multipliers method is supplemented with Karush- Kuhn-Tucker conditions [46].

2.3.1 TO example: Minimum compliance using SIMP

Minimum compliance (i.e. maximum global stiffness) is one of the simplest types of design problem formulations within TO, where the squared energy norm $\|\mathbf{u}\|_a^2 = a(\mathbf{u}, \mathbf{u})$ is to be minimized [46]. Together with Equation (2.3), the minimum compliance problem then takes the form

$$\begin{aligned} \min_{\mathbf{u} \in \mathbb{U}, \mathbf{E}} \quad & l(\mathbf{u}) \\ \text{s.t.} \quad & a(\mathbf{u}, \delta \mathbf{u}) = l(\delta \mathbf{u}), \quad \forall \delta \mathbf{u} \in \mathbb{U}^0, \mathbf{E} \in \mathbf{E}_{\text{ad}} \end{aligned} \quad (2.11)$$

where \mathbf{E}_{ad} denotes the set of admissible stiffness tensors. The discrete form reads

$$\begin{aligned} \min_{\mathbf{u}, \mathbf{E}} \quad & \mathbf{f}^\top \mathbf{u} \\ \text{s.t.} \quad & \mathbf{K}(\mathbf{E}_e) \mathbf{u} = \mathbf{f}, \quad \mathbf{E}_e \in \mathbf{E}_{\text{ad}} \end{aligned} \quad (2.12)$$

where the stiffness matrix \mathbf{K} depends on the element stiffness \mathbf{E}_e and is written as

$$\mathbf{K} = \sum_{e=1}^N \mathbf{K}_e(\mathbf{E}_e) \quad (2.13)$$

There are various possible definitions of \mathbf{E}_{ad} . One possible definition is to formulate a distributed, discrete valued, design problem as follows

$$\mathbf{E} = 1_{\Omega^{\text{opt}}} \mathbf{E}^0, \quad 1_{\Omega^{\text{opt}}} = \begin{cases} 1 & \text{if } \mathbf{x} \in \Omega^{\text{opt}} \\ 0 & \text{if } \mathbf{x} \in \Omega \setminus \Omega^{\text{opt}} \end{cases} \quad (2.14)$$

$$\int_{\Omega} 1_{\Omega^{\text{opt}}} d\Omega = \text{Vol}(\Omega^{\text{opt}}) \leq V.$$

where \mathbf{x} is the coordinate vector that corresponds to the chosen reference frame and \mathbf{E}^0 is the stiffness tensor for the given isotropic material. Furthermore, Ω is the predefined design space and Ω^{opt} is the sought optimal subset of Ω . The last inequality expresses the limit on the amount of material that is at disposal, where V is the upper limit for the volume.

One way to solve the discrete valued design problem in Equation (2.14) is to replace the integer values with continuous variables and then introduce a penalty parameter that steers the solution into discrete 0/1 values. The most common method is the Solid Isotropic Material with Penalization (SIMP) method [46], which reformulates Equation (2.14) as follows

$$\mathbf{E}(\mathbf{x}) = \rho(\mathbf{x})^p \mathbf{E}^0, \quad p > 1, \quad (2.15)$$

$$\int_{\Omega} \rho(\mathbf{x}) d\Omega \leq V; \quad \rho_{\min} \leq \rho(\mathbf{x}) \leq 1, \quad \mathbf{x} \in \Omega$$

where the design variable $\rho(\mathbf{x})$ can be interpreted as a material density fraction and p is the penalization factor that steers the intermediate densities towards 0 or 1. In order to get true '0/1' design, $p \geq 3$ is usually sufficient for materials with Poisson's ratio $\nu = 0.33$ [47]. Furthermore, in order to prevent any possible singularity of the equilibrium problem a lower bound ρ_{\min} is introduced, typically set to $\rho_{\min} = 10^{-3}$.

2.3.2 TO in Tosca

Tosca Structure uses two different principle approaches for solving topology optimization problems; the controller-based approach and the general sensitivity-based approach. The former is based on the OC method and is restricted to minimum compliance optimizations with a volume equality constraint. The sensitivity-based approach uses MMA and enables other objective functions as well as constraints (e.g. displacement, stress, and eigenfrequencies). Both approaches use SIMP as the interpolation method with $p = 3$ as default for static load cases [48].

Tosca structure also allows for other types of manufacturing constraints such as demold directions, symmetry constraints and member size constraints.

2.4 FE-modeling in Abaqus

This section is intended to give a brief overview of software specific terminology and modeling in *Abaqus*, involving *connector elements* and *coupling constraints*.

2.4.1 Connector elements

Connector elements are used to model connections; e.g. rigid connections, ball joints or bushings between different parts. Kinematic constraints are enforced with Lagrange multiplier method. Hence, the system of equations grows in size for each imposed kinematic constraint. A connector element is defined between two nodes and governed by the defined connector type together with a corresponding connector behavior, e.g. allowed degrees of freedom and what element stiffness those relative motions are associated with [48]. Below is a description of connector types used:

- **BEAM** imposes kinematic constraints such that no components of relative motions (translations as well as rotations) are allowed [48].
- **JOIN** imposes kinematic constraints such that no components of relative translations are allowed [48]. Hence, it describes a typical frictionless ball joint.
- **CARTESIAN** does not impose any kinematic constraint, but allows translational components of relative motion to be associated with a connector behavior, e.g. stiffness components. [48].
- **ROTATION** does not impose any kinematic constraint, but allows rotational components of relative motion to be associated with a connector behavior, e.g. stiffness components. [48].

2.4.2 Coupling constraints

Coupling constraints defines coupling conditions between a *reference node* and a group of *coupling nodes* with respect to selected degrees of freedom [48]. Below is a description of the two available types of coupling constraints:

- **KINEMATIC** constrains the motion of the coupling nodes to the rigid body motions of the reference node. This is imposed by eliminating degrees of freedoms at the coupling nodes [48]. Hence, if all six degrees of freedoms are selected, the nodes will be rigidly connected.
- **DISTRIBUTING** constrains the motion of the coupling nodes by distributing loads, acting on the reference node, to the coupling nodes. (For an arbitrary number of coupling nodes the equation system is underdetermined and there is no unique solution for equilibrium. Weight factors in combination with node positions are then used to determine the load distribution [48].)

3

Methodology

This chapter describes the methodology for the project. The work consists of three main parts; *Project Prestudy*, *Finite Element Analysis (FEA)* and *Structural Optimization*. Figure 3.1 shows an overview of the workflow.

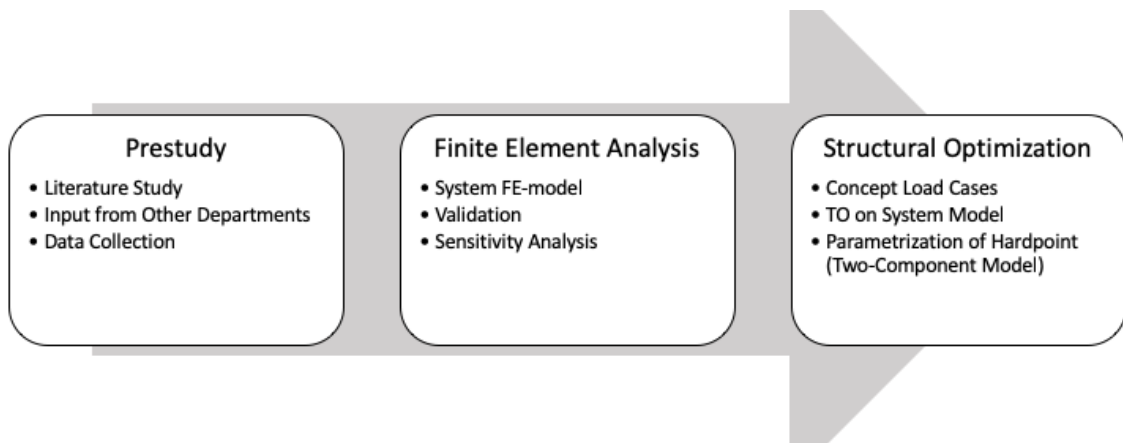


Figure 3.1: Overview of project and methodology

The prestudy includes literature study, data collection and gathering of input from pertinent departments. This is in order to establish sufficient knowledge within TO, vehicle dynamics and FE-modeling. Data collection is mainly about load data from previous simulations of the dynamic, full vehicle, model in *Adams Car*.

The second part involves development of an FE-model of the wheel suspension system, including identification of characteristics of components, joints and boundary conditions. It also involves verification with respect to force signals as well as sensitivity analysis with respect to stiffness of components and bushings.

The structural optimization part covers concept load cases as well as optimization strategies. TO is performed on the FE-model of the wheel suspension system, with the linkages as design volumes. Since previous studies within TO combined with parametrization of joint positions are limited, it is suitable to first learn from a simple problem. Therefore this study is limited to provide a prestudy for future development and the parametrization study is only performed on a simpler two-component model.

3.1 Prestudy

Except for planning, literature study and input from other disciplines the prestudy mainly involves data collection of load signals.

3.1.1 Strength events

During the complete vehicle simulations in *Adams Car*, load signals are recorded for each hardpoint and saved as Road Load Data (RLD). Three strength events are chosen in consultation with employees at Volvo Cars, i.e. Brake In Pothole (BIP), Drive Over Curb (DOC) and Skid Against Curb (SAC). Figure 3.2 shows snapshots from the selected events.

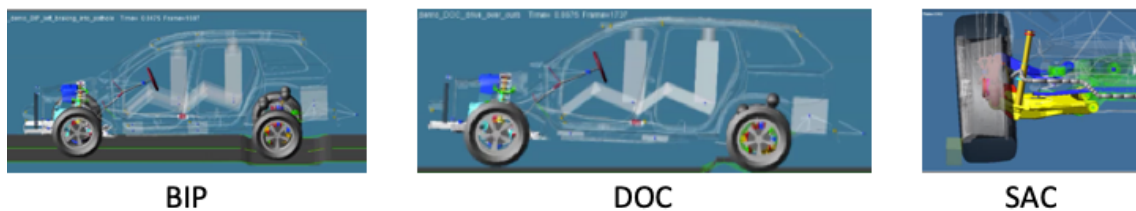


Figure 3.2: Snapshots from studied strength events

BIP captures longitudinal loading while DOC involves vertical loading and SAC covers lateral loading. Events governed by rolling loads are avoided in order to enable the simplification of excluding the anti-rollbar within the FE-model.

3.2 Finite Element Analysis

There exists a wide range of commercial softwares for FEA and in this project *Ansa* is used as a pre-processor, *Abaqus* as a solver and *Meta* as a post-processor. The simplified FE-model is validated with respect to force signals corresponding to RLD of the complete vehicle model. Outer load signals from the RLD are applied to the system FE-model and force signals in wheel suspension joints are then compared with the corresponding signals from the RLD.

3.2.1 FE-model

The development process is initiated by modeling of the individual components which are then assembled into a system model. Modeling and parallelly validating is an iterative process but this section is mainly intended to describe the final model.

3.2.1.1 Bushing attachments and material models for components

All components are modeled with isotropic linear elastic materials, except for the glass fiber leaf spring, which is modeled with an orthotropic linear elastic material model. **KINEMATIC** constraints are used to model rigid behavior between the theoretical centers of the bushing's outer bodies and the corresponding interfaces on the components (see for example HP14 in Figure 3.3). Similarly, connector **BEAM** is used to model rigid inner bushing bodies (see for example HP12 in Figure 3.3). Attachments for ball joints are modeled in the same manner (see HP6 in Figures 3.7 and 3.6).

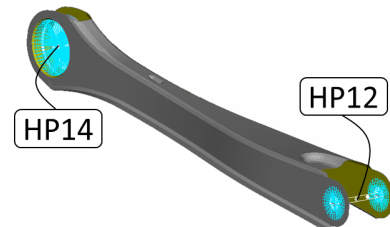


Figure 3.3: Toelink

3.2.1.2 Steel sheet components

The Upper Control Arm (UCA) and the Toelink (see Figures 3.3 and 3.4) consist of steel sheets with thicknesses in the range of 2.0-2.8 mm. The components are modeled with 3 mm mixed three node triangular (S3R in **Abaqus**) and four node quadrilateral (S4 in **Abaqus**) shell elements. Furthermore, the UCA contains multiple seam and spot welds which are rigidly modeled, i.e. with connector **BEAM** and **KINEMATIC** coupling respectively.

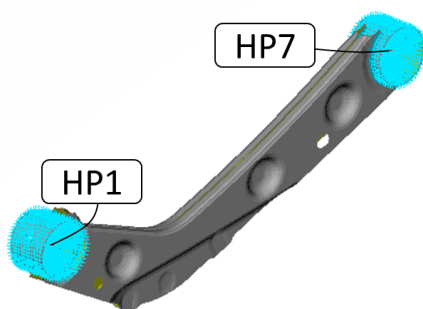


Figure 3.4: UCA

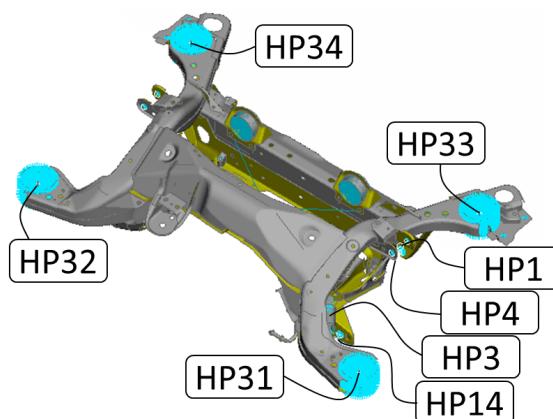


Figure 3.5: Subframe

The subframe (see Figure 3.5) is mainly made out of steel sheets with thicknesses in the range of 1.8-4.0 mm and is modelled with a similar methodology, but where the element size is within the range of 3-5 mm.

3.2.1.3 Aluminum cast components

The Lower Control Arm (LCA) as well as the main body of the knuckle consists of cast aluminum. The components (see Figures 3.6 and 3.7) are modeled with 3 mm four node tetrahedral (C3D4 in Abaqus) solid elements. The LCA's interface with the damper (see HP56 in Figure 3.6) is modeled with connector BEAM and the connection with the leaf spring (see HP68 in Figure 3.6) is modeled with a DISTRIBUTING coupling constraint, such that the load is distributed over a surface, corresponding to a type of bushing.

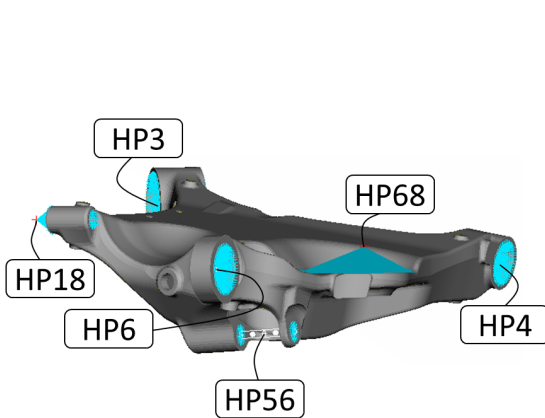


Figure 3.6: LCA

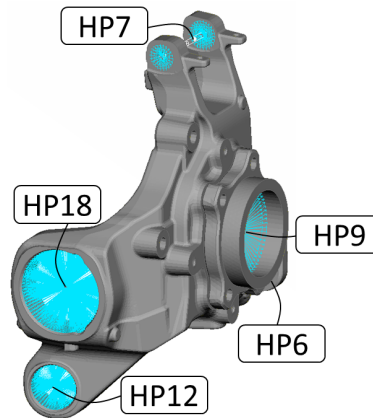


Figure 3.7: Knuckle

3.2.1.4 Boundary conditions

On a vehicle, the subframe is attached to the car body through bushings in HP31-34 (see Figure 3.5). However, in a chassis rig test the car body bushings are attached to a steel fixture (in general stiffer than the body). In this system FE-model the car body/fixture is assumed to be rigid. Inner bushing bodies are fixed through a KINEMATIC coupling with a fixed reference node, while the subframe is connected to the outer bushing bodies. Hence, relative movement between the subframe and the fixture depends on bushing stiffness. A simple illustration of the boundary conditions are shown in Figure 3.8 where the spring elements (representing the bushing's stiffnesses) are fixed in one end and attached to the outer bushing body in the other.

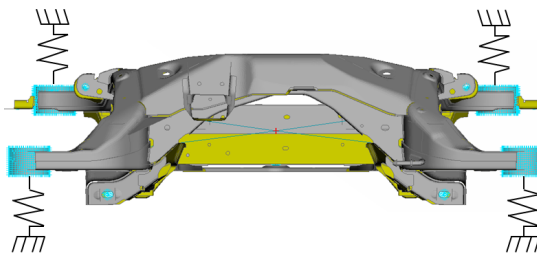


Figure 3.8: Boundary conditions similar to a chassis rig test fixture

3.2.1.5 Assembly

Figure 3.9 shows the assembled model together with the global reference frame for the car. The components are attached to each other through connector elements, one in each hardpoint. Each connector element acts between two coinciding nodes, i.e. between the center nodes of the corresponding *inner* and *outer* bushing bodies.

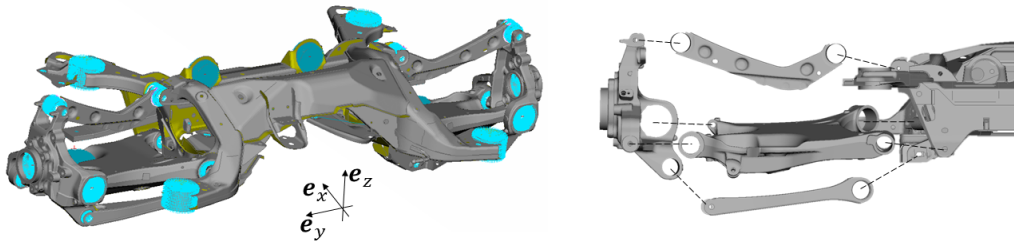


Figure 3.9: Assembly and global reference frame

The connector type `JOIN` is used to model the ball joints (HP6). The rest of the joints consists of bushings which are modelled with a combination of the two connector types; `CARTESIAN` and `ROTATION`. These are also associated with a corresponding connector behavior that refers to the bushing's stiffness characteristics. Note that `ROTATION` is chosen based on the assumption that rotations can be considered small.

3.2.1.6 Linear elastic bushing characteristics

Non-linear bushing characteristics are linearized, but it is not obvious what stiffness to choose in order to replicate load distributions over several strength events. Translational characteristics are described by uni-axial force-displacement curves and rotational characteristics are described by moment-rotation curves. The linear bushing characteristics are shown in Appendix A where they are presented together with the corresponding non-linear data (all without scales to protect corporate data). Rotational stiffnesses uses the initial stiffnesses around the origin, while the translational stiffnesses are chosen to some value between the lowest and the highest tangent of the corresponding bushing characteristics. The corresponding directions refers to local reference frames for each bushings, i.e. not the global reference system for the car. The values of the translational stiffnesses are essentially chosen by changing the stiffnesses from low to high and then analyzing the response of the system and choosing the value that corresponds well to the RLD.

3.2.1.7 Damper loads

Since there are no velocity during quasi-static analysis, damping characteristics would have no effect. However, the damper behavior needs to be included somehow in order to get reasonable load signals. This is solved by applying external forces

from the dampers, acting on the lower control arms (see Figure 3.10). These forces varies in time in accordance with the RLD.

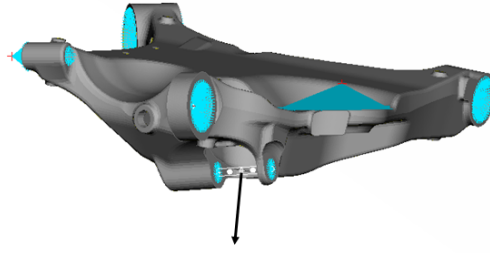


Figure 3.10: Damper force

It should be noted that this method is associated with some drawbacks. Peak loads from the dampers may result in some non-physical deflections of the system during quasi-static analyses. This is because the entire damper force is used to statically deform the system, while in a dynamic case the force mainly acts to decelerate the unsprung mass.

3.2.1.8 Drawing state loads and pretension forces

The FE-model is unloaded in its initial state (the drawing state), at least if pretension forces are not taken into consideration, while in reality (and in the dynamic simulations) it is not. It is essentially loaded by the vehicle weight. This has to be accounted for in order to get comparable load signals between the system FE-model and the RLD. Two methods are used to handle this. The first involves determination of the *drawing state loads*, i.e. the loads that correspond to the vehicle standing on the ground, and then to subtract these from the RLD before comparison. The second method involves pretension forces with vertical force components that act in the leaf spring. These forces have to act as internal forces to the system in the sense that no forces are added to the system as a whole. The pretension forces are shown in Figure 3.11 where the red components, acting on the lower control arms and the subframe, are applied in the model.

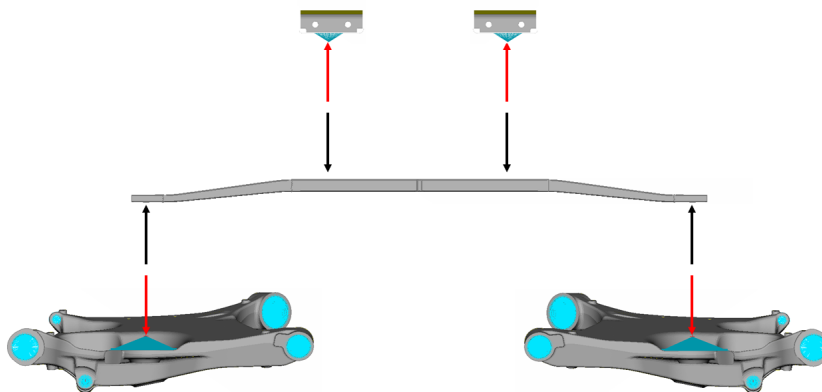


Figure 3.11: Pretension forces from the leaf spring at drawing state

The first method provides slightly better accuracy and involves less uncertainties, why it is used during sensitivity analysis as well as for verification of the FE-model. However, the second provides almost as good accuracy and since no loads are subtracted it is preferable for use during optimizations.

3.2.2 Verification with respect to force signals

The FE-model is verified against the RLD with respect to force-time signals. In order to get a broader view of how well it correlates, the verification is based on time sequences from the strength events rather than just single snapshots in time. For each event, a time interval is chosen such that the peak loads are captured. The corresponding sequence for external loads, i.e. at the knuckles in HP9 and the dampers in HP56, are then applied to the FE-model. Forces in intermediate hardpoints are then validated against the corresponding load signals from the RLD. Quasi-static analyses are used with load signals applied as 100 static load steps. Hence, these are not dynamic analyzes. The force signals, from both the FE-model and the RLD, are normalized according to Equation (3.1) before comparison.

$$F_{ish}^{\text{norm}} = \frac{F_{ish}}{\max_{i,s} (|F_{ish}^{\text{(RLD)}}|)} \quad (3.1)$$

Here h denotes hardpoint number, s denotes side, i.e. left (LH) or right (RH), and i denotes force component in the global coordinate system for the car. The normalization emphasizes that correlation of large magnitude components is more important than correlation of small ones. In order to quantify the deviations, Root Mean Square (RMS) values of the errors are calculated for the normalized force components as

$$\text{RMS}^{\text{norm}}(i, s, h) = \sqrt{\frac{1}{N} \sum_{n=1}^N \left(F_{ishn}^{\text{norm (FE)}} - F_{ishn}^{\text{norm (RLD)}} \right)^2} \quad (3.2)$$

where n denotes the current time step. Hence, together with the normalization in Equation (3.1), RMS^{norm} can be interpreted as the RMS value of the error, normalized by the largest RLD-force component in the corresponding hardpoint.

3.2.3 Sensitivity Analysis: Bushing Stiffness

As mentioned previously, it is not obvious what linear characteristics to choose for the bushings. Therefore, a sensitivity analysis of bushing stiffness is performed where the bushing stiffnesses for different hardpoints are varied one at a time, while everything else is held constant. They are varied between the lowest and highest tangent stiffness for the corresponding bushing (see Appendix A).

The sensitivity analysis is evaluated with respect to Root Mean Square (RMS) values of the error, i.e. the difference between the FE-model and the RLD. The RMS values are evaluated in two ways; RMS^{HP} refers to the deviation in each hardpoint number and $\text{RMS}^{\text{Event}}$ to a total deviation for an event, see Equations (3.3) and (3.4).

$$\text{RMS}^{\text{HP}}(h) = \sqrt{\frac{1}{I + S + N} \sum_{i=1}^I \sum_{s=1}^S \sum_{n=1}^N \left(F_{ishn}^{(\text{FE})} - F_{ishn}^{(\text{RLD})} \right)^2} \quad (3.3)$$

$$\text{RMS}^{\text{Event}} = \sqrt{\frac{1}{H + I + S + N} \sum_{h=1}^H \sum_{i=1}^I \sum_{s=1}^S \sum_{n=1}^N \left(F_{ishn}^{(\text{FE})} - F_{ishn}^{(\text{RLD})} \right)^2} \quad (3.4)$$

Here h , i , s and n are defined in accordance with Subsection 3.2.2. The sensitivity analysis of bushing stiffness aims to capture how sensitive it is to make an ansatz about these values at an early stage, i.e. before the bushing characteristics are determined, but also to measure the sensitivity of the results from the verification.

3.2.4 Sensitivity Analysis: Component Stiffness

In addition to bushing stiffness, a similar study is performed with respect to component stiffness, where Young's modulus for the linkages are varied. The aim is to study how sensitive the load distribution is with respect to component stiffness. Therefore, this analysis focuses on changes in peak forces rather than RMS values and serves as a prestudy for the optimization part, where component stiffness depends on the topology.

3.3 Structural Optimization

There exists a wide range of commercial software for TO and in this project *Tosca GUI* is used as a preprocessor, *Tosca Structure* as an optimizer, *Abaqus* as a FE-solver and *Tosca viewer* as a postprocessor. The parametrization of hardpoint positions are limited to involve a two-component problem.

3.3.1 Two-component problem

As mentioned in Chapter 1, there are seemingly not much literature on how to combine TO with parametrization of joint positions, at least not within industrial applications. Hence, general method development is needed within this area before application to complex models such as the studied wheel suspension system. Therefore a simple, made up, two-component problem is used to investigate different optimization strategies in context with parametrization of hardpoint positions.

The two-component model consists of two links that are connected to each other (see Figure 3.12). It is modeled in accordance with the methodology for the wheel suspension system. There are four hardpoints in total, where two of them are connected to ground through bushings, represented by spring elements in the figure. The components are also connected through a bushing and the upper three-point-link is loaded in the hardpoint to the right.

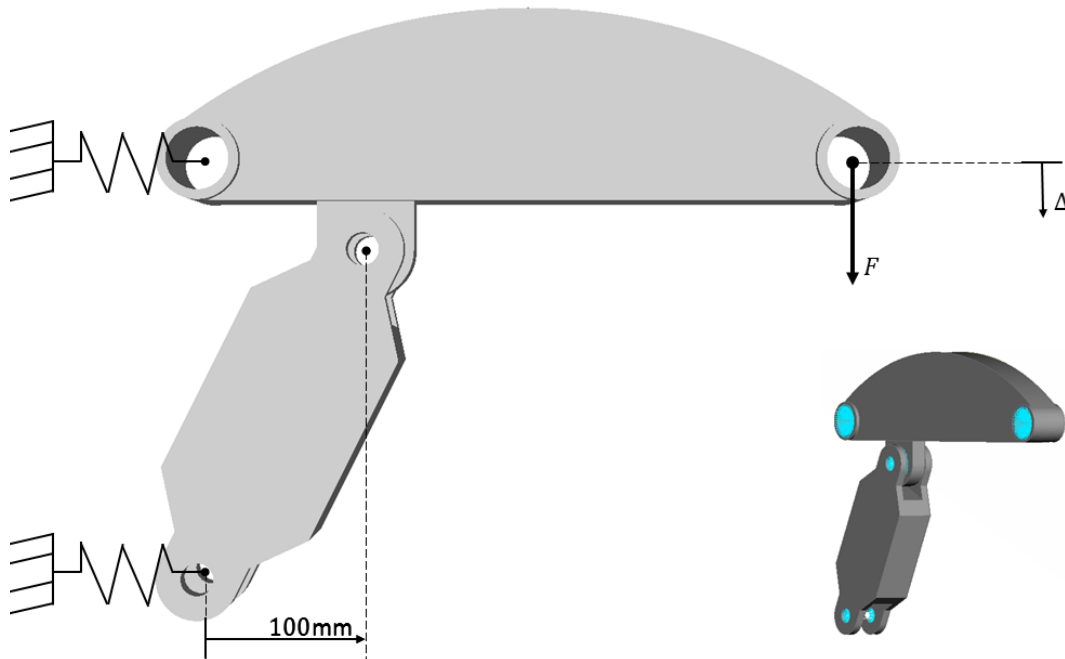


Figure 3.12: Two-component model: Problem definition and Abaqus FE-model

The bushings are either set to be rigid or flexible in order to study how flexible bushings affect optimization. The bushings have rotationally symmetric stiffnesses and the parametrization is with respect to the horizontal position of the common hardpoint between the links. It is varied between 100 mm (as currently seen in Figure 3.12) and 300 mm with a step size of 25 mm. Both components are defined as design volumes (the available design space Ω) but the topology for the zones around the bushings are frozen through design constraints.

The two-component model is used to study different optimization strategies, where the following three are included within this report:

- **Minimize mass**, with constraint on the vertical tip-displacement ($\Delta \leq 1$ mm) for a model with **rigid bushings**.
- **Minimize mass**, with constraint on the vertical tip-displacement ($\Delta \leq 10$ mm) for a model with **flexible bushings**.
- **Minimize strain energy**, with a constraint on system mass of 1.35 kg, for a model with **flexible bushings**.

3.3.2 TO of the wheel suspension system

This section explains the setup for topology optimization of the wheel suspension system, where linkages are optimized with respect to weight and stiffness. The validated FE-model is used as a reference model and provides benchmarks for stiffness requirements and performance measurements.

3.3.2.1 Design volumes of the linkages

Linkages are exchanged for design volumes (see Figure 3.13) that defines the available design space Ω . More detailed views of the design volumes are shown in Figures 3.14-3.16. These uses four node tetrahedral elements with an element size of 6 mm instead of 3 mm. This is simply in order to reduce the number of elements, making the computational effort manageable and should be fine enough to represent stiffness behavior. All design volumes are made of cast aluminium and are modelled in accordance with the methodology described in Section 3.2.1. The zones around coupling constraints and connector elements are frozen through design constraints.

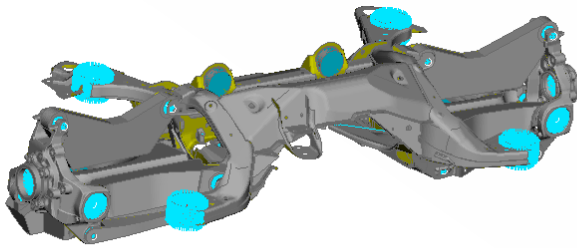


Figure 3.13: Linkages as design volumes

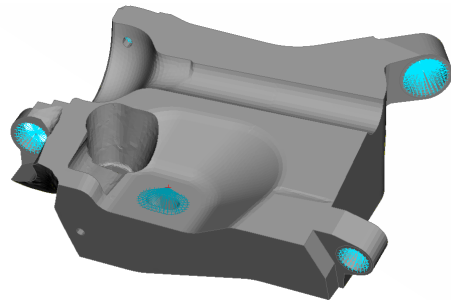


Figure 3.14: LCA design volume

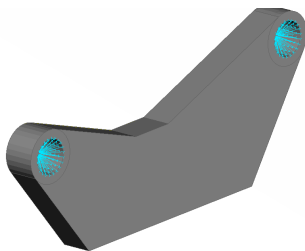


Figure 3.15: UCA design volume

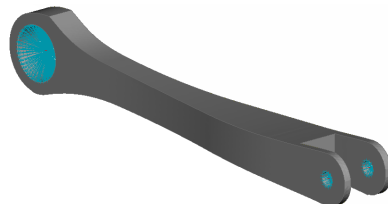


Figure 3.16: Toelink design volume

3.3.2.2 Concept load cases

The concept load cases consists of external loads applied at the knuckles in HP9, damper loads in HP56 and pretension forces in the leaf spring. The pretension forces are based on the car weight that is supported by the rear wheels as follows

$$F_z^{\text{pret}} = PF \cdot RM \quad (3.5)$$

where F_z^{pret} is the magnitude of the applied vertical force components (illustrated in Figure 3.11), RM is the total mass acting on the rear wheels and PF is the Pretension load factor. Note that RM differs slightly between the strength events due to different car loading, but PF should be fixed for a certain car, where $PF = 7.1$ in this case.

External loads at the knuckles in HP9 and at the dampers in HP56 are based on a snapshot in time that corresponds to the governing peak load at the knuckle for each event, i.e. the largest longitudinal force component for BIP, the largest vertical force component for DOC and the largest lateral force component for SAC. Note that the concept load cases involves asymmetry in accordance with the strength events.

3.3.2.3 Topology optimization configuration

Since the load cases are asymmetric a symmetry condition is applied in the xz -plane to ensure geometrical symmetry with respect to the left and right hand side of the car. The optimization strategy is to minimize strain energy subject to a mass constraint. Two main cases are presented, the first without additional constraints and the second with additional constraints on the displacements at the wheel center.

The configuration for the first optimization case is defined in Table 3.1. The objective is to minimize strain energy with a mass constraint, where \bar{M}^{Ref} refers to the weight of the linkages in the reference model. The optimization is first performed with respect to one load case at a time in order to study how different strength events affect the topology. However, the last is with respect to an equally weighted combination of all three load cases in order to gain robustness within the structure.

Table 3.1: Configuration of TO of case 1

Objective function	Constraint	Load case
Minimize strain energy	$M \leq \bar{M}^{\text{Ref}}$	BIP
		DOC
		SAC
		BIP + DOC + SAC

The configuration for the second optimization case is presented in Table 3.2. As for the mass, the allowed displacement is based on the reference model. However, the

displacement constraints can be violated during the optimization and thus need to be checked afterwards. The displacement constraints are such that they constrain the governing displacement direction in the wheel center (HP9) for each event. Thus for BIP, which captures longitudinal loading, the constraint is on the x -component. Similarly the constraint is on the z -component for DOC and on the y -component for SAC. The topology optimization is then iterated with lower and lower mass constraints until the displacement constraints are just fulfilled. However, note that system stiffness as well as the system weight will normally increase during the design realization step. The corresponding optimization setups are presented in Table 3.2.

Table 3.2: Configuration of TO of case 2

Objective function	Constraint	Load case
Minimize strain energy	$M \leq \bar{M}^{\text{Ref}}$ $ u_x^{\text{BIP}} \leq \bar{u}_x^{\text{BIP}} $ $ u_z^{\text{DOC}} \leq \bar{u}_z^{\text{DOC}} $ $ u_y^{\text{SAC}} \leq \bar{u}_y^{\text{SAC}} $	BIP + DOC + SAC
Minimize strain energy	$M \leq 0.9\bar{M}^{\text{Ref}}$ $ u_x^{\text{BIP}} \leq \bar{u}_x^{\text{BIP}} $ $ u_z^{\text{DOC}} \leq \bar{u}_z^{\text{DOC}} $ $ u_y^{\text{SAC}} \leq \bar{u}_y^{\text{SAC}} $	BIP + DOC + SAC
Minimize strain energy	$M \leq 0.8\bar{M}^{\text{Ref}}$ $ u_x^{\text{BIP}} \leq \bar{u}_x^{\text{BIP}} $ $ u_z^{\text{DOC}} \leq \bar{u}_z^{\text{DOC}} $ $ u_y^{\text{SAC}} \leq \bar{u}_y^{\text{SAC}} $	BIP + DOC + SAC
Minimize strain energy	$M \leq 0.7\bar{M}^{\text{Ref}}$ $ u_x^{\text{BIP}} \leq \bar{u}_x^{\text{BIP}} $ $ u_z^{\text{DOC}} \leq \bar{u}_z^{\text{DOC}} $ $ u_y^{\text{SAC}} \leq \bar{u}_y^{\text{SAC}} $	BIP + DOC + SAC
Minimize strain energy	$M \leq 0.6\bar{M}^{\text{Ref}}$ $ u_x^{\text{BIP}} \leq \bar{u}_x^{\text{BIP}} $ $ u_z^{\text{DOC}} \leq \bar{u}_z^{\text{DOC}} $ $ u_y^{\text{SAC}} \leq \bar{u}_y^{\text{SAC}} $	BIP + DOC + SAC
Minimize strain energy	$M \leq 0.5\bar{M}^{\text{Ref}}$ $ u_x^{\text{BIP}} \leq \bar{u}_x^{\text{BIP}} $ $ u_z^{\text{DOC}} \leq \bar{u}_z^{\text{DOC}} $ $ u_y^{\text{SAC}} \leq \bar{u}_y^{\text{SAC}} $	BIP + DOC + SAC

4

Results

This chapter contains results from verification and sensitivity analysis of the system FE-model as well as from the optimizations.

4.1 Verification of FE-model

This section is merely intended to highlight some of the most interesting findings. However, complete results from the verification part is presented in Appendix B. As can be seen in Figures B.1 - B.30, the FE-model tends to have high correlation with the RLD and it captures most tendencies, such as force peaks and valleys. In particular the force signals in the ball joints (HP6) are nearly identical to the RLD for all strength events. The corresponding force signals for BIP are shown in Figure 4.1 and force signals for the other two events are presented in Figures B.14 and B.24.

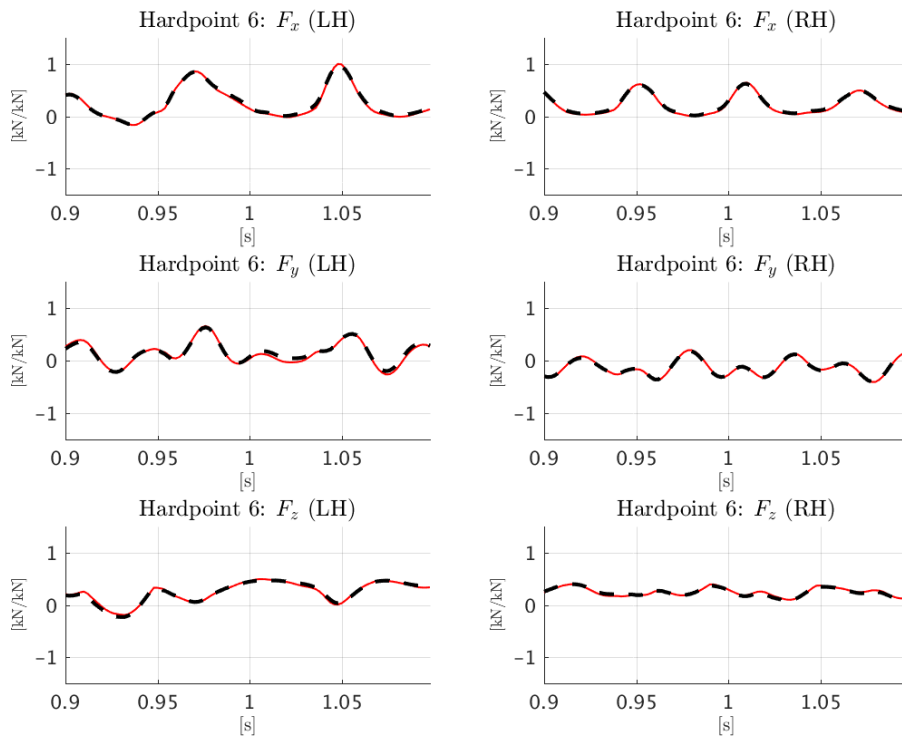


Figure 4.1: Force signals in HP6 during BIP, FE-model (— —) vs RLD (—)

4. Results

The force signals from the FE-model are compared with force signals from the RLD. The largest component from the RLD reaches ± 1 due to normalization in accordance with Equation (3.1).

Normalized RMS values, see Equation (3.2), are presented in Tables 4.1 - 4.3. Note that RMS^{norm} is by no means a perfect measurement of deviation, but together with Figures B.1 - B.30 it can offer some guidance. The correlation is usually very high for $\text{RMS}^{\text{norm}} \leq 10\%$, acceptable for $\text{RMS}^{\text{norm}} \leq 15\%$ and poor if $\text{RMS}^{\text{norm}} \geq 20\%$. Tables 4.1-4.3 also present means of RMS^{norm} , taken over all hardpoints and calculated for each force component. A comparison, with respect to these mean values, between the method that uses drawing state loads and the one that uses pretension forces are presented in Tables B.2, B.4 and B.6. It can be noted that both methods provide similar accuracy.

RMS^{norm} for all force signals during the BIP event is presented in Table 4.1. As can be seen, the correlation is acceptable for all force signals except F_y^{LH} in HP4. It is highlighted in red and discussed further in Section 4.1.1.

Table 4.1: RMS^{norm} for all force signals during the BIP event, with subtraction of drawing state loads

Force HP	F_x^{LH}	F_y^{LH}	F_z^{LH}	F_x^{RH}	F_y^{RH}	F_z^{RH}
HP1	3.2 %	12.5 %	1.0 %	2.2 %	12.3 %	0.8 %
HP3	4.0 %	5.0 %	1.3 %	3.6 %	3.8 %	1.2 %
HP4	2.5 %	26.9 %	3.2 %	1.9 %	7.0 %	0.9 %
HP6	2.7 %	4.0 %	2.7 %	2.1 %	1.3 %	1.9 %
HP7	2.1 %	12.5 %	1.2 %	1.2 %	12.3 %	0.8 %
HP12	1.3 %	8.0 %	1.0 %	1.0 %	5.5 %	0.6 %
HP14	1.7 %	8.0 %	0.8 %	1.2 %	5.6 %	0.5 %
HP18	1.6 %	5.6 %	2.5 %	1.5 %	5.5 %	2.1 %
HP31-32	8.5 %	4.1 %	4.6 %	7.2 %	3.4 %	3.8 %
HP33-34	8.3 %	8.3 %	11.8 %	7.6 %	10.1 %	9.4 %
Mean	3.6 %	9.5 %	3.0 %	3.0 %	6.7 %	2.2 %

RMS^{norm} for all force signals during the DOC event are presented in Table 4.2. Here most force signals shows good correlation as well, but F_y^{LH} and F_y^{RH} in HP4 corresponds to high RMS^{norm} and this is discussed further in Section 4.1.1. F_z^{LH} and F_z^{RH} in HP33-34 are also quite high, but may be considered as acceptable with respect to the simplifications behind the system FE-model.

Table 4.2: RMS^{norm} for all force signals during the DOC event, with subtraction of drawing state loads

Force HP	F_x^{LH}	F_y^{LH}	F_z^{LH}	F_x^{RH}	F_y^{RH}	F_z^{RH}
HP1	1.3 %	2.5 %	0.5 %	1.3 %	2.5 %	0.5 %
HP3	2.5 %	4.0 %	3.3 %	2.5 %	3.9 %	3.3 %
HP4	2.5 %	39.3 %	6.1 %	2.4 %	39.0 %	6.1 %
HP6	2.1 %	2.9 %	4.9 %	2.0 %	2.9 %	4.9 %
HP7	1.1 %	2.4 %	0.6 %	1.1 %	2.4 %	0.6 %
HP12	2.3 %	10.5 %	1.7 %	2.4 %	10.4 %	1.7 %
HP14	2.3 %	10.6 %	1.0 %	2.3 %	10.6 %	1.0 %
HP18	0.9 %	3.9 %	6.0 %	0.9 %	3.9 %	6.0 %
HP31-32	6.7 %	4.5 %	5.8 %	7.1 %	4.9 %	5.7 %
HP33-34	9.7 %	6.3 %	16.6 %	9.2 %	6.0 %	16.8 %
Mean	3.1 %	8.7 %	4.6 %	3.1 %	8.7 %	4.7 %

Table 4.3 presents RMS^{norm} for all force signals during the SAC event. Here most force signals show good correlation as well, but F_x^{LH} and F_y^{LH} in HP3 show poor correlation and this is discussed further in Section 4.1.1. Also note that RMS^{norm} is generally larger for the left hand side than for the right. This is because SAC is an asymmetric strength event where the loads are much larger on the left hand side, that hits the curb.

Table 4.3: RMS^{norm} for all force signals during the SAC event, with subtraction of drawing state loads

Force HP	F_x^{LH}	F_y^{LH}	F_z^{LH}	F_x^{RH}	F_y^{RH}	F_z^{RH}
HP1	0.6 %	0.7 %	0.3 %	0.1 %	0.4 %	0.0 %
HP3	49.5 %	52.3 %	7.1 %	4.8 %	4.9 %	1.4 %
HP4	1.6 %	8.3 %	2.5 %	0.3 %	7.5 %	0.6 %
HP6	6.7 %	5.4 %	5.3 %	0.1 %	0.2 %	0.8 %
HP7	0.6 %	0.7 %	0.3 %	0.1 %	0.4 %	0.0 %
HP12	0.5 %	3.2 %	0.2 %	0.0 %	0.2 %	0.0 %
HP14	0.5 %	3.2 %	0.2 %	0.0 %	0.2 %	0.0 %
HP18	2.8 %	9.4 %	8.3 %	0.2 %	0.7 %	0.5 %
HP31-32	8.6 %	8.4 %	0.9 %	5.8 %	1.5 %	1.4 %
HP33-34	3.5 %	9.9 %	13.0 %	2.0 %	11.0 %	3.6 %
Mean	7.5 %	10.2 %	3.8 %	1.3 %	2.7 %	0.8 %

4.1.1 Force signals with poor correlation

Despite that the correlation looks acceptable overall, there are some exceptions (five out of 180).

The first exception is found in strength event BIP (see Figure 4.2) where F_y^{LH} in HP4 shows an $\text{RMS}^{\text{norm}} = 26.9\%$.

The second and third main exceptions are found during strength event DOC (see Figure 4.2) where both F_y^{LH} and F_y^{RH} in HP4 show poor correlation, with RMS^{norm} of 39.3% and 39.0% respectively.

The poor correlation for lateral forces in HP4 can be referred to cases where the dampers are more active. DOC is associated with large damper loads and in the BIP event these forces are larger for the left hand side than for the right. F_y^{LH} corresponds to the wheel that goes into the pothole while F_y^{RH} corresponds to the wheel that stays on the road surface and therefore shows better correlation with respect to the RLD (see Figure B.3). Also note that HP4 looks better for the SAC event (see Figure B.23) where the damper forces are smaller.

The fourth and fifth main exceptions occurs during SAC, where both F_x^{LH} and F_y^{LH} in HP3 show poor correlation (see Figure 4.2). The corresponding values of RMS^{norm} are 49.5% and 52.3% respectively.

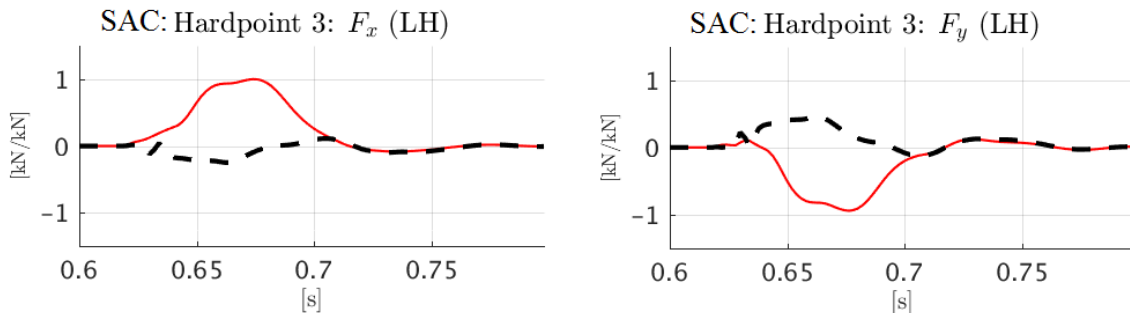


Figure 4.2: High RMS^{norm} : BIP and DOC, FE-model (— —) vs RLD (—)

Figure 4.3: High RMS^{norm} : SAC, FE-model (— —) vs RLD (—)

4.1.2 Static analysis and dynamic events

The developed FE-model is only used during quasi-static analyses, but the applied loads are from dynamic events. Hence, peak loads from the dampers result in unphysical deflections. This effect is most significant during the DOC event, where the large vertical forces statically pushes the LCA down, see Figure 4.4, where the undeformed system (grey) is plotted on top of the deformed (red). Note that, in a dynamic case, the peak damper force mainly acts to decelerate the unsprung mass.

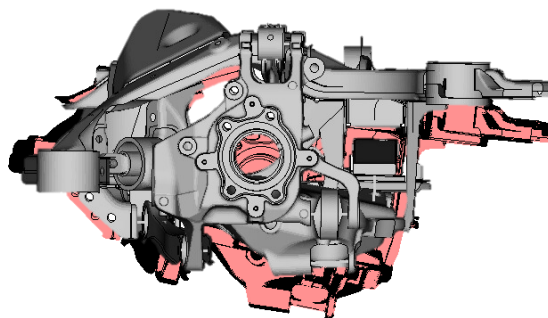


Figure 4.4: Non-physical deflections caused by peak damper loads during DOC

Another noteworthy difference between the quasi-static FE-model and the RLD refers to the difference between load signals for inner and outer hardpoints of the toelink and UCA. Recall that HP12 and HP14 correspond to the outer and inner bushings for the toelink. The corresponding signals for F_z^{RH} during DOC are presented in Figure 4.5. As expected, equilibrium is fulfilled during static analysis of the FE-model. In contrast, the RLD differs between these two hardpoints and there are essentially two probable explanations for this difference; (1) the corresponding local coordinate systems, within the dynamic model, are not perfectly aligned with the global reference frame of the car during the whole event (they rotate with the corresponding bushings) and (2) equilibrium is not present as the component accelerates. The FE-model has fixed coordinate systems and component accelerations are not included in quasi-static analysis.

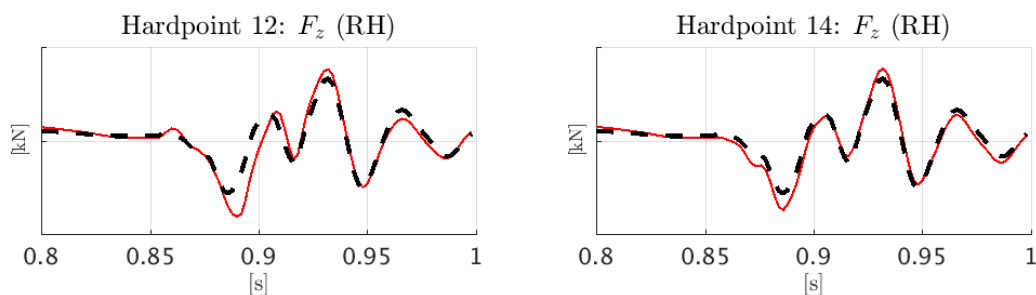


Figure 4.5: F_z^{RH} for DOC: HP12 and 14, FE-model (—) vs RLD (—)

4.1.3 Sensitivity analysis: Bushing stiffness

This section is intended to focus on the most interesting results from the sensitivity analysis with respect to bushing stiffness. However, additional results are found in Appendix C and a summary is presented in Table 4.4. Comments on system response is provided for each bushing stiffness that is varied. The analyzed hardpoints are HP3 and HP4 since these show the highest discrepancy in the verification (see Table 4.1 - 4.3). HP31-34 are also analyzed to investigate the influence of car body bushing stiffness. Over all, the system shows low sensitivity to bushing stiffness, but there are a few exceptions, mainly with respect to bushing stiffness in the local y-directions of HP3 and HP31-32.

Table 4.4: Summary of the system response with respect to bushing stiffness

HP	Stiffness	Event	Comments on system response
3	K_x	BIP	Negligible sensitivity
		DOC	Negligible sensitivity
		SAC	Some sensitivity in HP3, 12 and 14 for low stiffness. Otherwise negligible
	K_y	BIP	Over all high sensitivity for low stiffness. Negligible sensitivity in HP4 and HP31-34
		DOC	Over all high sensitivity for low stiffness. Negligible sensitivity in HP4 and HP31-34
		SAC	Some sensitivity in HP3, 12, 14 and 18 for low stiffness. Otherwise negligible
4	K_x	BIP	Negligible sensitivity
		DOC	Negligible sensitivity
		SAC	Negligible sensitivity
	K_y	BIP	Negligible sensitivity
		DOC	Negligible sensitivity
		SAC	Some sensitivity in HP4. Otherwise negligible
31-32	K_x	BIP	Negligible sensitivity
		DOC	Negligible sensitivity
		SAC	Negligible sensitivity
	K_y	BIP	Some sensitivity in HP31-34. Otherwise negligible
		DOC	Negligible sensitivity
		SAC	High sensitivity in HP31-34 for low and high stiffness. Otherwise negligible
33-34	K_x	BIP	Some sensitivity in HP31-34. Otherwise negligible
		DOC	Negligible sensitivity
		SAC	Some sensitivity in HP31-34. Otherwise negligible
	K_y	BIP	Negligible sensitivity
		DOC	Negligible sensitivity
		SAC	Some sensitivity in HP31-34. Otherwise negligible

As can be seen in Figure 4.6, the bushing stiffness in local y-directions for HP3, has a rather big influence on the system response, particularly for BIP and DOC. For these two events it is clear that a higher stiffness results in a better correlation. This is not the case for SAC. For some hardpoints the correlation is instead slightly better for low stiffnesses. Thus a trade-off has to be made between the different strength events.

The vertical dashed black line seen in the figures represents the value that is used in the FE-model of the system. As explained in Section 3.2.3 the stiffnesses corresponds to bushing specific material data, thus the lowest and highest tangent stiffnesses may differ between hardpoints.

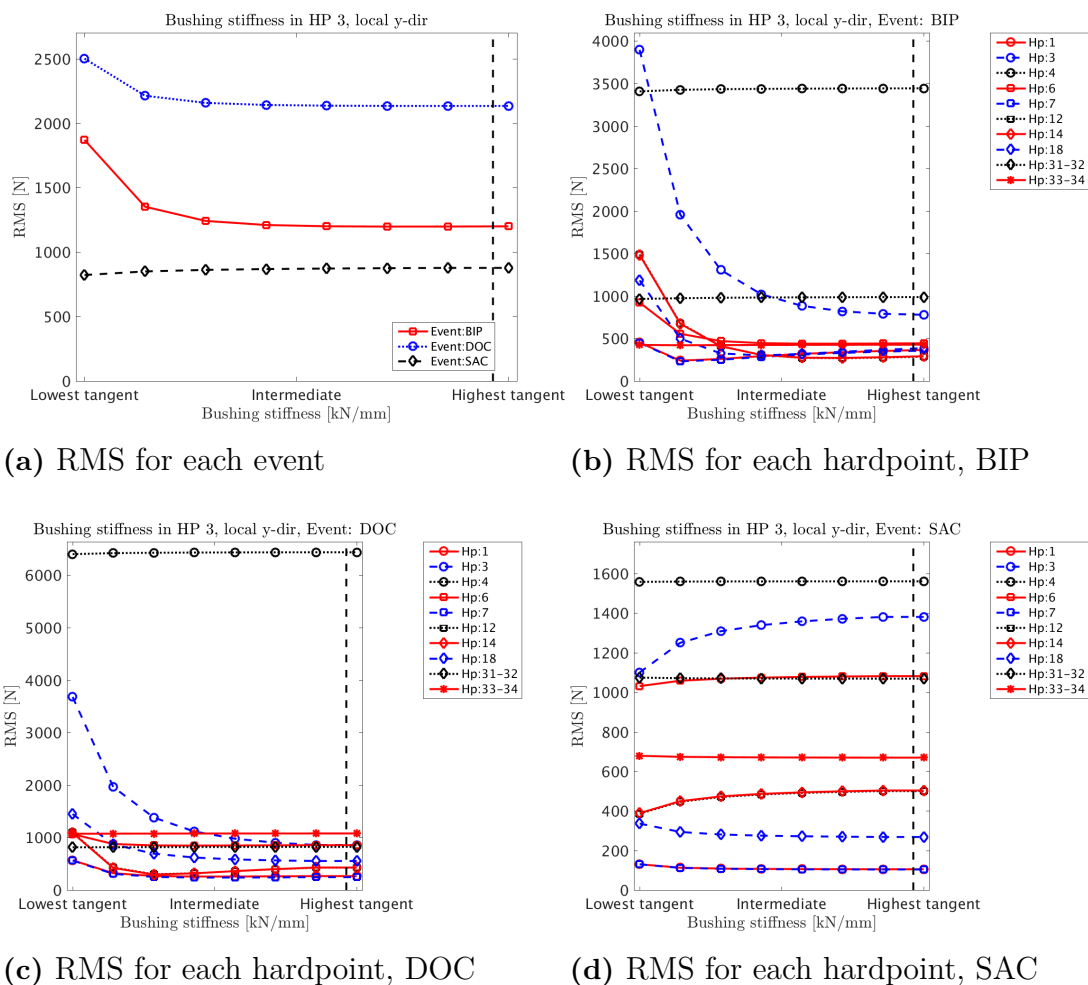


Figure 4.6: System response of bushing stiffness in HP 3 local y-direction

The sensitivity analysis of bushing stiffnesses in HP31-34 examines how sensitive the system is with respect to stiffness of car body bushings, i.e. the boundary conditions.

As mentioned in Table 4.4, changes in car body bushing stiffnesses do not affect force signals in hardpoints for linkages. This can be seen in Figure 4.7, where the stiffness corresponding to the local y-direction in HP31-32, is analyzed. Thus,

4. Results

reasonable changes in stiffness does not affect linkages joints. However, by changing the bushing modeling in hardpoints 31-34 to rigid elements, the correlation gets much poorer in all hardpoints, not just for hardpoints 31-34. An indication to this can be seen in Figure 4.7d where the plot shows that initially the result improves with higher stiffness but eventually starts to worsen. Note that in these figures the 'High' stiffness is very far from rigid.

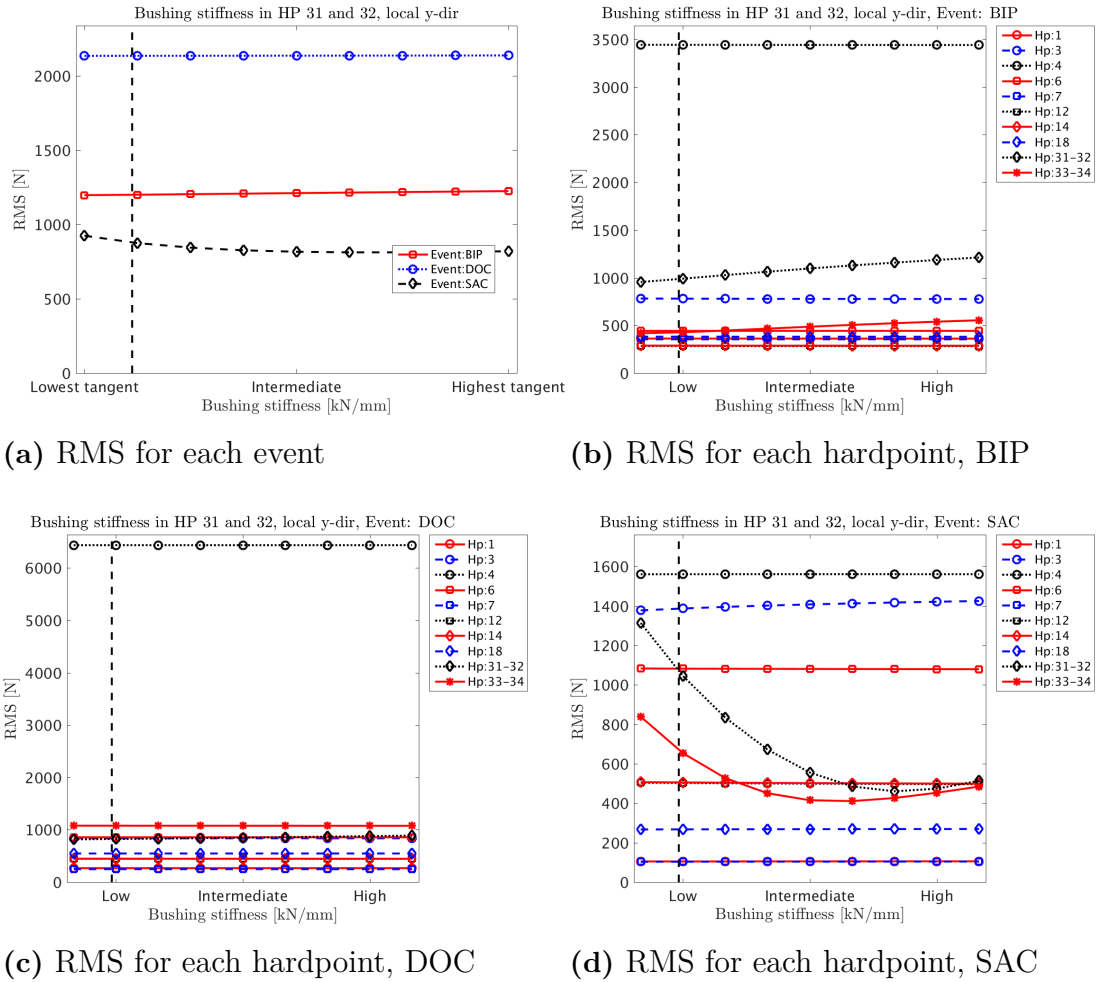


Figure 4.7: System response of bushing stiffness in HP 31-32 local y-direction

The sensitivity analysis shows that the response in the intermediate joint exhibit little sensitivity with respect to the bushing stiffness variation in car body bushings, i.e. HP31-34. Similarly stiffness of bushings for linkages does not seem to affect the reaction forces in HP31-34. It also shows that the system is mainly sensitive for lower stiffnesses and that a trade-off has to be made with respect to RMS values for different strength events.

4.1.4 Sensitivity analysis: Component stiffness

The peak loads shows low sensitivity to component stiffness. This section is therefore limited to only involve results for the combination of hardpoint, component and load case that shows the largest sensitivity, i.e. HP4, LCA and DOC (see Figure 4.8). The results are presented in terms of fractional changes of the largest force magnitude within the hardpoint, all compared with the developed FE-model. The component stiffness is varied with Young's modulus and the force magnitude corresponds to the largest norm that occurs during the event. Hence, the analysis provides a measurement of how sensitive the load distribution is with respect to component stiffness.

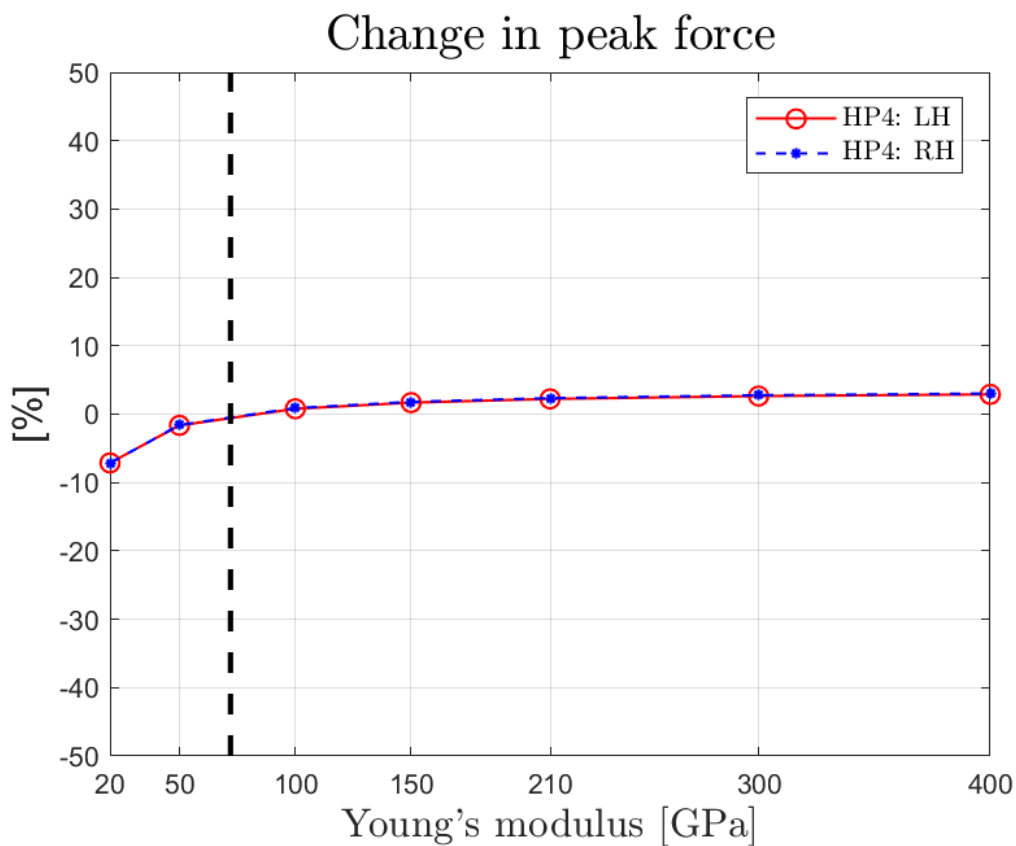


Figure 4.8: Change in peak force in HP4 for DOC when changing the stiffness of the LCA

As can be seen in Figure 4.8, the loads are not very sensitive with respect to component stiffness, at least not for reasonable values of Young's modulus. As a reference the LCA is made of cast aluminum with a Young's modulus of 72 GPa, marked with a vertical dashed line. During TO, the design volumes usually uses much more material than the optimized topology. Hence, the corresponding components are initially very stiff. The stiffness is then reduced as material is removed and the end result can be expected to have a similar stiffness as the reference model. The results indicates that changes in force magnitudes are within a few percent.

4.2 Structural Optimization

This Section presents both the result from the optimization of the simplified model and the result from the FE-model of the optimization of the wheel suspension system.

4.2.1 Optimization of the two-component model

The first optimization involves minimization of system weight, subject to a tip displacement $\Delta \leq 1$ mm for a model with rigid bushings. This setup gives an optimized system mass that changes smoothly with respect to hardpoint position (see 4.9). The corresponding topology evolution is shown in Figure 4.10. As expected, the system needs less weight to fulfill the displacement constraint as the parametrized hardpoint is re-positioned towards the tip. The slope of the curve in Figure 4.9 indicates that systems with structurally inefficient joint positions will gain a larger weight reduction per unit length of repositioning compared to systems with structurally efficient placement of hardpoints.

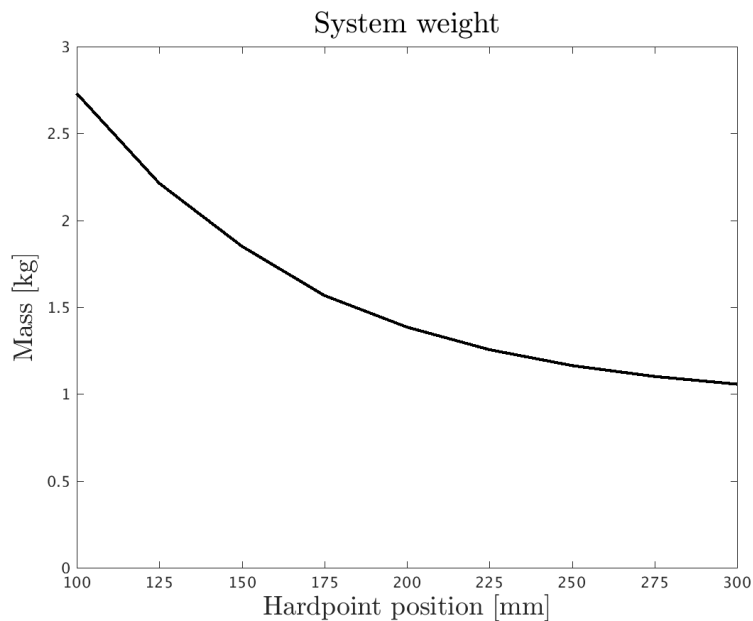


Figure 4.9: Performance plot: Minimize mass (rigid bushings)

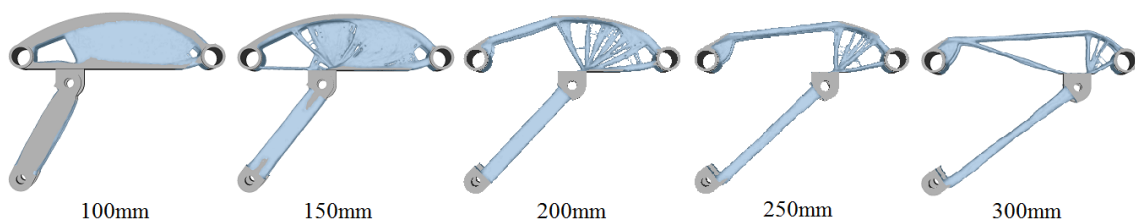


Figure 4.10: Topology evolution: Minimize mass (rigid bushings)

The corresponding optimizations with elastic bushings are shown in Figures 4.11 and 4.12. The optimization setup is minimization of system weight, subject to a tip displacement $\Delta \leq 10$ mm. The constraint is not fulfilled when the hardpoint is too far away from the tip (due to flexibility in the bushings) and the corresponding data points in Figure 4.11 are left out. The change in optimized system weight is rather dramatic for hardpoint positions between 150 mm and 175 mm, then the slope levels out.

Compared to the corresponding result for rigid bushings (see Figures 4.9 and 4.10) it can be seen that the bushing stiffnesses affect the optimization results significantly. The difference in slope (weight reduction per unit length of repositioning) is even greater between structurally inefficient and efficient systems. Another noteworthy difference refers to the geometrical outcomes. By comparing Figure 4.10 with Figure 4.12 it can be seen how reaction moments affect the topology. With rigid bushings the reaction moments on the left boundaries are larger. The corresponding topology is adapted by a slightly off centered lower link, where the adjusted angle favours the vertical support for the system. Similarly the section closest to the left boundary for the upper link is thicker and points slightly upwards (compare with the perfectly horizontal in Figure 4.12.)

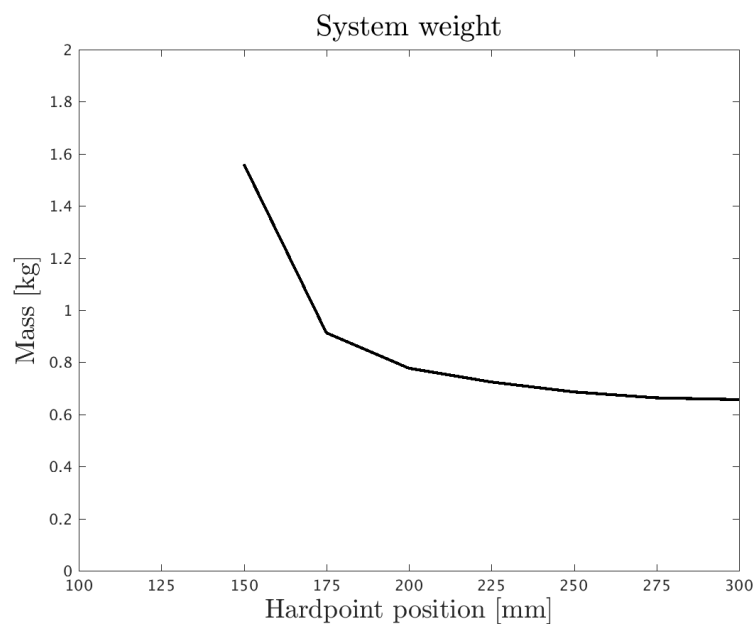


Figure 4.11: Performance plot: Minimize mass (flexible bushings)

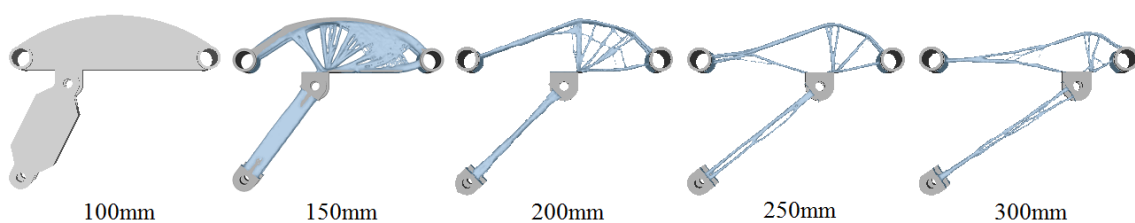


Figure 4.12: Topology evolution: Minimize mass (flexible bushings)

4. Results

For minimum compliance (minimizing strain energy) the strain energy, tip displacement and the outcome topology all behaves smoothly with respect to hardpoint position (see Figures 4.13-4.15).

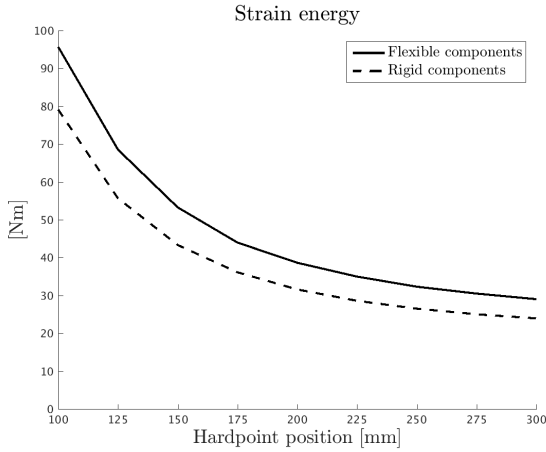


Figure 4.13: Strain energy

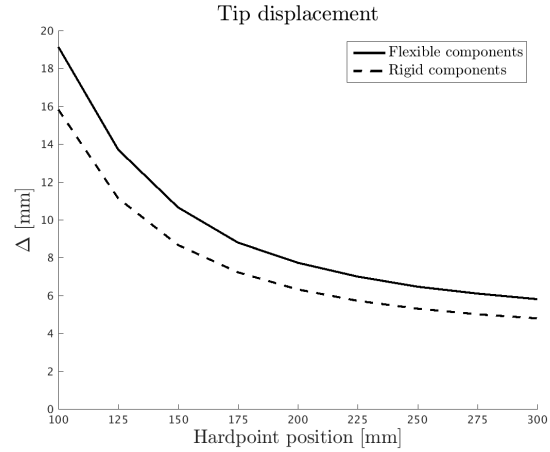


Figure 4.14: Tip Displacement

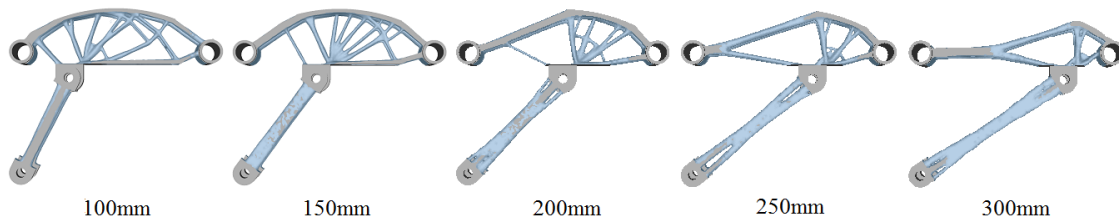


Figure 4.15: Topology evolution: Minimize strain energy (flexible bushings)

Despite that the outcome topologies in Figure 4.15 looks reasonable with respect to design realization, strain energy may not be suitable as a performance measurement. It is not easily understood and may thereby be hard to communicate with other disciplines. However, by comparing Figures 4.13 and 4.14 it can be seen that the strain energy correlates perfectly with the tip displacement. This should be expected for this problem since the strain energy is merely a scaling of the tip displacement, i.e. $0.5F\Delta$.

It should be noted that displacement measurement may be harder to correlate with the strain energy for problems that involves multiple loads, acting on different parts of the boundary. Hence, this requires careful consideration of how load cases and stiffness performance measurements are combined.

4.2.2 TO of the wheel suspension system

The results of the topology optimization of the wheel suspension system of both cases defined in Section 3.3.2.3 are presented in this section. The results are compared to the FE-model presented in Section 4.1, here called the reference model.

4.2.2.1 Case 1

The results from the optimization in case 1 are summarized in Table 4.5 and the resulting topology of the components are presented in Figure 4.16. Note that these are just results from using all concept load cases and that the corresponding results for optimization against single load cases are presented in Appendix D.

Table 4.5: Results from optimization case 1 with all load cases, BIP, DOC and SAC

		Opt system	Ref model	Change
Strain energy [Nm]	BIP	187	187	0.0%
	DOC	227	283	-19.6%
	SAC	404	411	-1.6%
	sum	819	881	-7.0%
Mass [kg]	LCA	5.39	5.22	3.2%
	UCA	0.94	1.19	-20.7%
	Toelink	0.62	0.59	5.0%
	sum	6.95	7.00	-0.7%
Displacements [mm]	$ u_{x,L}^{\text{BIP}} $	14.19	13.98	1.5%
	$ u_{x,R}^{\text{BIP}} $	0.71	0.87	-17.9%
	$ u_{z,L}^{\text{DOC}} $	3.21	2.62	22.6%
	$ u_{z,R}^{\text{DOC}} $	3.30	2.72	21.6%
	$ u_{y,L}^{\text{SAC}} $	6.25	6.06	3.2%
	$ u_{y,R}^{\text{SAC}} $	3.28	3.28	0.1%

In this optimization there are no constraints on displacements but the displacements are still measured and compared to the reference model. As described in Subsection 3.3.2.3 the displacements are measured at the wheel center and in the governing direction of each event. As can be seen in Table 4.5 all but one are larger for the optimized system than for the reference model. However, the strain energy is reduced for load cases DOC and SAC while it remains the same for BIP. Hence, the optimized system is overall stiffer than the reference model. The relative mass distribution between the components is also different, where some of the material from the UCA is redistributed to the toelink and LCA. The sum of the component masses shows that the optimized system converge towards a total mass that lies slightly below the predefined mass constraint. This is discussed further in Section 5.2.2.

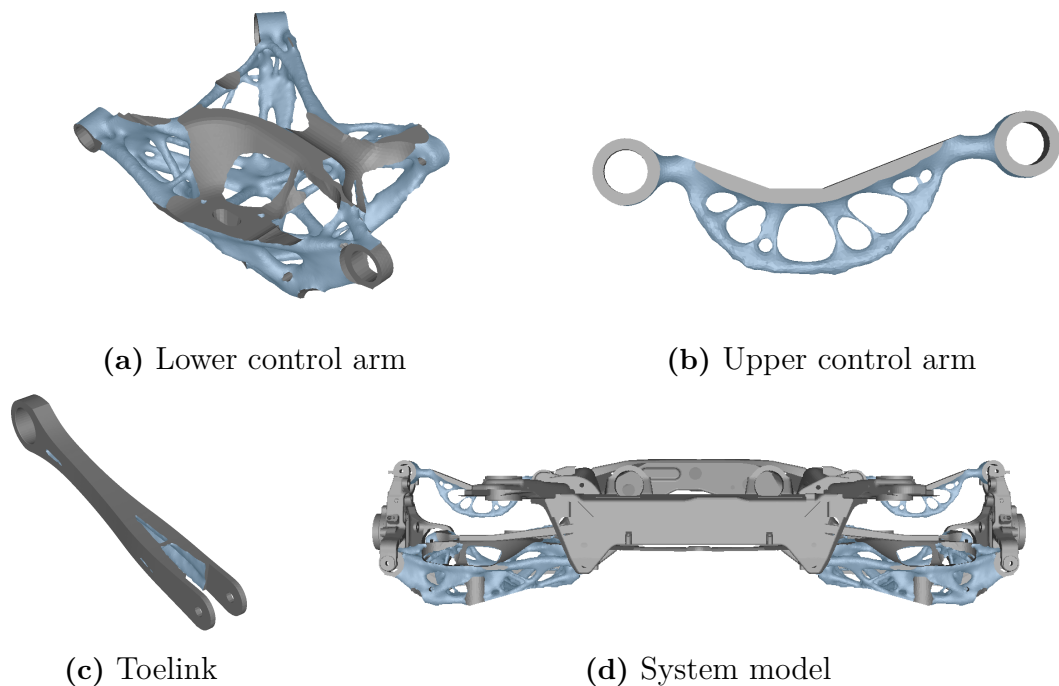


Figure 4.16: Topology of the optimized components for case 1 with all load cases, BIP, DOC and SAC

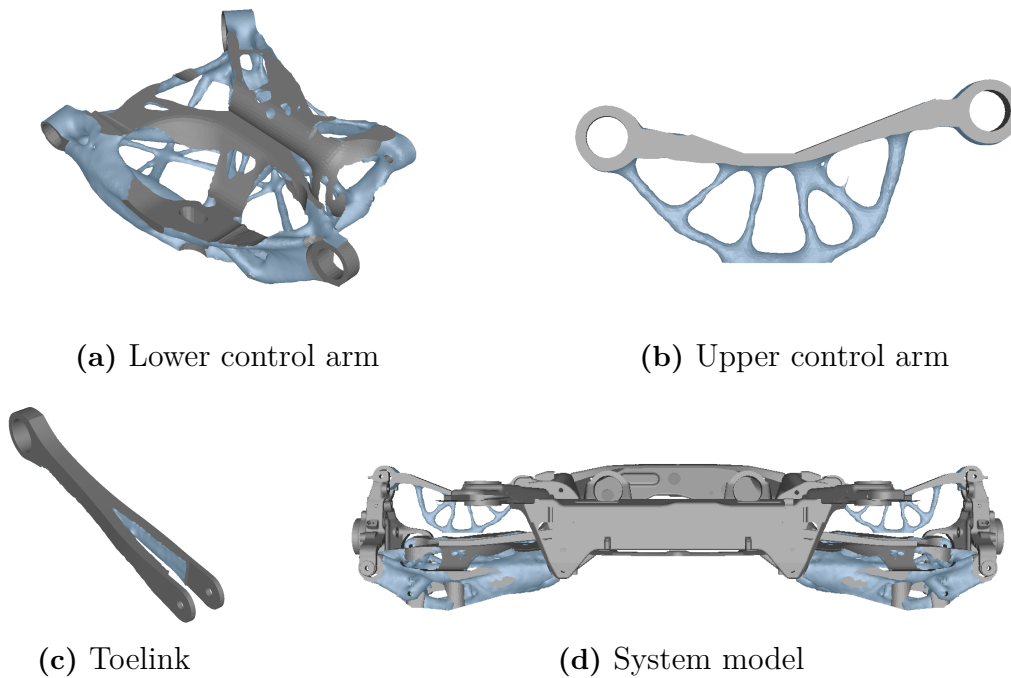
The topology of the components from the optimization with individual load cases are presented in Figures D.1-D.3 in Appendix D. These show how the topology is affected by the different load cases. By comparing these figures it can be noted that high stiffness in the toelink is not very crucial during the DOC event and the toelink is thus very slender. In the SAC event it is instead the LCA that becomes slender while the toelink almost uses all available mass.

4.2.2.2 Case 2

The results from the optimizations in case 2 are summarized in Table 4.6-4.7, where Table 4.6 corresponds to the mass constraint $M \leq \bar{M}$ and the resulting topology of the components are presented in Figure 4.17. Just as in case 1 (where no displacement constraints are added) the relative mass distribution between the links is different from the reference model. However, in this case the redistribution is even more significant, where more mass is redistributed from the UCA to the LCA and toelink. The strain energy is decreased for DOC and SAC, just as in case 1, but here it is also reduced for BIP. The displacements at the wheel center (HP9) are less than for the reference model and thus the constraints are fulfilled.

Table 4.6: Results from optimization case 2, $M \leq \bar{M}^{\text{Ref}}$

		Opt system	Ref model	Change
Strain energy [Nm]	BIP	186	187	-0.4%
	DOC	233	283	-17.5%
	SAC	408	411	-0.7%
	sum	827	881	-6.0%
Mass [kg]	LCA	5.55	5.22	6.4%
	UCA	0.73	1.19	-38.7%
	Toelink	0.66	0.59	13.0%
	sum	6.95	7.00	-0.8%
Displacements [mm]	$ u_{x,L}^{\text{BIP}} $	13.97	13.98	-0.0%
	$ u_{x,R}^{\text{BIP}} $	0.76	0.87	-12.7%
	$ u_{z,L}^{\text{DOC}} $	2.60	2.62	-0.7%
	$ u_{z,R}^{\text{DOC}} $	2.71	2.72	-0.3%
	$ u_{y,L}^{\text{SAC}} $	6.06	6.06	-0.1%
	$ u_{y,R}^{\text{SAC}} $	3.28	3.28	-0.1%

**Figure 4.17:** Topology of the optimized components for case 2 with all load cases, BIP, DOC and SAC

In Table 4.7 the results from the iterations of the mass constraint are summarized. Here the mass constraint ranges from 90 to 50 percent of the reference mass. For each iteration, percentage changes (with respect to the reference model) for strain energy, mass and displacements are presented. With less than 90 percent of the reference mass the sum of the strain energy is above that of the reference model, i.e. the system has become less stiff over all. However, until a mass of only 50 percent, the displacement constraints are still fulfilled. Hence, it may be hard to tell whether the optimized system has the same performance as the reference model. An increased strain energy indicates that the system becomes weaker over all.

Note that the used displacement constraints are just for illustration during this pilot study and may not be interpreted as proper requirements. Some displacements in Table 4.7 behaves rather unpredictable as the mass is reduced. Non-physical deflections of the FE-model may be a contributing factor, but the system in itself is also rather complex. Weakening of links may for example cause the knuckle to rotate such that certain displacements in HP9 are reduced. However, it is clear that the modeled system fails to fulfill the displacements constraints when the mass constraint is at 50 percent of the reference model's. The resulting topology of the components consisting of 60 to 90 percent of the reference model's mass are presented in Figures D.4-D.6 in Appendix D. As the mass is reduced, the rib structure for the LCA becomes more pronounced and the UCA becomes more truss-like.

Table 4.7: Results from optimization case 2, with $M \leq [0.5 - 0.9]\bar{M}^{\text{Ref}}$

		$0.9\bar{M}^{\text{Ref}}$	$0.8\bar{M}^{\text{Ref}}$	$0.7\bar{M}^{\text{Ref}}$	$0.6\bar{M}^{\text{Ref}}$	$0.5\bar{M}^{\text{Ref}}$
Strain energy [Nm]	BIP	0.7%	3.7%	6.8%	19.4%	43.2%
	DOC	-14.0%	-4.5%	4.5%	35.0%	180.4%
	SAC	0.3%	5.4%	9.6%	21.2%	117.1%
	sum	-4.2%	1.9%	7.4%	25.2%	121.7%
Mass [kg]	LCA	-5.3%	-15.1%	-25.8%	-36.2%	-46.6%
	UCA	-40.7%	-49.0%	-53.7%	-60.2%	-70.4%
	Toelink	1.6%	-14.2%	-26.0%	-39.3%	-45.3%
	sum	-10.7%	-20.8%	-30.6%	-40.6%	-50.6%
Displacements [mm]	$ u_{x,L}^{\text{BIP}} $	-0.0%	-0.1%	-0.0%	-0.1%	5.4%
	$ u_{x,R}^{\text{BIP}} $	-2.6%	-0.4%	-0.2%	-0.1%	-3.3%
	$ u_{z,L}^{\text{DOC}} $	-0.7%	-3.0%	-4.4%	-8.2%	-31.6%
	$ u_{z,R}^{\text{DOC}} $	-0.3%	-1.2%	-1.3%	-2.8%	-17.4%
	$ u_{y,L}^{\text{SAC}} $	-0.1%	-0.2%	-0.0%	-0.2%	-10.5%
	$ u_{y,R}^{\text{SAC}} $	-0.1%	-0.2%	-0.6%	-1.3%	-21.4%

5

Discussion

This chapter presents a discussion of outcomes from the project and whether applied methods are suitable for the corresponding methodology. The project aims to propose a methodology that can be used to combine TO with parametrization of joint positions as well as providing a prestudy for future project within this area. In particular the goal is to propose methods for simplified FE-modeling of automotive wheel suspension systems together with concept load cases, as well as studying different optimization strategies. It also aims to provide a pilot study of how the material distribution between linkages can be optimized, with respect to stiffness and weight. Hence, by adopting TO with a system level approach.

5.1 FE-model of the wheel suspension system

The FE-model involves rather many simplifications, e.g. linear geometry and linear bushing characteristics, whereof the most important are discussed in this section. It is important to involve load cases that capture key characteristics of the system, where longitudinal forces are essentially covered by BIP, vertical forces by DOC and lateral forces by SAC. These are expected to capture the most relevant loads at an early stage of development. However, additional load cases such as rolling loads may be introduced as the methods are refined.

5.1.1 Rigid bushing attachments

The proposed FE-model involves rigid behavior between the theoretical centers of bushing bodies and the corresponding interfaces on the components. Hence the model is somewhat over stiff. However, it seems like bushing deflections, i.e. deformations in connector elements, are dominating system level deflections and that the proposed simplification for bushing sleeves seem to be suitable. At least within stiffness analysis.

5.1.2 Quasi-static analysis with linear assumptions

The bushings are modelled with connector elements together with a corresponding connector behavior for linear elastic characteristics. This seems to work well with respect to force signals. Although, it should be emphasized that the model is not validated with respect to displacements and excluding non-linearities may contribute to non-physical system level deflections, which in turn can affect the load distribution within the system. Hence, this may well be a contributing factor to why some load signals shows poor correlation (see Section 4.1.1). However, the deviations of lateral forces in HP4 during BIP and DOC are likely affected by the damper loads (see Figure 4.2). DOC is associated with large damper loads and for BIP event these forces are larger for the left hand side than for the right. In the BIP event, F_y^{LH} corresponds to the wheel that goes into the pothole (see Figure 4.2) while F_y^{RH} corresponds to the wheel that stays on the road surface and therefore shows better correlation with respect to the RLD (see Figure B.3). Also note that HP4 looks better for the SAC event (see Figure B.23) where the damper forces are smaller. Hence, modeling the dampers with external forces may contribute to poor correlation for lateral forces in HP4. Nevertheless, it should be noted that the signals get even worse if damper forces are excluded.

Forces that corresponds to a dynamic event are applied within a quasi-static analysis and the peak damping forces that in a dynamic case act to decelerate unsprung mass, instead act to deform the system statically (see Section 4.1.2). Hence, unreasonable system level deflections may be the common reason behind the force signals with high RMS. It is therefore likely that reasonable displacements will reduce these deviations. Except for non-linearities, Equivalent Static Loads (ESL) [49], i.e. a static load that compensates for mass inertia, may be introduced in order replicate system level deflections during quasi-static analysis.

5.1.3 Boundary conditions and bushing stiffness

The proposed boundary conditions are based on an assumption that the car body can be considered as rigid. However, relative movement between the subframe and the car body depends on stiffness of car body bushings and flexibility in the car body may be compensated by choosing a relatively low tangent stiffness when linearizing the corresponding bushing characteristics. The sensitivity analysis with respect to bushing stiffnesses shows that force signals corresponding to hardpoints for linkages are not sensitive with respect to car body bushing stiffnesses. Similarly, the force signals in the car body bushings are not sensitive with respect to stiffnesses in bushings for linkages. Hence, hardpoints for linkages and hardpoints for car body bushings may be analyzed separately. At least as long as the stiffness magnitudes are reasonable, i.e. somewhere between the lowest and highest tangent stiffness of the corresponding non-linear bushing characteristics.

The sensitivity analysis also shows that the bushing stiffness in HP31-32 can be tuned further in order to reduce RMS of the deviation. This last fine tuning is skipped in order to have a sensitivity analysis that corresponds to the presented FE-model. Hence, only varying one variable at time and having everything else fixed in accordance with the reference model. Updating the reference means that the entire sensitivity analysis should be updated in order to be valid. Hence, requiring a huge amount of computational capacity. Also note that an update would have had negligible affect to the optimizations of linkages since loads in linkages are not sensitive with respect to stiffness in car body bushings.

5.2 TO on system level

The proposed scheme (see Figure 1.1) introduces an outer parametric loop that works around the TO. It may be relatively computationally demanding, but it proves to work well for industrial level applications, i.e. on 3D-structures such as the two-component model. With a well thought out DOE, it should be possible to study trends from repositioning of hardpoints within chassis applications. As a starting point, it seems reasonable to study repositionings of about ± 20 mm in different directions. This is with respect to packaging restrictions and other attributes. It may be possible to gain a relatively large mass reduction per unit length of repositioning within the wheel suspension system. However, the potential mass reduction depends on how structurally efficient the current setup of hardpoint positions is and this needs to be investigated further.

Another essential part is parametrization of the system FE-model, where intersections between design volumes must be avoided. A previous thesis work at Volvo Cars covered a parametric approach for design volumes [14] and it may be possible to adopt some of their methods. They found out that the UCA can gain from having a raised design volume and this should have been expected since it is preferable with a straight UCA. This design is not allowed within the current configuration since it will collide with a body beam. Although, it would be interesting to study if a better solutions for the UCA can be achieved by parametrization of hardpoint positions together with parametrization of design volumes.

Except for a parametric loop that follows a DOE, it is also relevant to consider parametric optimization. It can be implemented in a similar manner, with an outer parametric optimization loop instead of the predefined DOE. In order to get reasonable results, additional constraints should be added in terms of limiting boundaries for each hardpoint position (see Figure 5.2).



Figure 5.1: Straight UCA

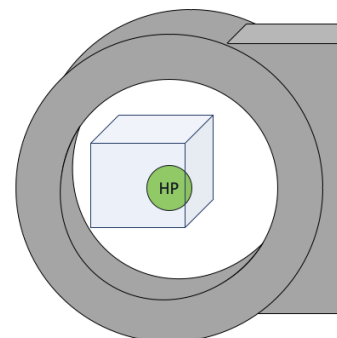


Figure 5.2: Boundary for hardpoint position during parametric optimization

Such a scheme can be useful for fine-tuning of parameters. However, the wheel suspension system is very complex and requirements from multiple disciplines have to be considered. Simply optimizing parameters by only considering structural performance may lead to waste of computational power. Hence, as a starting point it seems more relevant with a well thought out DOE in order to study trends and to provide knowledge about the system.

The future potential for TO on system level seems promising. Optimizations of the two-component model show that a broader solution space through parametrization can lead to decreased system weight. As can be seen for the linkages in Section 4.2.2 the relative mass distribution between different components are treated within one single optimization. Hence, this may reduce iterations during the component phase.

5.2.1 Load distribution during optimization

The mass of the studied suspension system is small in comparison with the total mass that is supported by the rear wheels (about 4-5 %) and component stiffness have been shown to not significantly affect the load distribution. Hence, for given outer loads it seems reasonable that the load distribution remain relatively unchanged during TO. However, the load distribution as well as outer loads to the system may still change with repositioning of hardpoints and this should be investigated further.

5.2.2 Optimization strategies

The over all goal with TO in context with the wheel suspension system is to reduce mass while fulfilling system requirements that are generally formulated as stiffness constraints. Hence, minimize mass subject to stiffness constraints is therefore preferable for evaluation of different hardpoint positions. Minimum compliance is thus not suitable for evaluation of different hardpoint positions when the performance is to be evaluated in terms of optimized mass. However, it may be used for fixed hardpoint positions and is then performed through iteration with lower and lower mass constraint, as for the optimizations in case 2 (see Table 4.7).

Minimum compliance seems to be numerically stable. Numerical difficulties arises when trying to use minimize mass for the wheel suspension model. However, stability is reached when damper loads are removed. Hence, solving the issues with the damper loads is essential for future implementation of the proposed scheme in Figure 1.1. Furthermore, bushing stiffnesses are dominating the strain energy. As a result the derivative of the strain energy with respect to component mass seems to be small in comparison with the total strain energy of the system. In turn, convergence of the optimization problem with respect to strain energy tends to be reached slightly below the given mass constraint. See for example the results in Tables 4.5- 4.6 where the mass of the optimizations tends to be slightly lower than the mass constraint. The difference can be considered as acceptable, but it is still relevant to try alternative convergence conditions.

6

Conclusion

This chapter summarizes the main conclusions of the project and presents recommendations for future follow-up projects. The proposed methodology enables TO to be introduced earlier in the system phase (see proposed workflow for development of wheel suspension systems in Appendix E).

This work resulted in the following main conclusions:

- The proposed modeling of bushing attachments seems to be a reasonable simplification. Bushing deflections are dominating system level deflections and the bushing behavior is more crucial from a stiffness perspective.
- Linear elastic material models for components seem to be a reasonable assumption, but non-linear bushing stiffness and non-linear geometry is interesting to study further.
- The boundary conditions used correspond to an assumption about a rigid car body and that the relative movement between the subframe and the car body depends on bushing stiffness. The physical interpretation is simple and it seems to provide reasonable load signals. Hence, a suitable simplification with respect to an early stage of development.
- Longitudinal forces are essentially covered by BIP, vertical forces by DOC and lateral forces by SAC. These are expected to capture key characteristics of the system at an early stage of development. However, it may be relevant to introduce more load cases with respect to robustness.
- The sensitivity analysis shows that an ansatz about the involved bushing stiffnesses can be made, but that they should neither be chosen too low or too high. Hence, an intermediate stiffness is probably the safest guess. Furthermore, force signals corresponding to hardpoints for linkages are not sensitive with respect to car body bushing stiffnesses and similarly the force signals in the car body bushings are not sensitive with respect to stiffnesses in bushings for linkages.
- Component stiffness does not have a significant effect on the load distribution within the system. Hence, for given outer loads, the load distribution will remain relatively unchanged during TO.

- System requirements are generally formulated as stiffness constraints, why minimize mass together with stiffness constraints are preferable for evaluation of different hardpoint positions. Note that the constraints used within this prestudy is only for illustrative purposes. The constraints should preferably be formulated with respect to requirements for key characteristics of the chassis, e.g. SAC may be associated with a certain camber stiffness.
- Minimize mass subject to stiffness constraints is preferable for evaluation of different hardpoint positions. After all the goal is to reduce mass while fulfilling system requirements.
- The future potential for TO on system level seems promising. In addition to a broader solution space through parametrization of hardpoint positions the relative mass distribution between different components is treated within one single optimization. The proposed scheme introduces an outer parametric loop that works around the TO. With a well thought out DOE, it should be possible to study trends from repositioning of hardpoints within chassis applications. As a starting point, it seems reasonable to study repositionings of about ± 20 mm.

6.1 Further work

The proposed methodology shows future potential, but there are still some areas that need to be addressed. Despite that the FE-model shows good correlation over all, there are some exceptions, i.e. five (out of 180) force signals that show too high RMS. In this context it is relevant to study the influence of non-linearities, such as geometrical non-linearities and non-linear bushing characteristics. It is also relevant to address the issues that refer to the damper loads. A better model may not only be beneficial in terms of correlation, it may also solve the issues with numerical instability for minimizing mass during optimizations. In order to introduce proper stiffness constraints during optimization, there is also a need for correlation of the FE-model with respect to displacements. Furthermore, simplified geometry of design volumes may be essential for a parametrized FE-model of the wheel suspension system. This is not only with consideration to geometrical challenges of having a geometry that follows the hardpoints, meshing and modeling also need to be automatized.

Bibliography

- [1] J. Hofer, E. Wilhelm, W. Schenler, "Comparing the mass, energy, and cost effects of lightweighting in conventional and electric passenger vehicles" *Journal of Sustainable Development of Energy, Water and Environment Systems*, vol. 2, issue 3, pp 284– 295, 2014. doi: 10.13044/j.sdewes.2014.02.0023 [Online].
- [2] Luk, J.M., Kim, H.C., De Kleine, R., Wallington, T.J. and Maclean, H.L. (2017), "Review of the fuel saving, Life cycle GHG emission, and ownership cost impacts of lightweighting vehicles with different powertrains", *Environmental Science and Technology*, Vol. 51 No. 15, pp. 8215-8228, doi: 10.1021/Acs.Est.7b00909 [Online].
- [3] E. Wilhelm, J. Hofer, W. Schenler, "Optimal Lightweighting in Battery Electric and Vehicles", *World Electric Vehicle Journal*, vol. 5, no. 3, pp 751-762, Sep, 2012. doi: 10-3390/wevj5030751 [Online].
- [4] E. Wilhelm, J. Hofer, W. Schenler, and L. Guzzella, "Optimal implementation of lightweighting and powertrain efficiency technology in passengers' vehicles", *Transport*, vol. 27, no. 3, pp. 237-249, Sep, 2012. doi: 10.3846/16484142.2012.719546, [Online].
- [5] I. Gibson, D. W. Rosen, B. & Stucker, *Additive manufacturing technologies: 3D printing, rapid prototyping, and direct digital manufacturing*. 2nd ed. New York, US: Springer-Verlag, 2015
- [6] D. Bracket, I. Ashcroft, and R. Hague, "Topology Optimization for Additive Manufacturing", in *22nd Annual International Solid Freeform Fabrication Symposium(SFF)*, 2011, pp. 348–362. [Online].
- [7] M. E. Orme et al, "Designing for Additive Manufacturing: Lightweighting Through Topology Optimization Enables Lunar Spacecraft", *Journal of Mechanical Design*, vol. 139, no. 10, pp. 1–6, Aug 2017. doi: 10.1115/1.4037304, [Online].
- [8] R. Larsson, "Methodology for topology and shape optimization: Application to a rear lower control arm", MSc thesis, Department of Applied Mechanics, Chalmers University of Technology, Gothenburg, Sweden, 2016. [Online]. Available: <http://studentarbeten.chalmers.se/publication/238778>, Accessed on: Jan 25, 2019.

- [9] N. Kåmark, "Development Process of Topology Optimized Casted Components", MSc thesis, Department of Applied Mechanics, Chalmers University of Technology, Gothenburg, Sweden, 2018. [Online]. Available: <http://studentarbeten.chalmers.se/publication/254903>, Accessed on: Jan 25, 2019.
- [10] T. Ghandriz, "An ALGORITHM FOR STRUCTURAL OPTIMIZATION OF MULTIBODY SYSTEMS", MSc thesis, Department of Numerical Analysis, Lund University, Lund, Sweden, 2014. [Online]. Available: <https://www.lu.se/lup/publication/4939909>, Accessed on: May 7, 2019.
- [11] A. Moghadasi, A. Held, R. Seifried, "Topology Optimization of Flexible Multibody Systems Using Equivalent Static Loads and Displacement Fields", *PAMM: Proceedings in Applied Mathematics & Mechanics*, vol. 14, no. 1, pp. 35–36, Dec. 2014. [online].
- [12] J. Sun, Q. Tian, H. Hu, N.L. Pedersen, "Topology optimization of a flexible multibody system with variable-length bodies described by ALE-ANCF", *Nonlinear Dynamics*, no. 2, pp. 413–441, 2018. [online].
- [13] B. J. Kim et al, "Topology optimization of industrial robots for system-level stiffness maximization by using part-level metamodels", *Structural and Multidisciplinary Optimization*, vol. 54, no 4, pp. 1061-1071, October 2016. [Online]
- [14] K. Bhadin, J. Skön, "Balancing of Wheel Suspension Packaging, Performance and Weight", MSc thesis, Department of Product and Production Development, Chalmers University of Technology, Gothenburg, Sweden, 2016. [Online]. Available: <http://studentarbeten.chalmers.se/publication/238598-balancing-of-wheel-suspension-packaging-performance-and-weight>, Accessed on: Jan 25, 2019.
- [15] P. Ekströmer, S. Schütte, J. Ölvander, "State of the art of generative design and topology optimization and potential reserach needs", *DS:91 Proceedings of NordDesign 2018*, 2018. [online]. Available: <https://www.designsociety.org/publication/40924/State+of+the+art+of+generative+design+and+topology+optimization+and+potential+research+needs>, Accessed on: May 7, 2019.
- [16] H. Chickermane and H. C. Gea, "Design of Multi-Component Structural System for Optimal Layout Topology and Joint Locations," *Engineering with Computers*, vol. 13, no. 2, pp. 235–243, 1997. [online].
- [17] J. Liu, "Guidelines for AM part consolidation", *Virtual & Physical Prototyping*, vol. 11, no. 2, pp. 133–141, 2016. [online].
- [18] Z. Qian and G.K. Ananthasuresh, "Optimal Embedding of Rigid Objects in the Topology Design of Structures", *Mechanics Based Design of Structures & Machines*, vol. 32, no. 2, pp. 165–193, 2004. [online].

-
- [19] L. Qing, G.P Steven, GP and Y.M. Xie, "Evolutionary structural optimization for connection topology design of multi-component systems", *Engineering Computations*, vol. 18, no. 3, p. 460, 2001. [online].
- [20] A. Yildiz and K. Saitou, "Topology Synthesis of Multicomponent Structural Assemblies in Continuum Domains", *Journal of Mechanical Design*, vol. 133, no. 1, p. 11008, 2011. [online].
- [21] J. Hou, J. Zhu, H. F. HE, W. Zhang and W. GUO, "Stiffeners layout design of thin-walled structures with constraints on multi-fastener joint loads", *Chinese Journal of Aeronautics*, vol. 30, no. 4, pp. 1441–1450, 2017. [online].
- [22] J.H. Zhu, J. Hou, W.H. Zhang and Y. Li, "Structural topology optimization with constraints on multi-fastener joint loads", *Structural and Multidisciplinary Optimization*, no. 4, p. 561, 2014. [online].
- [23] H.H. Gao, J.H. Zhu, W.H. Zhang and Y. Zhou, "An improved adaptive constraint aggregation for integrated layout and topology optimization", *Computer Methods in Applied Mechanics and Engineering*, vol. 289, pp. 387–408, 2015. [online].
- [24] Esteco, "modeFrontier | www.esteco.com", 2019. [Online] Available: <https://www.esteco.com/modefrontier>, Accessed on: May 29, 2019.
- [25] Dassault systèmes, "Isight & SIMULIA™ Execution Engine - Dassault Systèmes®", 2019. [Online]. Available: <https://www.3ds.com/products-services/simulia/products/isight-simulia-execution-engine>, Accessed on: May 28, 2019.
- [26] Vanderplaats, "VisualDOC - Vanderplaats", 2019. [Online]. Available: <http://www.vrand.com/products/visualdoc/>, Accessed on: May 29, 2019.
- [27] Altair, "Structural Analysis Solver for Linear & Nonlinear | Altair Optistruct", 2019. [Online]. Available: <https://altairhyperworks.com/product/optistruct>, Accessed on: May 28, 2019.
- [28] Dassault systèmes, "Tosca - The Optimization suite by Dassault Systèmes", 2019. [Online]. Available: <https://www.3ds.com/products-services/simulia/products/tosca>, Accessed on: May 28, 2019.
- [29] Vanderplaats, "GENESIS - Vanderplaats", 2019. [Online]. Available: <http://www.vrand.com/products/genesis/>, Accessed on: May 28, 2019.
- [30] Autodesk, "Generative Design Manufacturing", 2019. [Online]. Available: <https://www.autodesk.com/solutions/generative-design/manufacturing>, Accessed on: May 29, 2019.
- [31] ParaMatters INC, "ParaMatters", 2019. [Online]. Available: <https://paramatters.com>, Accessed on: May 29, 2019.

- [32] Siemens, "Generative Design | Tools & Software | Siemens PLM, 2019. [Online]. Available: <https://www.plm.automation.siemens.com/global/en/products/mechanical-design/generative-design.html>, Accessed on: May 29, 2019.
- [33] Dassault Systèmes, "Abaqus Unified FEA - SIMULIA™ by Dassault Systèmes", 2002. [Online]. Available: <https://www.3ds.com/products-services/simulia/products/abaqus>, Accessed on: Nov 13, 2018.
- [34] MSC Software, "Adams - The Multibody Dynamics Simulation Solution", 2019. [Online]. Available: <http://www.mscsoftware.com/product/adams>, Accessed on: Nov 13, 2018.
- [35] G. Genta and L. Morello *The automotive chassis. Vol. 1, Components design*. London: Springer, 2008.
- [36] Volvo Car Group, "The all-new Volvo XC90 - Rear suspension - Volvo Car Group - Global Media Newsroom", 2014. [Online]. Available: <https://www.media.volvocars.com/global/en-gb/media/photos/149308/the-all-new-volvo-xc90-rear-suspension>
- [37] N. Ottosen and H. Petersson *Introduction to the Finite Element Method*. New Jersey, US: Prentice Hall, 1992.
- [38] N.-H. Kim *Introduction to Nonlinear Finite Element Analysis*. [electronic resource]. Boston, MA: Springer US: Imprint: Springer, 2015. Available: <http://proxy.lib.chalmers.se/login?url=http://search.ebscohost.com/login.aspx?direct=true&db=cat06296a&AN=clc.b2100349&lang=sv&site=eds-live&scope=site>, Accessed on: Feb 23 2019.
- [39] J. N. Reddy *An introduction to continuum mechanics: with applications*. New York: Cambridge University Press, 2008.
- [40] P. W. Christensen and A. Klarbring, *An Introduction to Structural Optimization*, Vol 153. Springer 2009.
- [41] O. Sigmund. "On the usefulness of non-gradient approaches in topology optimization", *Structural and Multidisciplinary Optimization*, vol. 43, no. 5, pp. 589-596, May 2011. doi:10.1007/s00158-011-0638-7 [Online].
- [42] T.Y. Chen and Y. H. Chiou, "Structural Topology Optimization Using Genetic Algorithms", in *Proceedings of the World Congress on Engineering*, 2013, pp. 1933-1937. [Online].
- [43] G.-C. Luh and C.-Y. Lin, "Structural topology optimization using ant colony optimization algorithm", *Applied Soft Computing*, vol. 9 no. 4 pp 1343-1353, September 2009. [Online].

- [44] G.-C. Luh et al, "A binary particle swarm optimization for continuum structural topology optimization", *Applied Soft Computing*, vol. 11, no 2, pp. 2833-2844, March 2011. [Online].
- [45] K. Svanberg, "The Method of Moving Asymptotes - A new method for structural optimization", *International journal for numerical methods in engineering*, vol. 24, no 2, pp. 359-373, Feb 1987.
- [46] M. P. Bendsoe and O. Sigmund, *Topology Optimization: Theory, methods, and applications*, 2nd ed., Berlin, Germany: Springer-Verlag, 2004.
- [47] M. P. Bendsoe and O. Sigmund, "Material interpolation schemes in topology optimization", *Archive of Applied Mechanics*, vol 69, no. 9-10, pp. 635-654, Nov 1999. [Online].
- [48] Dassault Systèmes, "SIMULIA User Assistance 2018". [Online].
- [49] E. P. Hong et al, "Optimization of flexible components of multibody systems via equivalent static loads", *Structural and Multidisciplinary Optimization*, vol 40, no. 1, pp 549-562, Jan 2010. [Online].

A

Linearization of bushing characteristics

This chapter presents the linearized bushing characteristics that are used in the FE-model. Figures A.1 - A.7 show linear bushing characteristics plotted against the non-linear models that are used during dynamic simulations. Translational stiffness characteristics are described by force-displacement curves while rotational stiffness characteristics are described by moment-rotation curves. Axis scales are hidden in order to protect corporate data, but the plots still capture the essential characteristics for the methodology, i.e. how to linearize the non-linear behaviours. It can be noted that rotational stiffnesses uses the initial (low) stiffnesses around the origin, while the translational stiffnesses are chosen to some value between the lowest and highest tangent of the corresponding bushing characteristics.

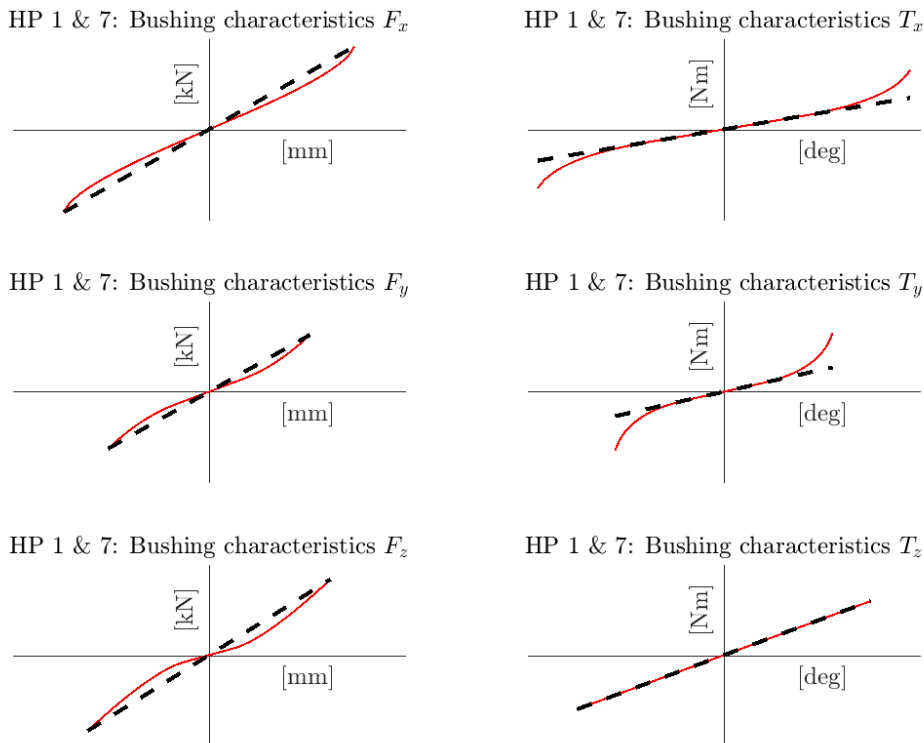


Figure A.1: Bushing characteristics: HP1 & 7, FE-model (— —) vs RLD (—)

A. Linearization of bushing characteristics

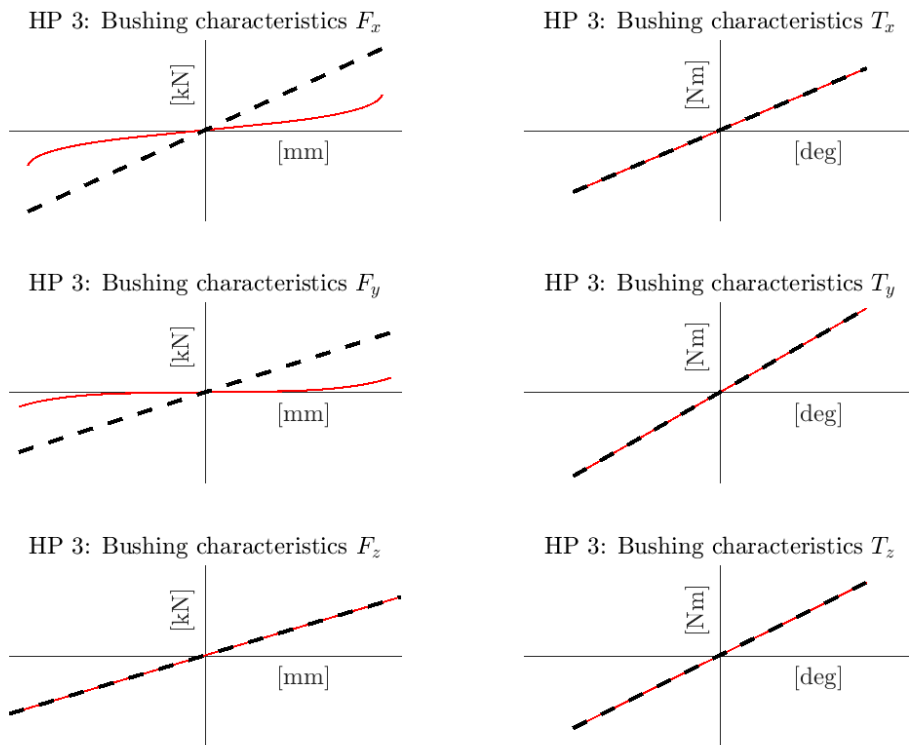


Figure A.2: Bushing characteristics: HP3, FE-model (— —) vs RLD (—)

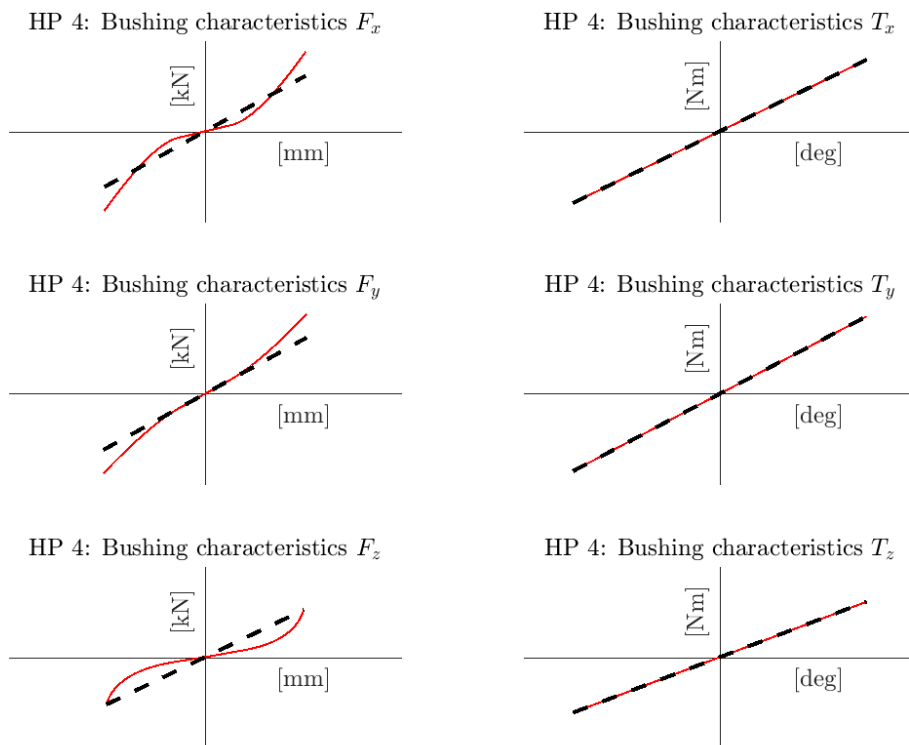


Figure A.3: Bushing characteristics: HP4, FE-model (— —) vs RLD (—)

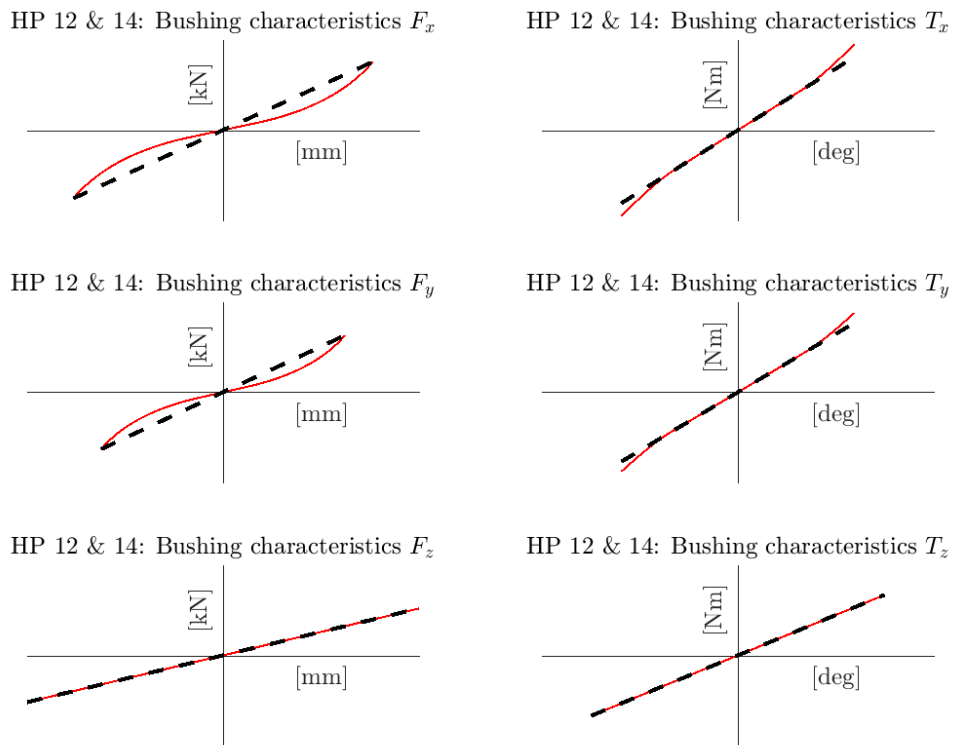


Figure A.4: Bushing characteristics: HP12 & 14, FE-model (— —) vs RLD (—)

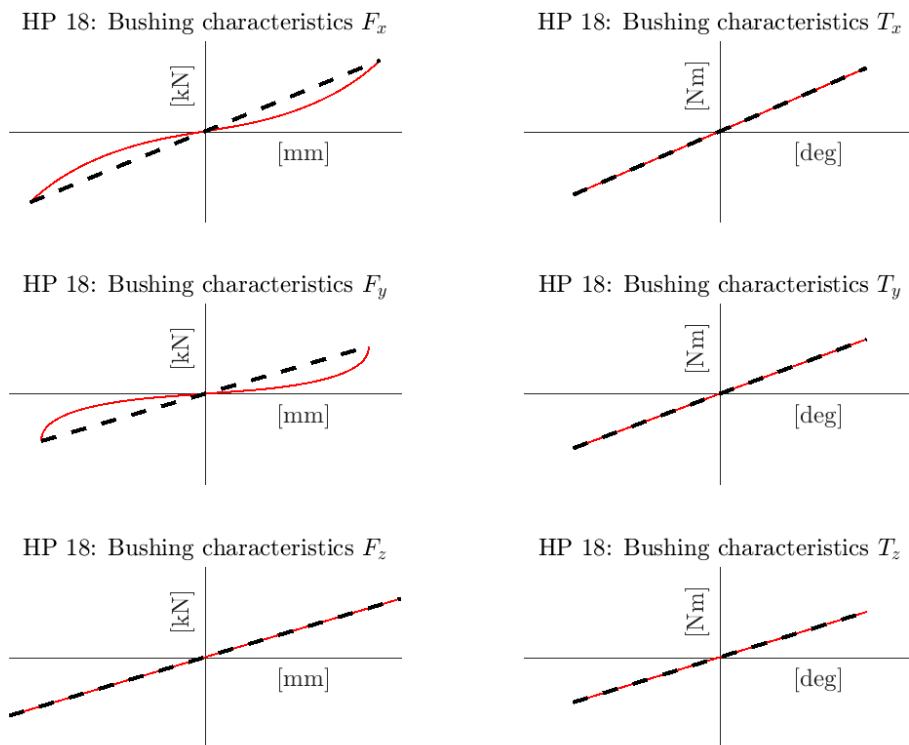


Figure A.5: Bushing characteristics: HP18, FE-model (— —) vs RLD (—)

A. Linearization of bushing characteristics

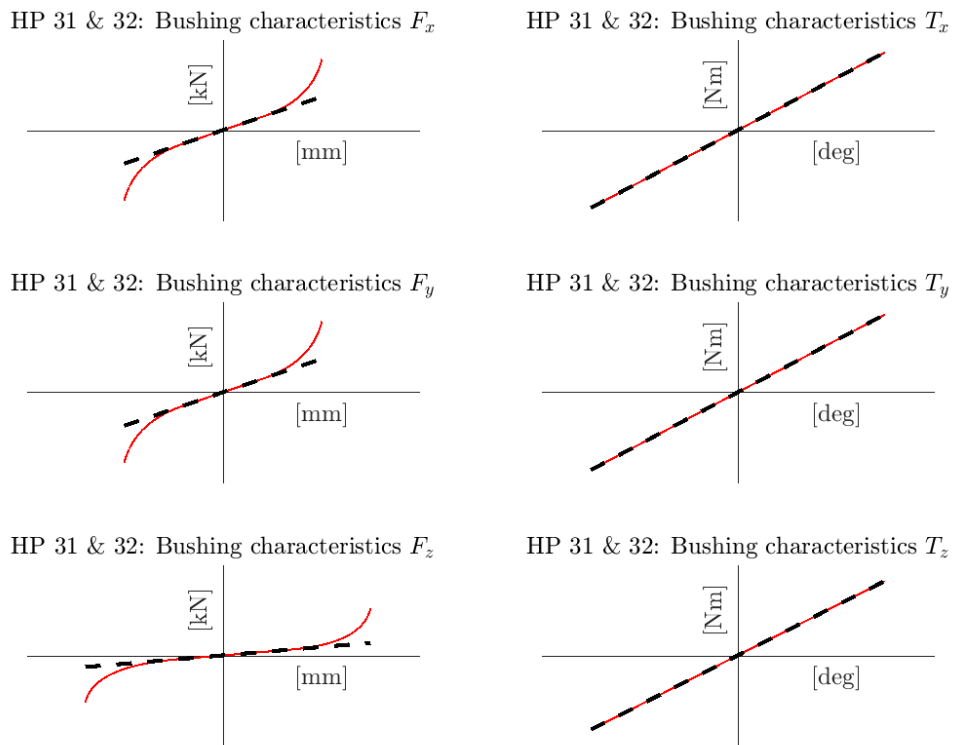


Figure A.6: Bushing characteristics: HP31 & 32, FE-model (— —) vs RLD (—)

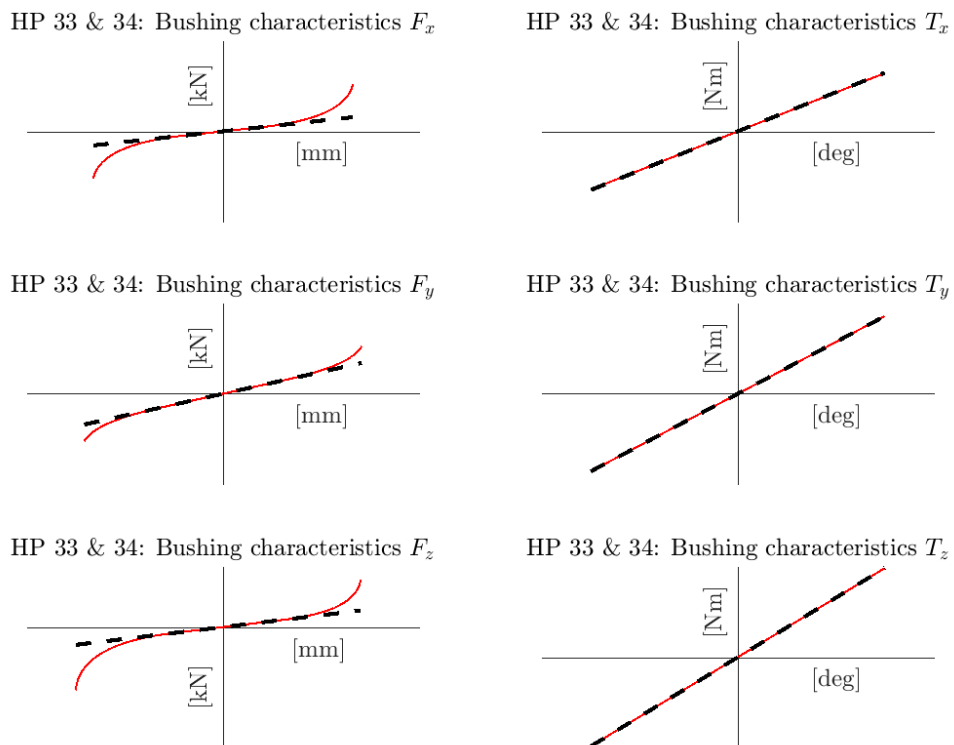


Figure A.7: Bushing characteristics: HP33 & 34, FE-model (— —) vs RLD (—)

B

Results from verification of FE-model

This chapter contains complete results from verification of the developed FE-model, including correlation plots from all three strength events, i.e. BIP, DOC and SAC. Note that all plots are for drawing state loads, but numerical comparison against the use of pretension forces are also presented.

Figures B.1 - B.10 show the correlation plots for BIP and the corresponding RMS values are presented in Table B.1. Table B.2 shows a comparison between drawing state loads and pretension forces.

Table B.1: RMS^{norm} for all force signals during the BIP event, with subtraction of drawing state loads

Force HP	F_x^{LH}	F_y^{LH}	F_z^{LH}	F_x^{RH}	F_y^{RH}	F_z^{RH}
HP1	3.2 %	12.5 %	1.0 %	2.2 %	12.3 %	0.8 %
HP3	4.0 %	5.0 %	1.3 %	3.6 %	3.8 %	1.2 %
HP4	2.5 %	26.9 %	3.2 %	1.9 %	7.0 %	0.9 %
HP6	2.7 %	4.0 %	2.7 %	2.1 %	1.3 %	1.9 %
HP7	2.1 %	12.5 %	1.2 %	1.2 %	12.3 %	0.8 %
HP12	1.3 %	8.0 %	1.0 %	1.0 %	5.5 %	0.6 %
HP14	1.7 %	8.0 %	0.8 %	1.2 %	5.6 %	0.5 %
HP18	1.6 %	5.6 %	2.5 %	1.5 %	5.5 %	2.1 %
HP31-32	8.5 %	4.1 %	4.6 %	7.2 %	3.4 %	3.8 %
HP33-34	8.3 %	8.3 %	11.8 %	7.6 %	10.1 %	9.4 %
Mean	3.6 %	9.5 %	3.0 %	3.0 %	6.7 %	2.2 %

Table B.2: Comparison of mean RMS^{norm} during BIP

Force Method	F_x^{LH}	F_y^{LH}	F_z^{LH}	F_x^{RH}	F_y^{RH}	F_z^{RH}
Drawing state loads	3.6 %	9.5 %	3.0 %	3.0 %	6.7 %	2.2 %
Pretension forces	3.7 %	10.5 %	3.0 %	3.2 %	7.9 %	2.3 %

B. Results from verification of FE-model

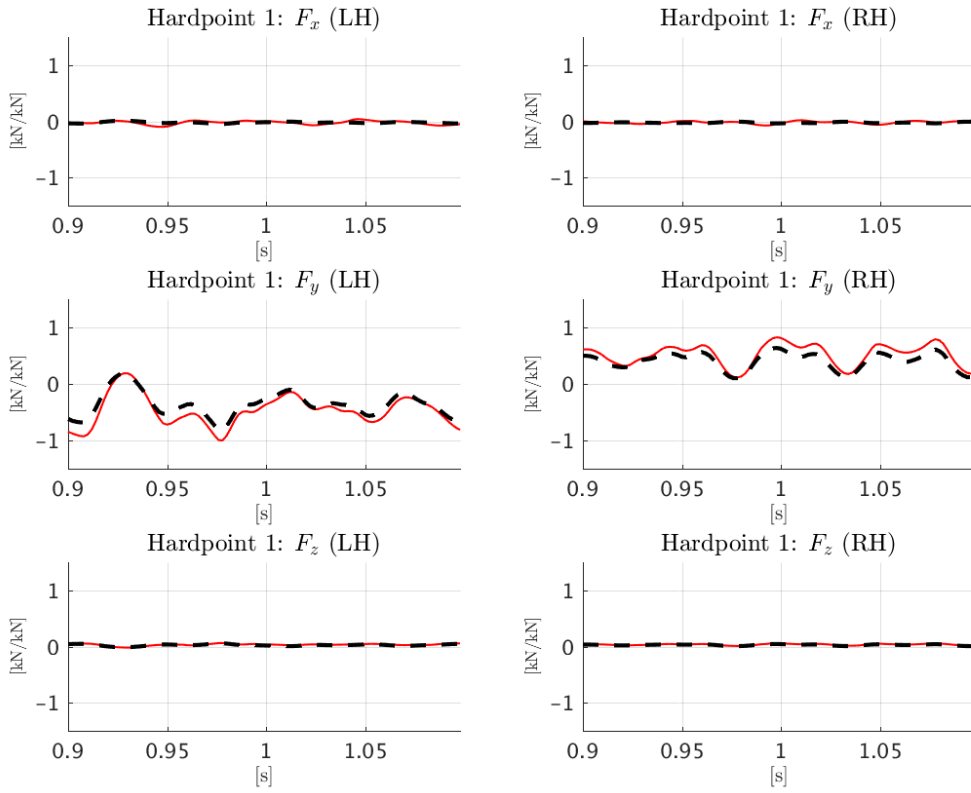


Figure B.1: F^{norm} in HP1 during BIP, FE-model (— —) vs RLD (—)

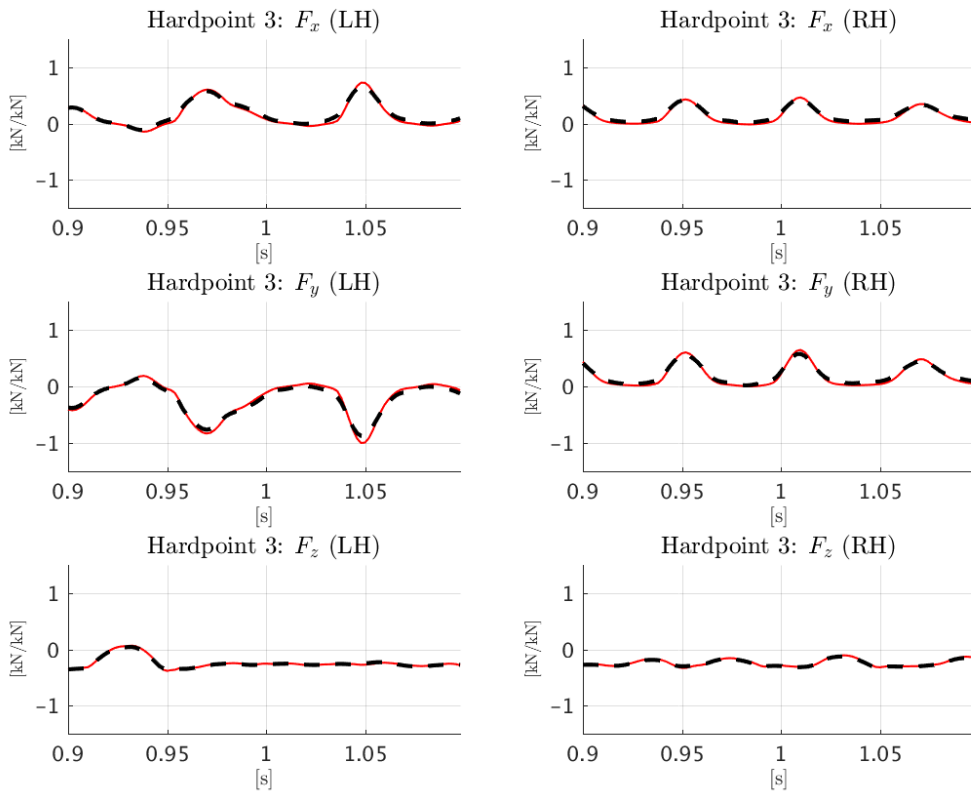


Figure B.2: F^{norm} in HP3 during BIP, FE-model (— —) vs RLD (—)

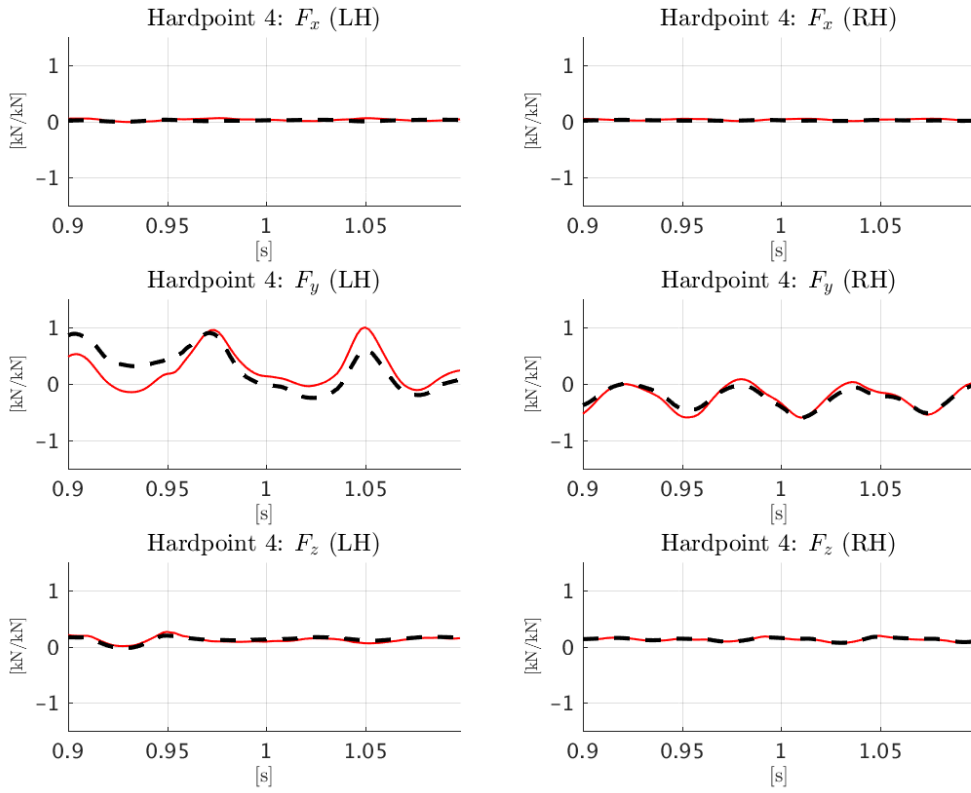


Figure B.3: F^{norm} in HP4 during BIP, FE-model (— —) vs RLD (—)

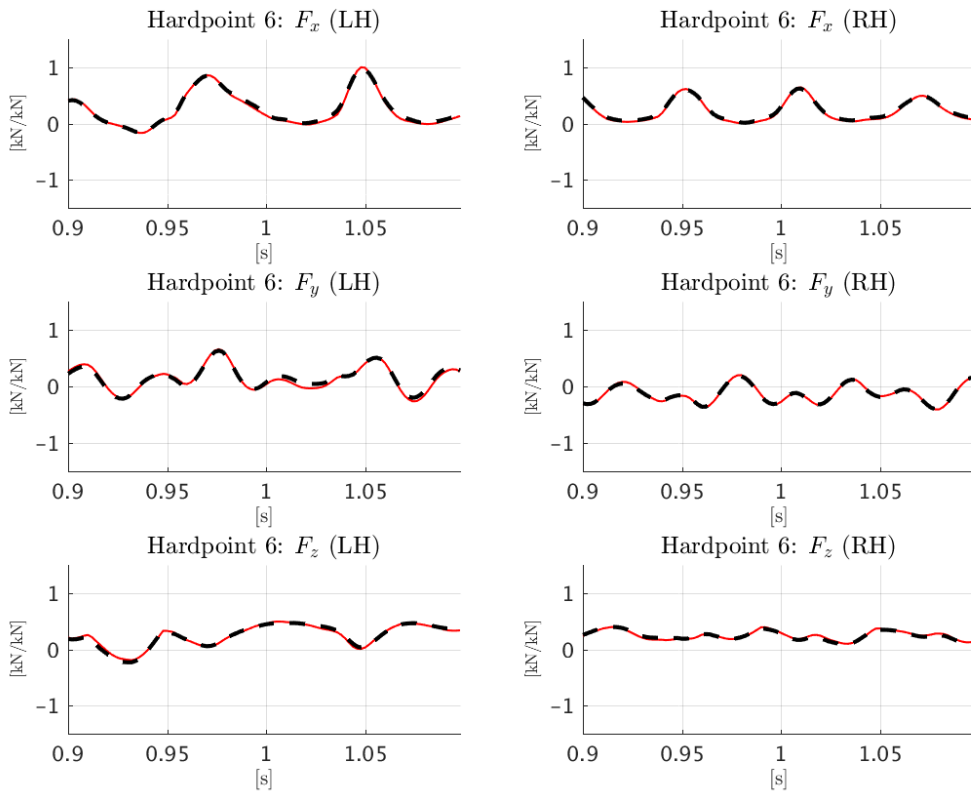


Figure B.4: F^{norm} in HP6 during BIP, FE-model (— —) vs RLD (—)

B. Results from verification of FE-model

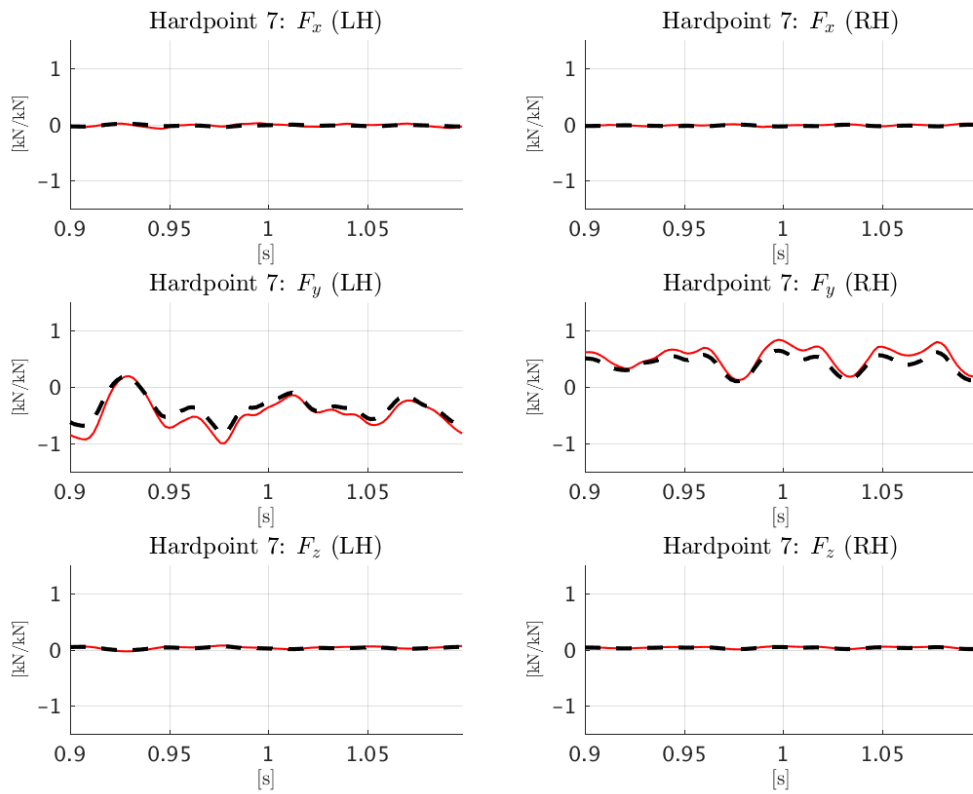


Figure B.5: F^{norm} in HP7 during BIP, FE-model (— —) vs RLD (—)

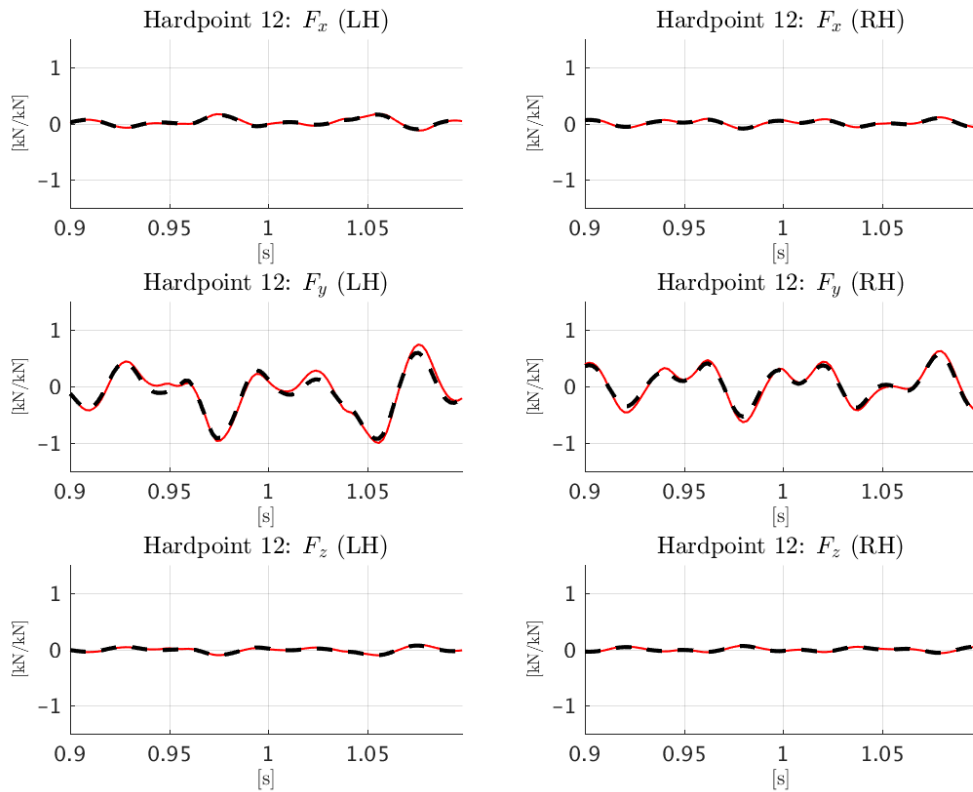


Figure B.6: F^{norm} in HP12 during BIP, FE-model (— —) vs RLD (—)

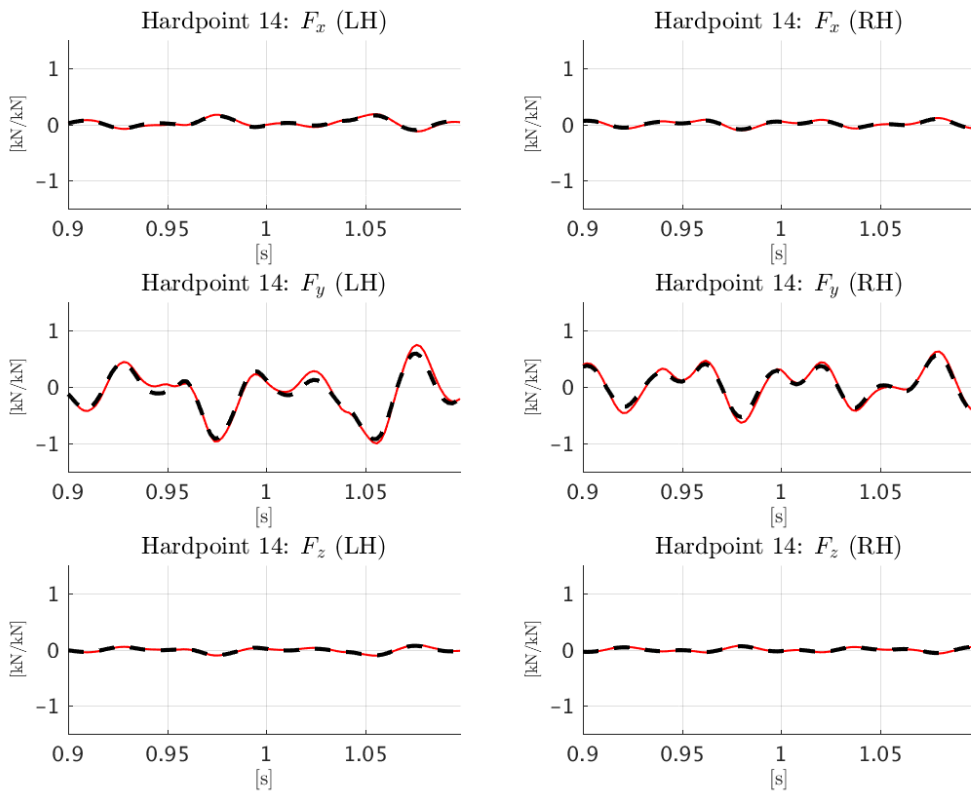


Figure B.7: F^{norm} in HP14 during BIP, FE-model (— —) vs RLD (—)

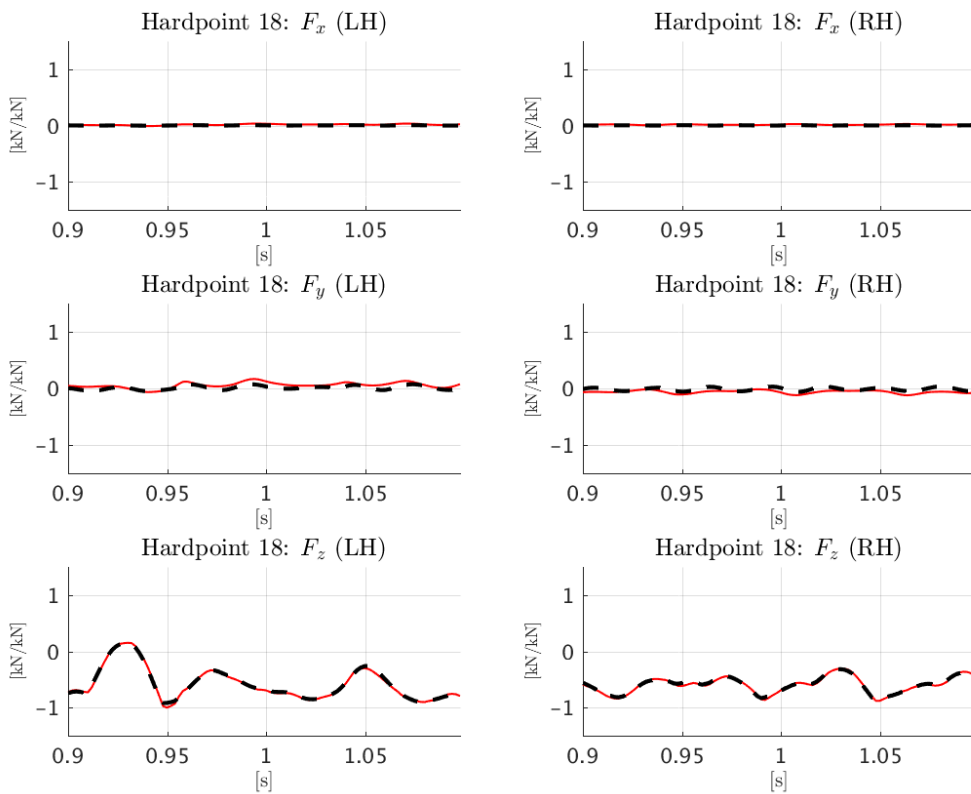


Figure B.8: F^{norm} in HP18 during BIP, FE-model (— —) vs RLD (—)

B. Results from verification of FE-model

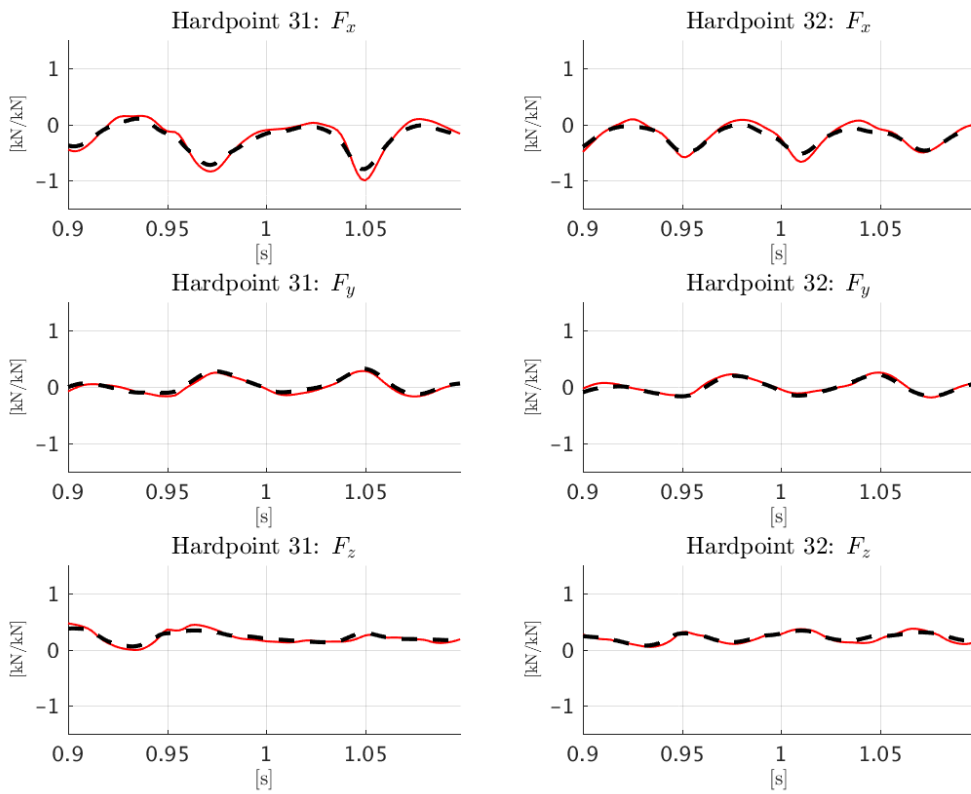


Figure B.9: F^{norm} in HP31-32 during BIP, FE-model (— —) vs RLD (—)

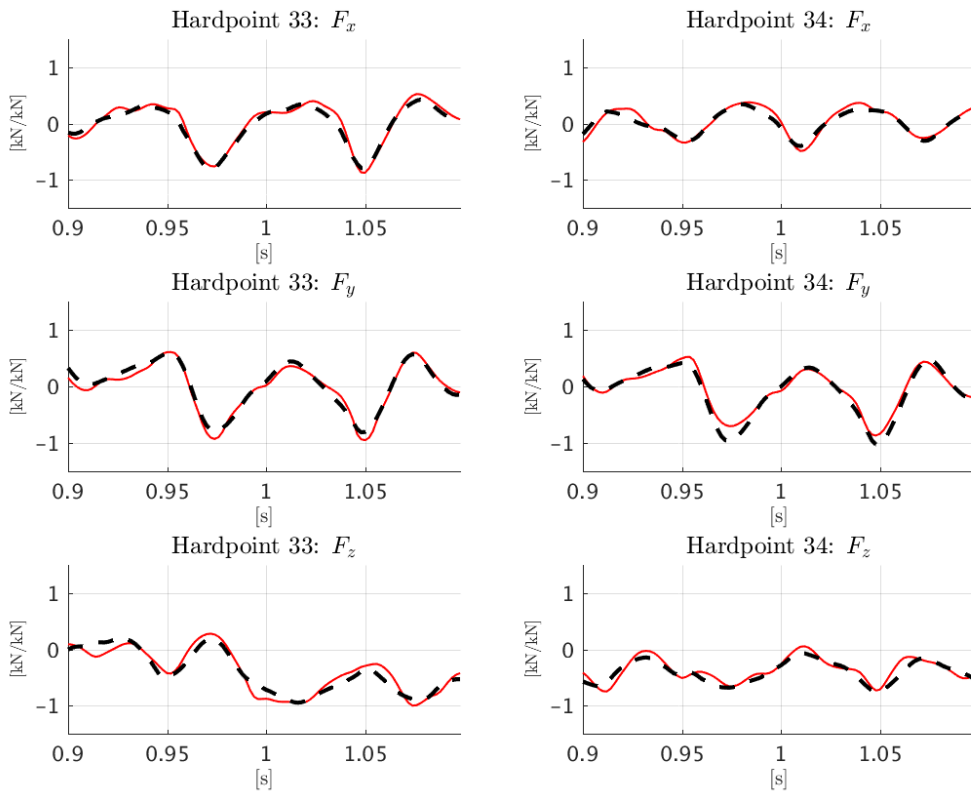


Figure B.10: F^{norm} in HP33-34 during BIP, FE-model (— —) vs RLD (—)

Figures B.11 - B.20 show the correlation plots for DOC and the corresponding RMS values are presented in Table B.3. Table B.4 shows a comparison between drawing state loads and pretension forces.

Table B.3: RMS^{norm} for all force signals during the DOC event, with subtraction of drawing state loads

Force HP	F_x^{LH}	F_y^{LH}	F_z^{LH}	F_x^{RH}	F_y^{RH}	F_z^{RH}
HP1	1.3 %	2.5 %	0.5 %	1.3 %	2.5 %	0.5 %
HP3	2.5 %	4.0 %	3.3 %	2.5 %	3.9 %	3.3 %
HP4	2.5 %	39.3 %	6.1 %	2.4 %	39.0 %	6.1 %
HP6	2.1 %	2.9 %	4.9 %	2.0 %	2.9 %	4.9 %
HP7	1.1 %	2.4 %	0.6 %	1.1 %	2.4 %	0.6 %
HP12	2.3 %	10.5 %	1.7 %	2.4 %	10.4 %	1.7 %
HP14	2.3 %	10.6 %	1.0 %	2.3 %	10.6 %	1.0 %
HP18	0.9 %	3.9 %	6.0 %	0.9 %	3.9 %	6.0 %
HP31-32	6.7 %	4.5 %	5.8 %	7.1 %	4.9 %	5.7 %
HP33-34	9.7 %	6.3 %	16.6 %	9.2 %	6.0 %	16.8 %
Mean	3.1 %	8.7 %	4.6 %	3.1 %	8.7 %	4.7 %

Table B.4: Comparison of mean RMS^{norm} during DOC

Method \ Force	F_x^{LH}	F_y^{LH}	F_z^{LH}	F_x^{RH}	F_y^{RH}	F_z^{RH}
Drawing state loads	3.1 %	8.7 %	4.6 %	3.1 %	8.7 %	4.7 %
Pretension forces	3.1 %	8.9 %	4.4 %	3.1 %	8.8 %	4.4 %

B. Results from verification of FE-model

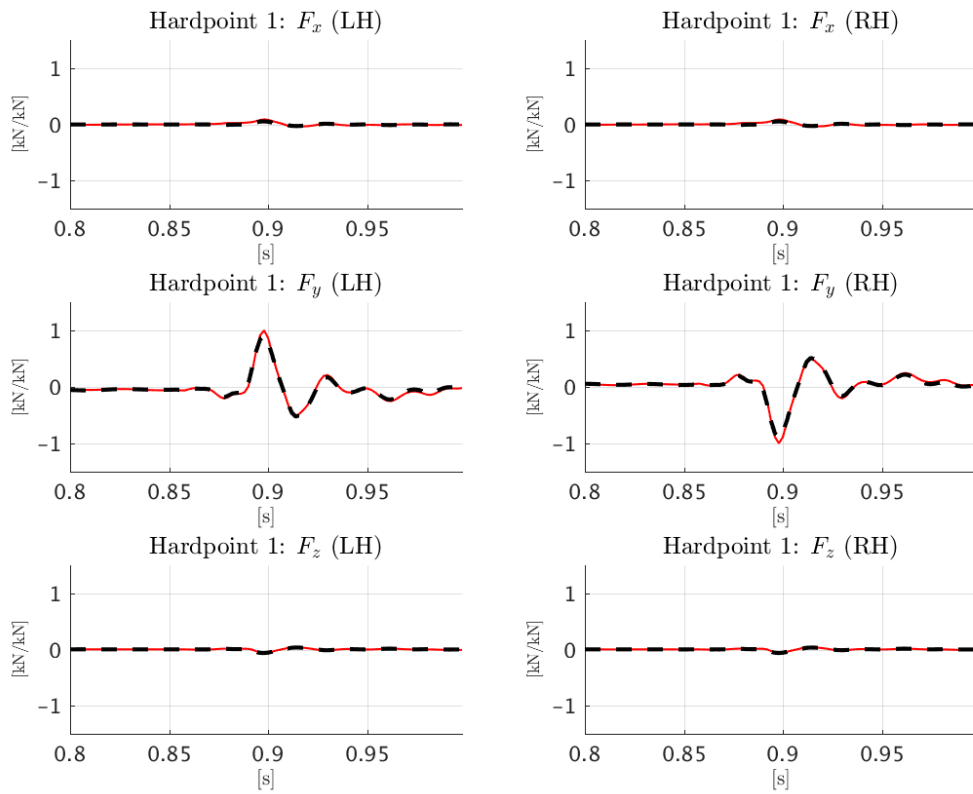


Figure B.11: F^{norm} in HP1 during DOC, FE-model (— —) vs RLD (—)

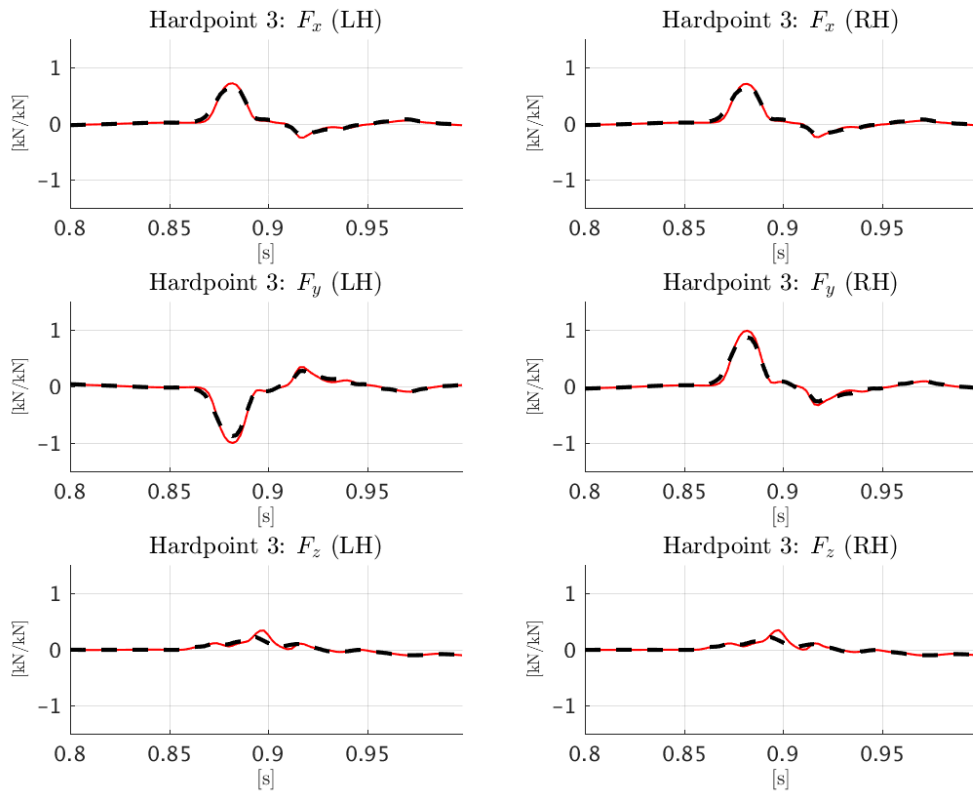


Figure B.12: F^{norm} in HP3 during DOC, FE-model (— —) vs RLD (—)

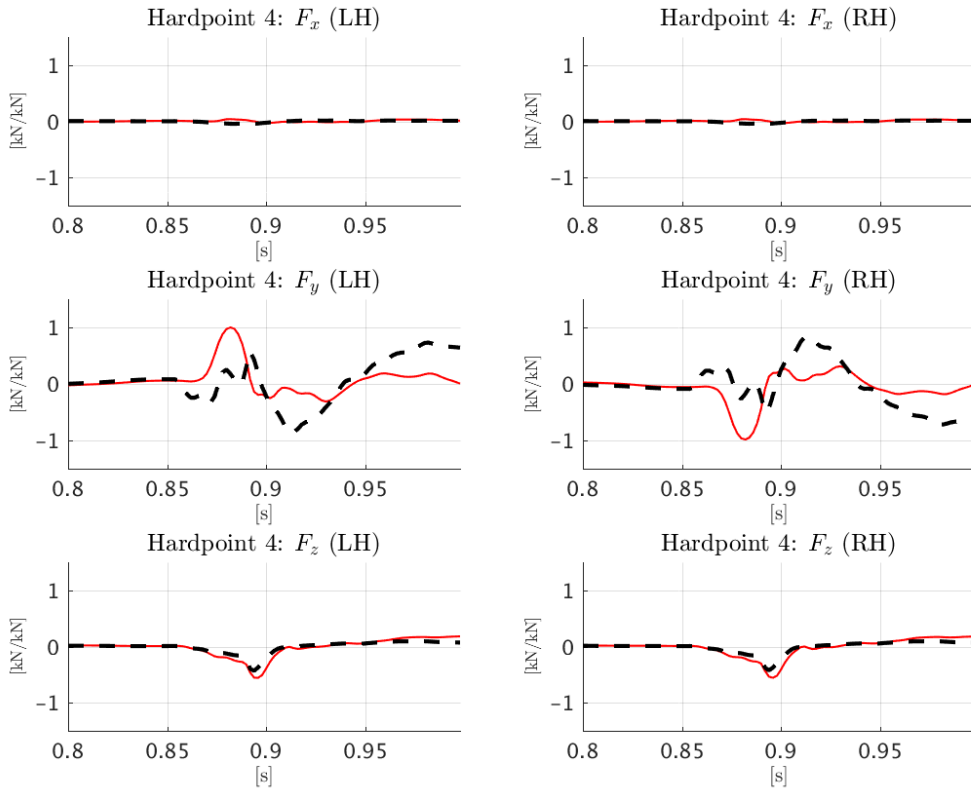


Figure B.13: F^{norm} in HP4 during DOC, FE-model (— —) vs RLD (—)

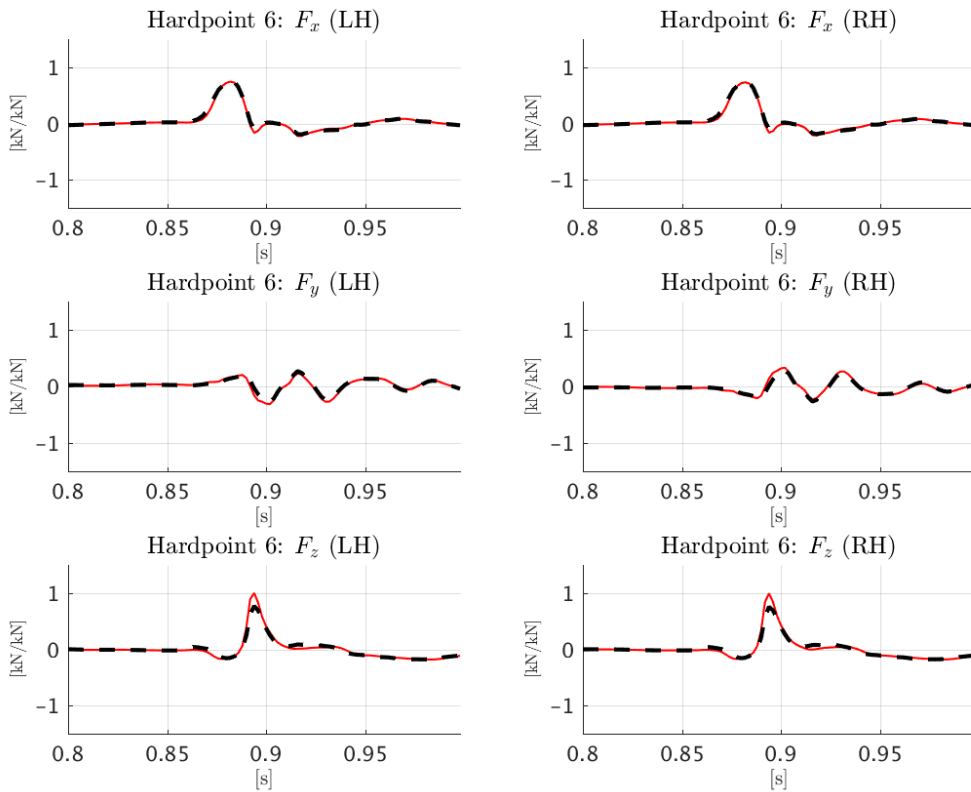


Figure B.14: F^{norm} in HP6 during DOC, FE-model (— —) vs RLD (—)

B. Results from verification of FE-model

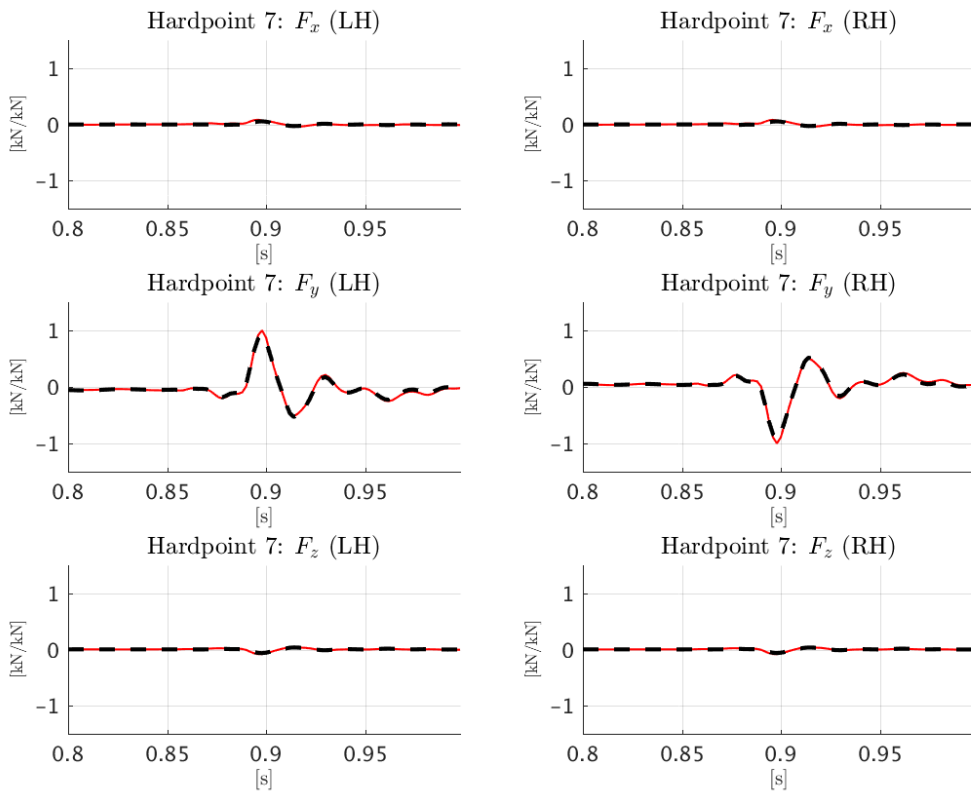


Figure B.15: F^{norm} in HP7 during DOC, FE-model (— —) vs RLD (—)

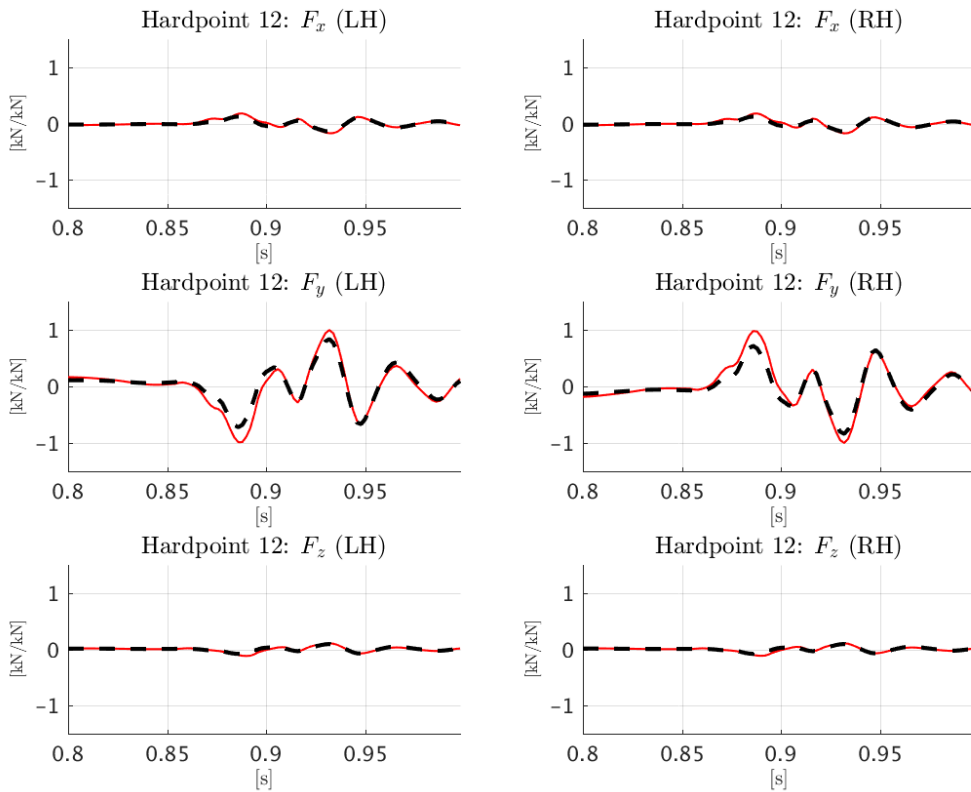


Figure B.16: F^{norm} in HP12 during DOC, FE-model (— —) vs RLD (—)

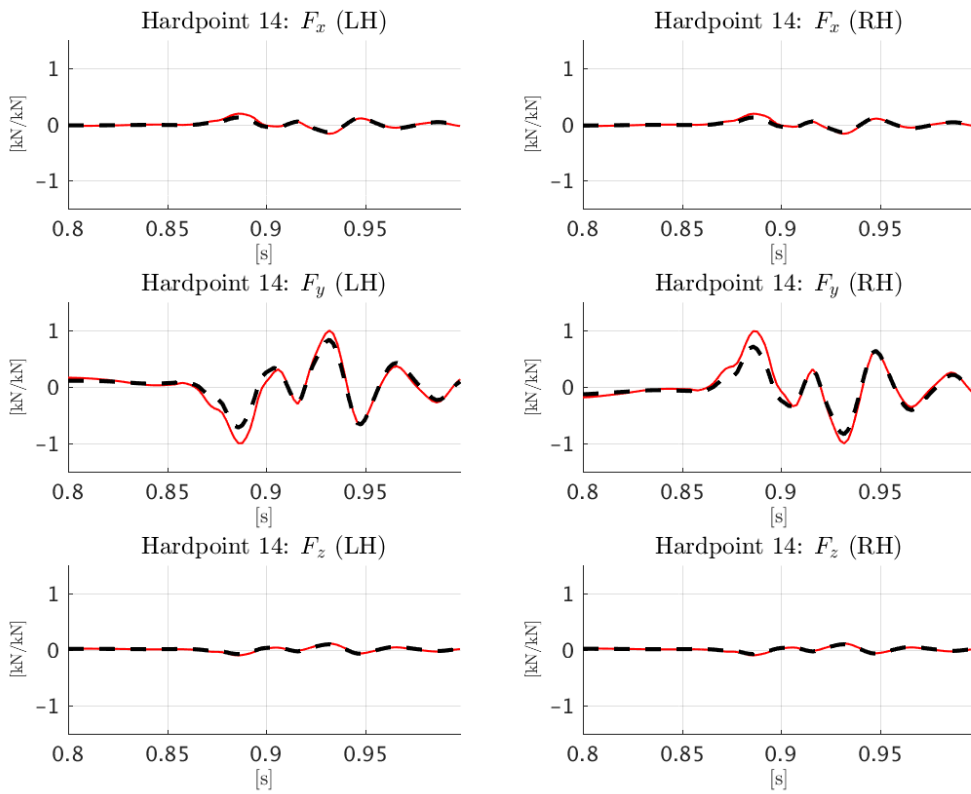


Figure B.17: F^{norm} in HP14 during DOC, FE-model (— —) vs RLD (—)

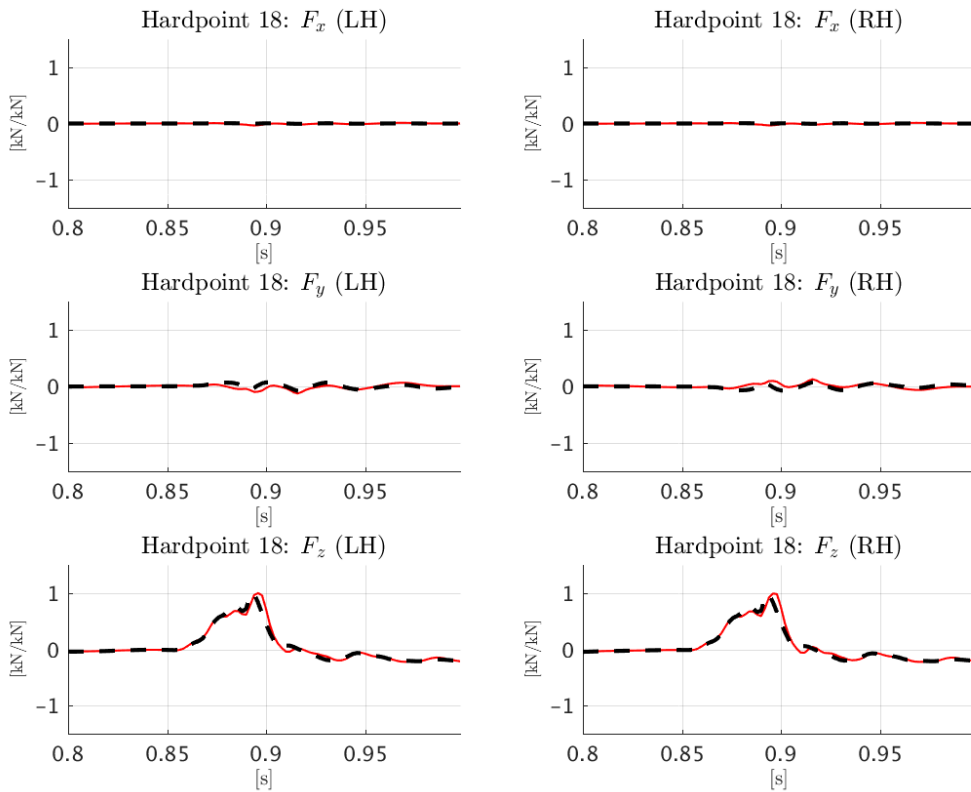


Figure B.18: F^{norm} in HP18 during DOC, FE-model (— —) vs RLD (—)

B. Results from verification of FE-model

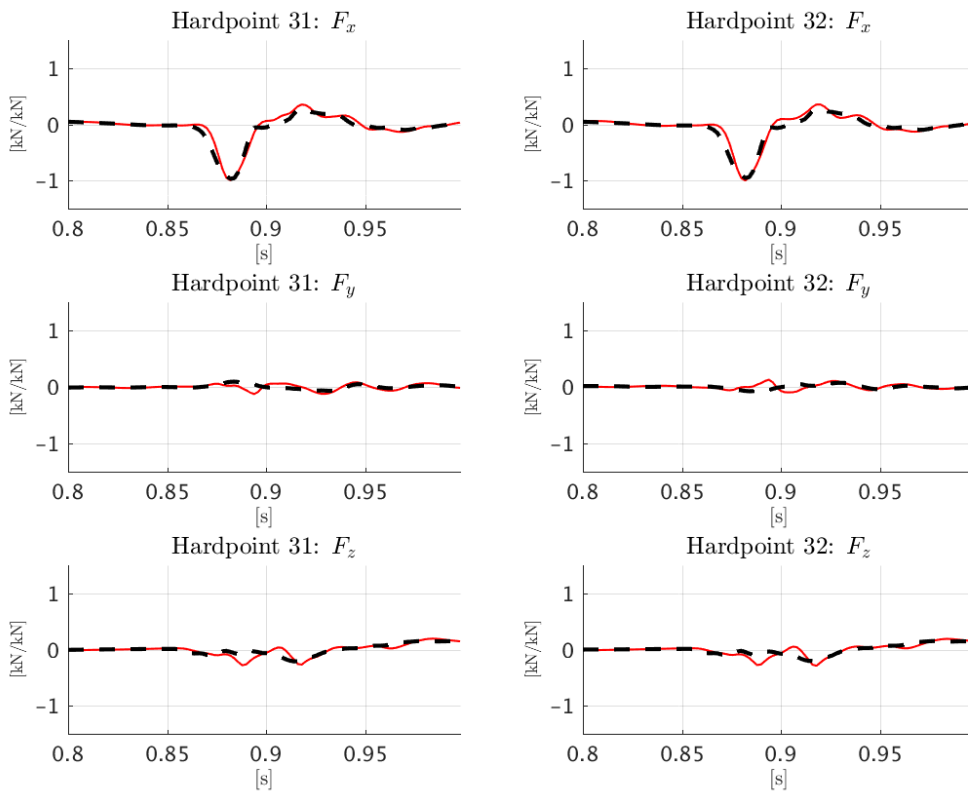


Figure B.19: F^{norm} in HP31-32 during DOC, FE-model (— —) vs RLD (—)

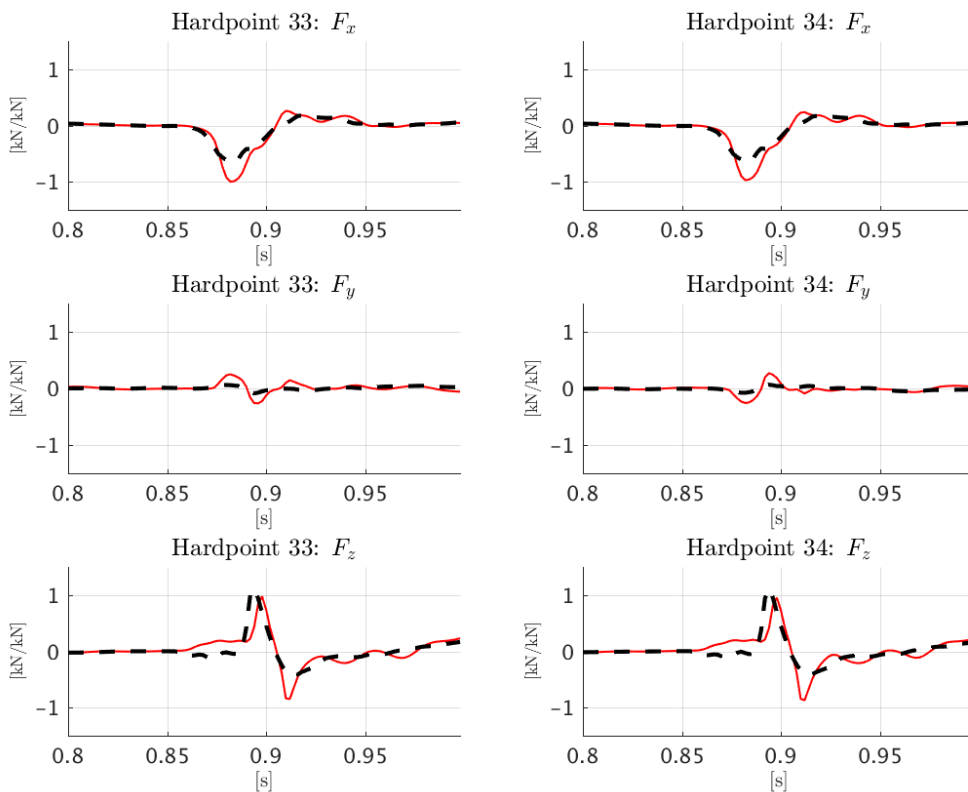


Figure B.20: F^{norm} in HP33-34 during DOC, FE-model (— —) vs RLD (—)

Figures B.21 - B.30 show the correlation plots for SAC and the corresponding RMS values are presented in Table B.5. Table B.6 shows a comparison between drawing state loads and pretension forces.

Table B.5: RMS^{norm} for all force signals during the SAC event, with subtraction of drawing state loads

Force HP	F_x^{LH}	F_y^{LH}	F_z^{LH}	F_x^{RH}	F_y^{RH}	F_z^{RH}
HP1	0.6 %	0.7 %	0.3 %	0.1 %	0.4 %	0.0 %
HP3	49.5 %	52.3 %	7.1 %	4.8 %	4.9 %	1.4 %
HP4	1.6 %	8.3 %	2.5 %	0.3 %	7.5 %	0.6 %
HP6	6.7 %	5.4 %	5.3 %	0.1 %	0.2 %	0.8 %
HP7	0.6 %	0.7 %	0.3 %	0.1 %	0.4 %	0.0 %
HP12	0.5 %	3.2 %	0.2 %	0.0 %	0.2 %	0.0 %
HP14	0.5 %	3.2 %	0.2 %	0.0 %	0.2 %	0.0 %
HP18	2.8 %	9.4 %	8.3 %	0.2 %	0.7 %	0.5 %
HP31-32	8.6 %	8.4 %	0.9 %	5.8 %	1.5 %	1.4 %
HP33-34	3.5 %	9.9 %	13.0 %	2.0 %	11.0 %	3.6 %
Mean	7.5 %	10.2 %	3.8 %	1.3 %	2.7 %	0.8 %

Table B.6: Comparison of mean RMS^{norm} during SAC

Method \ Force	F_x^{LH}	F_y^{LH}	F_z^{LH}	F_x^{RH}	F_y^{RH}	F_z^{RH}
Drawing state loads	7.5 %	10.2 %	3.8 %	1.3 %	2.7 %	0.8 %
Pretension forces	8.0 %	10.4 %	4.4 %	1.6 %	2.9 %	1.1 %

B. Results from verification of FE-model

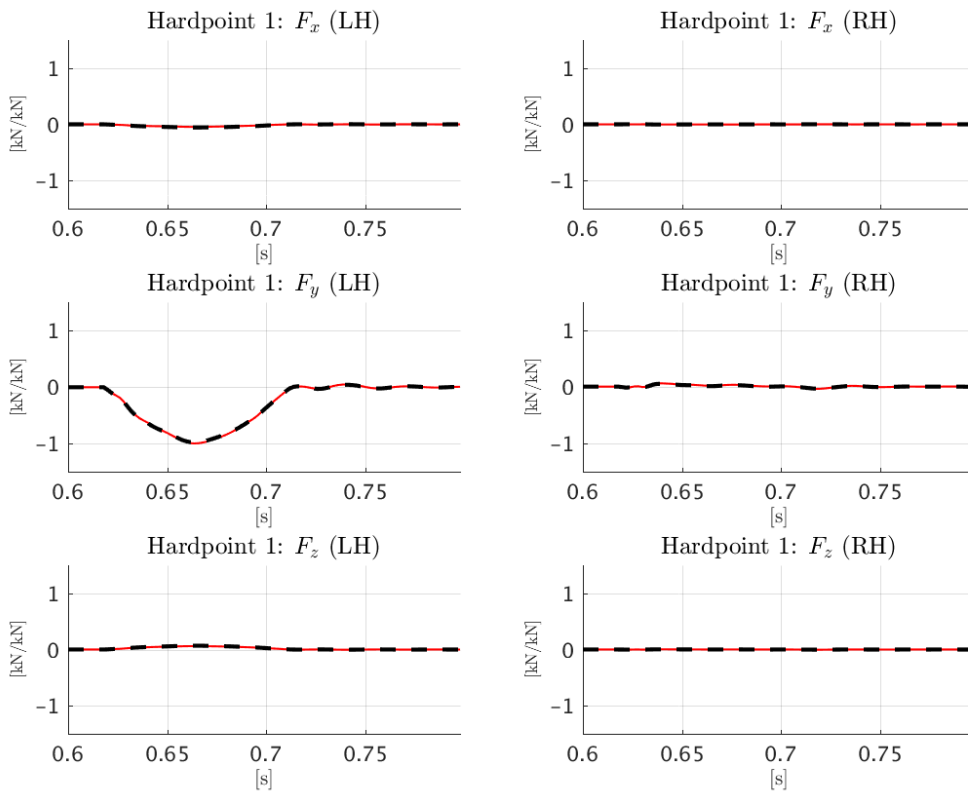


Figure B.21: F^{norm} in HP1 during SAC, FE-model (— —) vs RLD (—)

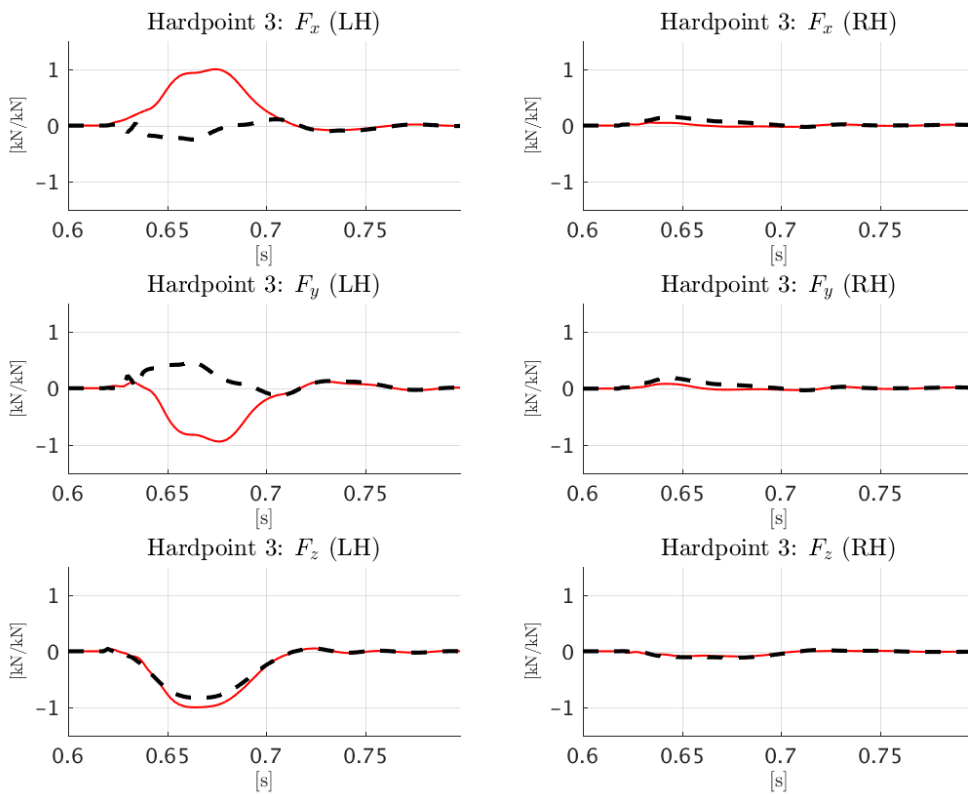


Figure B.22: F^{norm} in HP3 during SAC, FE-model (— —) vs RLD (—)

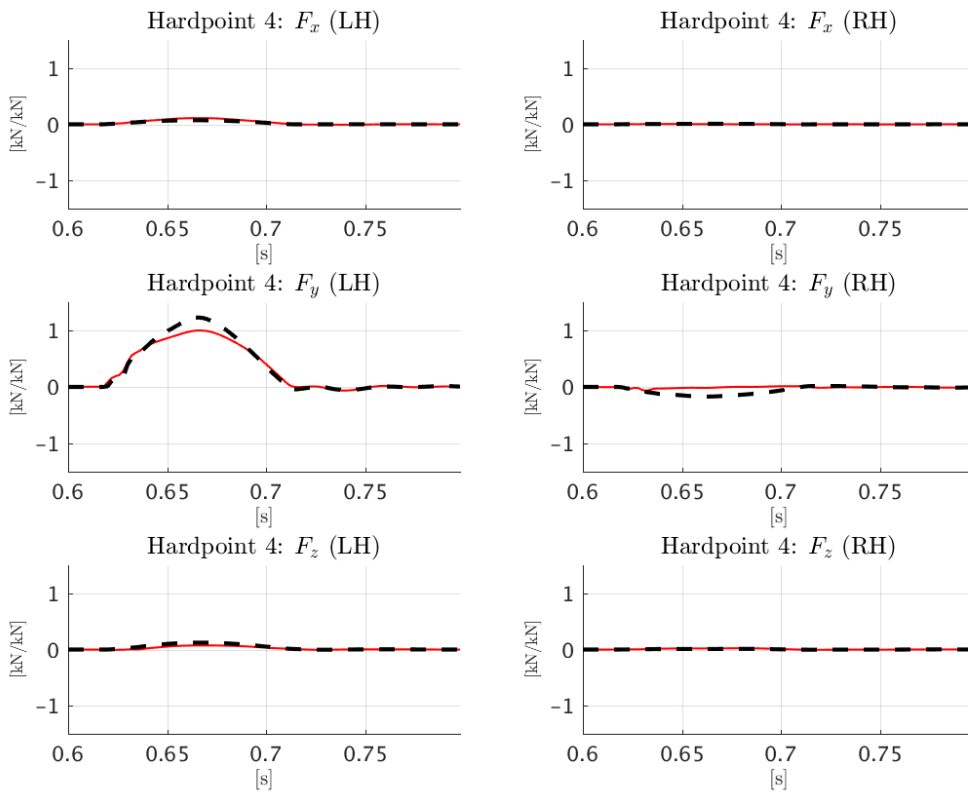


Figure B.23: F^{norm} in HP4 during SAC, FE-model (— —) vs RLD (—)

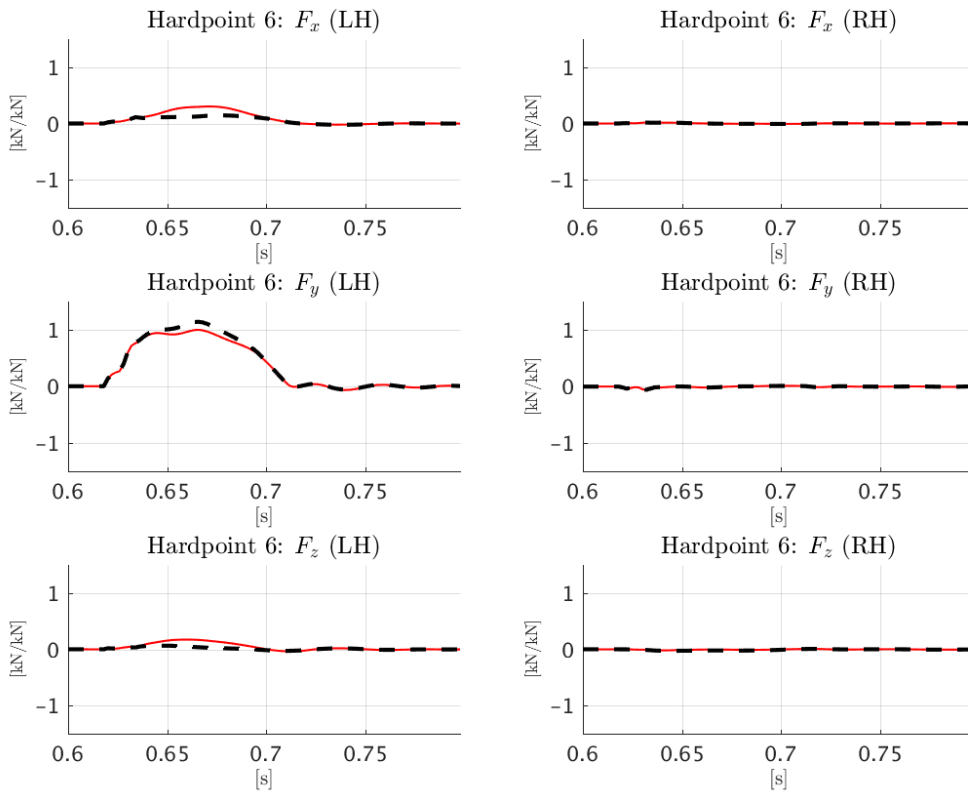


Figure B.24: F^{norm} in HP6 during SAC, FE-model (— —) vs RLD (—)

B. Results from verification of FE-model

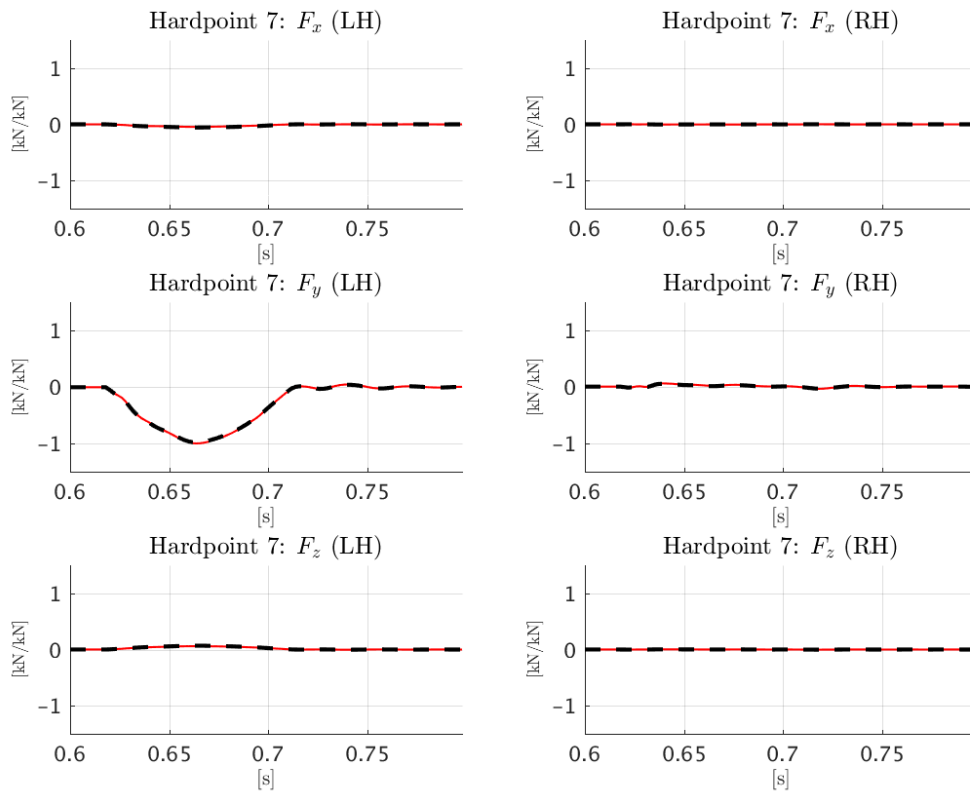


Figure B.25: F^{norm} in HP7 during SAC, FE-model (— —) vs RLD (—)

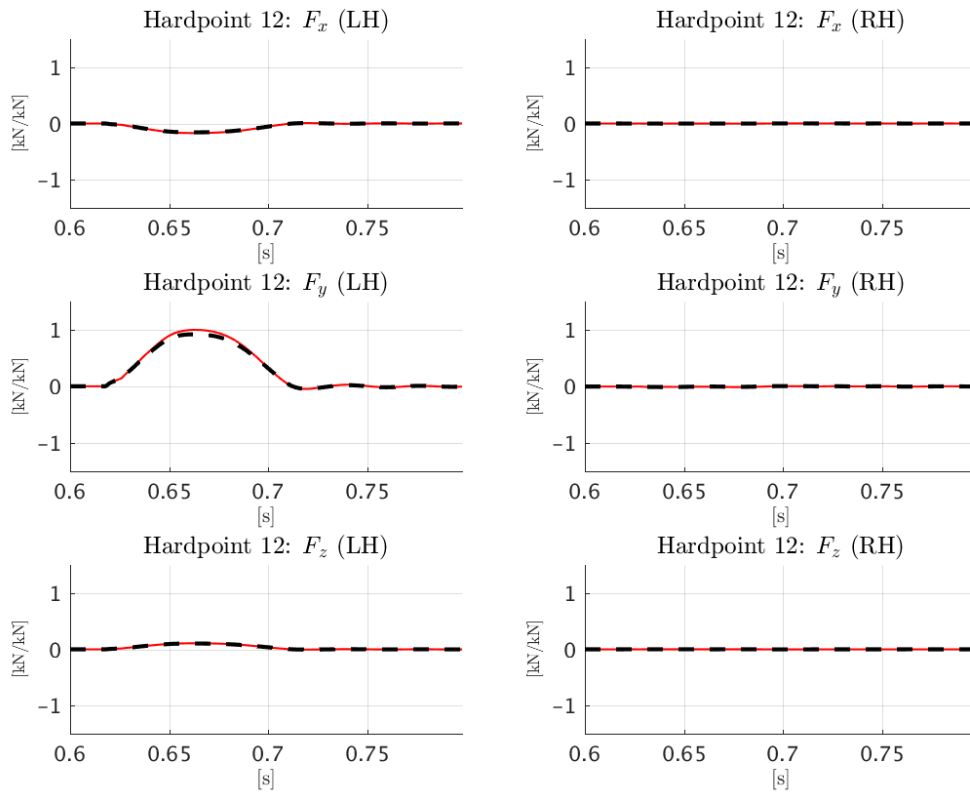


Figure B.26: F^{norm} in HP12 during SAC, FE-model (— —) vs RLD (—)

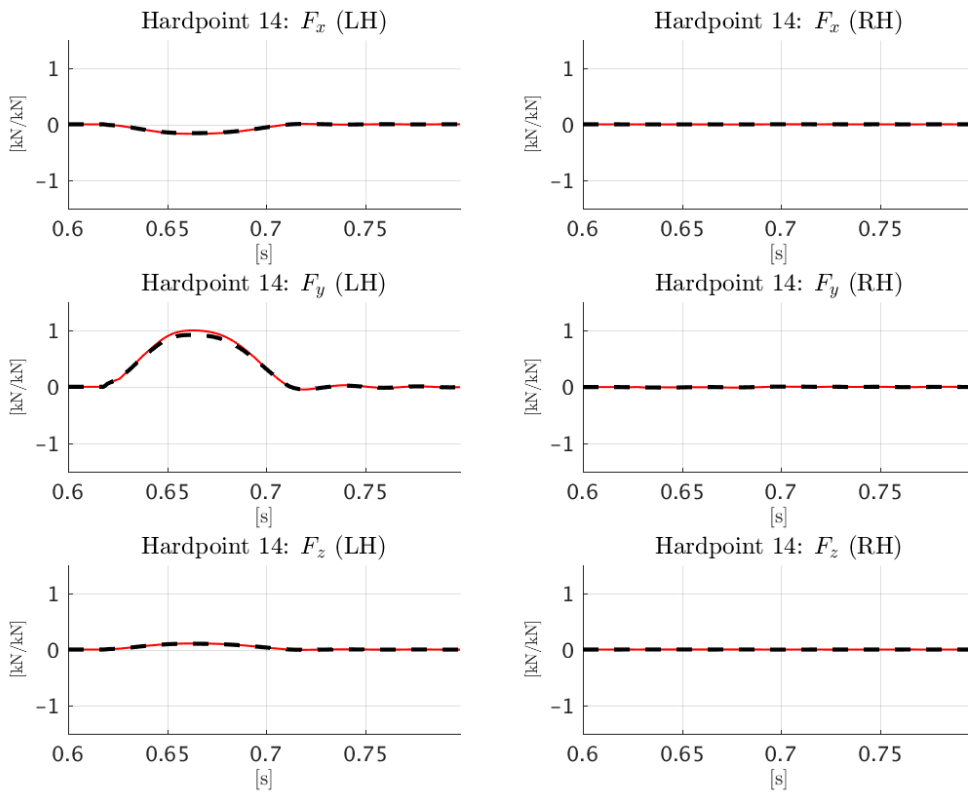


Figure B.27: F^{norm} in HP14 during SAC, FE-model (— —) vs RLD (—)

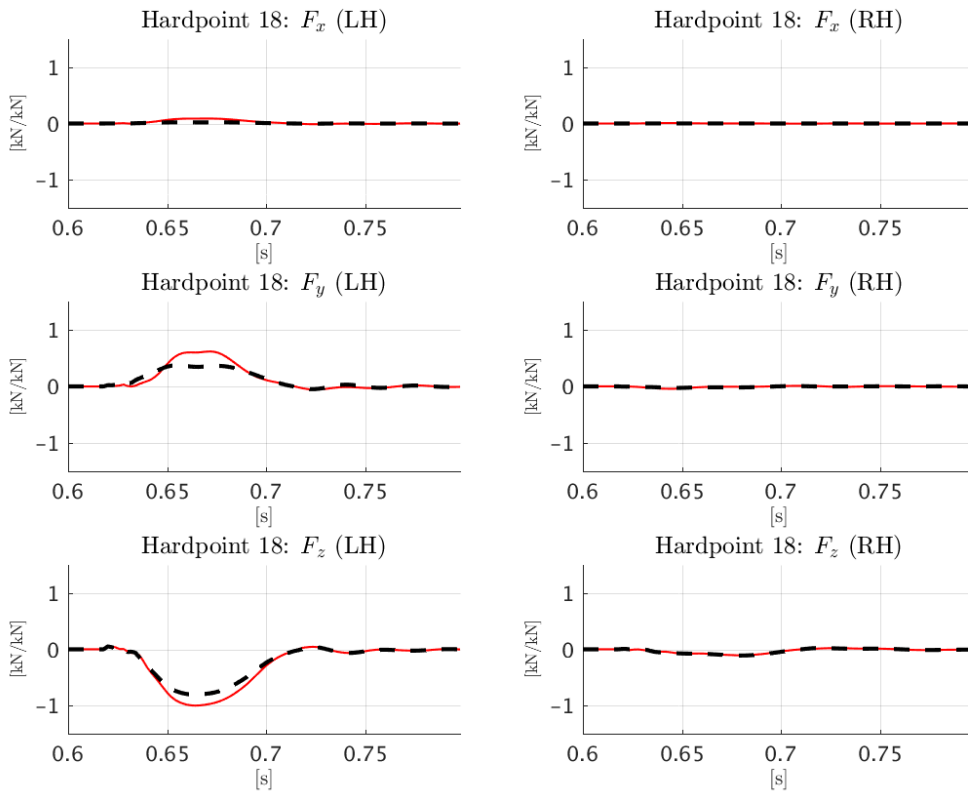


Figure B.28: F^{norm} in HP18 during SAC, FE-model (— —) vs RLD (—)

B. Results from verification of FE-model

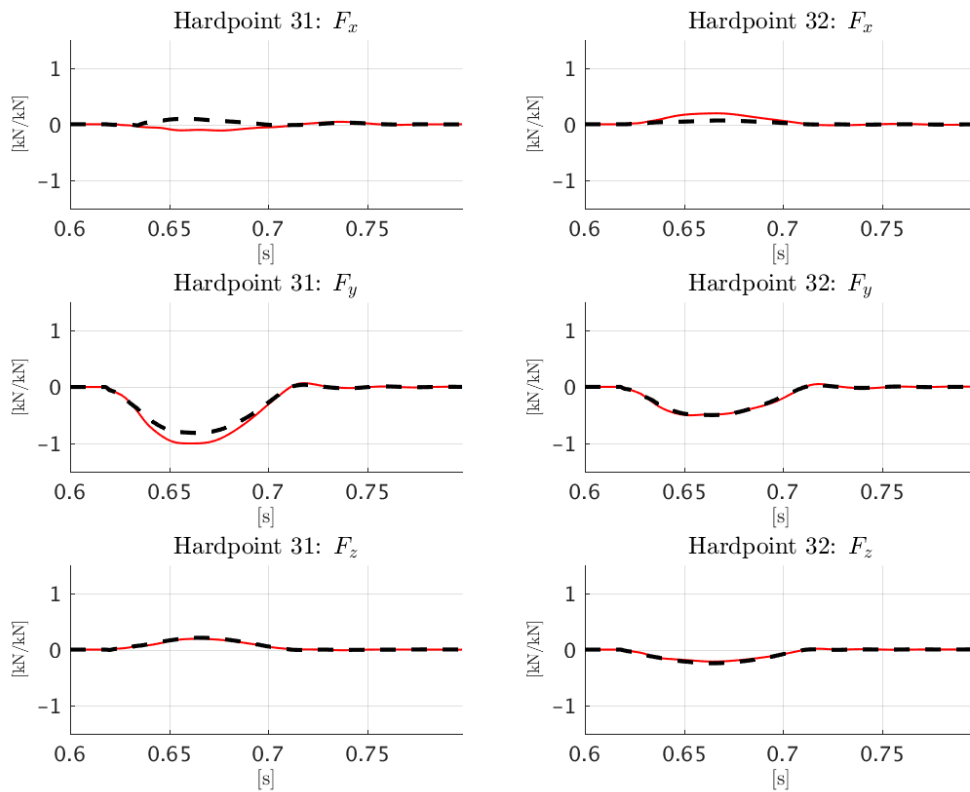


Figure B.29: F^{norm} in HP31-32 during SAC, FE-model (— —) vs RLD (—)

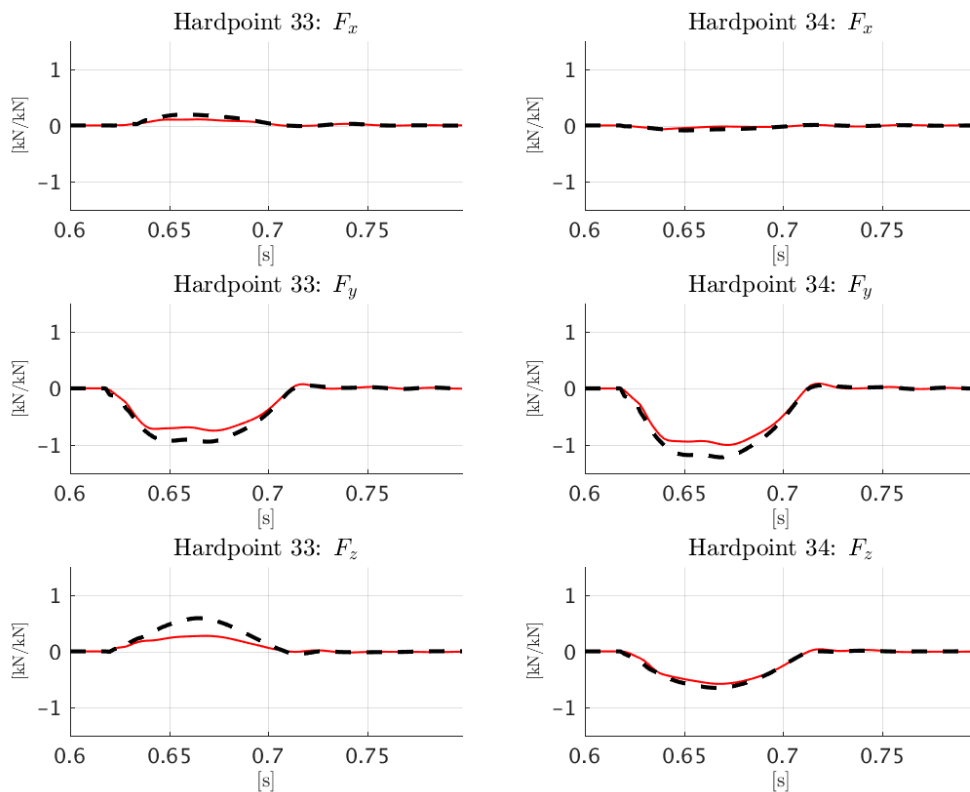
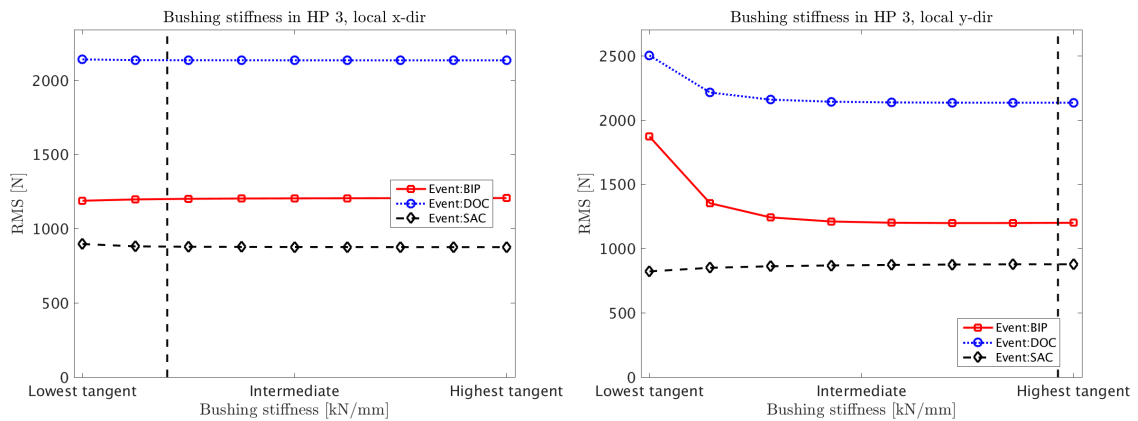


Figure B.30: F^{norm} in HP33-34 during SAC, FE-model (— —) vs RLD (—)

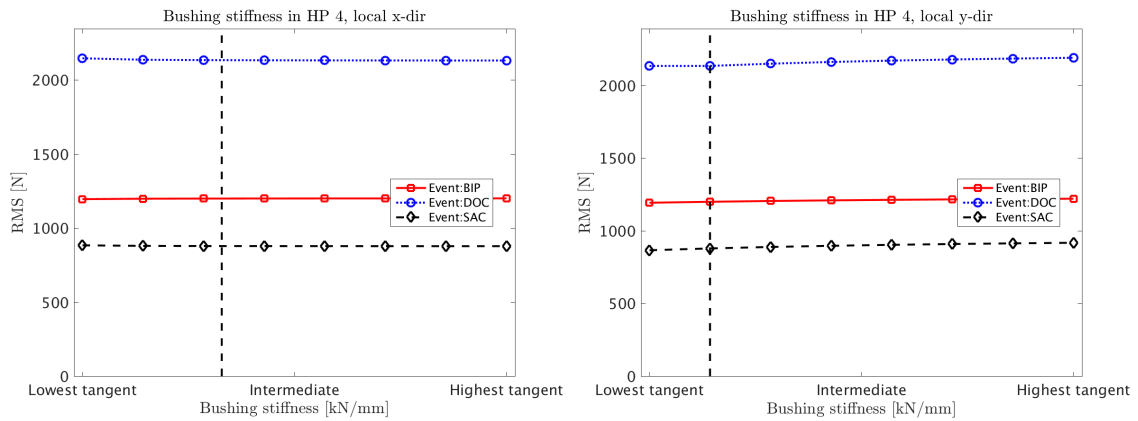
C

Results from sensitivity analysis: bushing stiffness



(a) $\text{RMS}^{\text{Event}}$ vs K_x in HP3

(b) $\text{RMS}^{\text{Event}}$ vs K_y in HP3

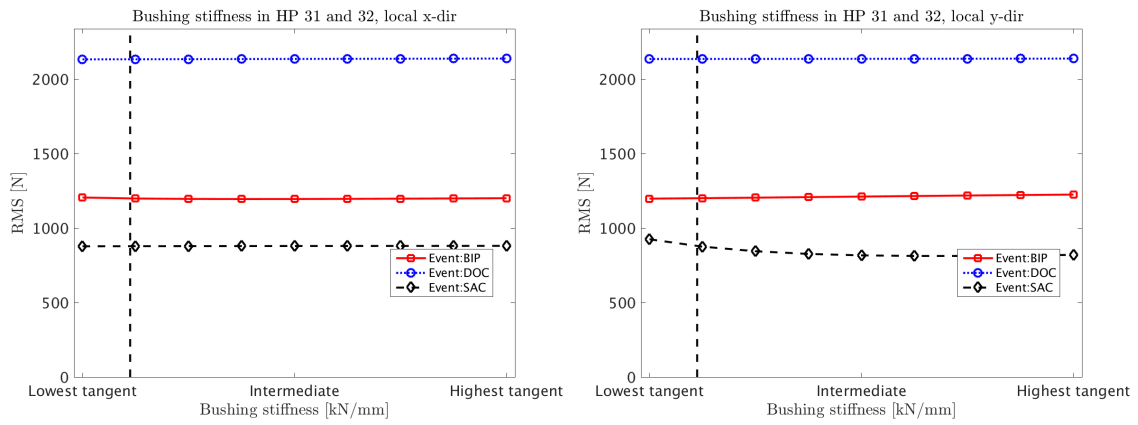


(c) $\text{RMS}^{\text{Event}}$ vs K_x in HP4

(d) $\text{RMS}^{\text{Event}}$ vs K_y in HP4

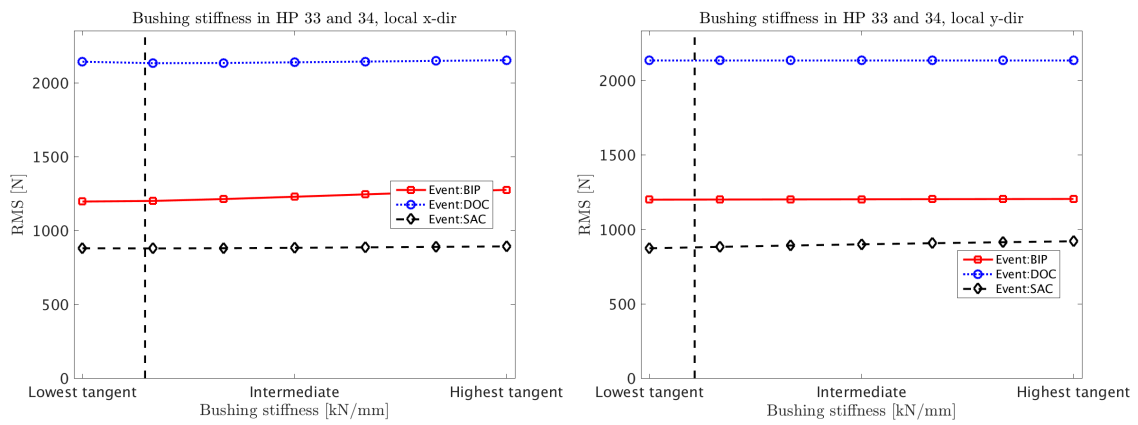
Figure C.1: Sensitivity analysis of bushing stiffness in HP3 and HP4 showing $\text{RMS}^{\text{Event}}$ vs bushing stiffness for all events

C. Results from sensitivity analysis: bushing stiffness



(a) $\text{RMS}^{\text{Event}}$ vs K_x in HP31-32

(b) $\text{RMS}^{\text{Event}}$ vs K_y in HP31-32



(c) $\text{RMS}^{\text{Event}}$ vs K_x in HP33-34

(d) $\text{RMS}^{\text{Event}}$ vs K_y in HP33-34

Figure C.2: Sensitivity analysis of bushing stiffness in HP31-32 and HP33-34 showing $\text{RMS}^{\text{Event}}$ vs bushing stiffness for all events

D

Additional Results from TO of the system model

Here the results from the topology optimization defined in Table 3.1 for the three individual load cases are presented. The topology of the components with load case BIP are shown in Figure D.1, with load case DOC in Figure D.2 and with load case SAC in Figure D.3.

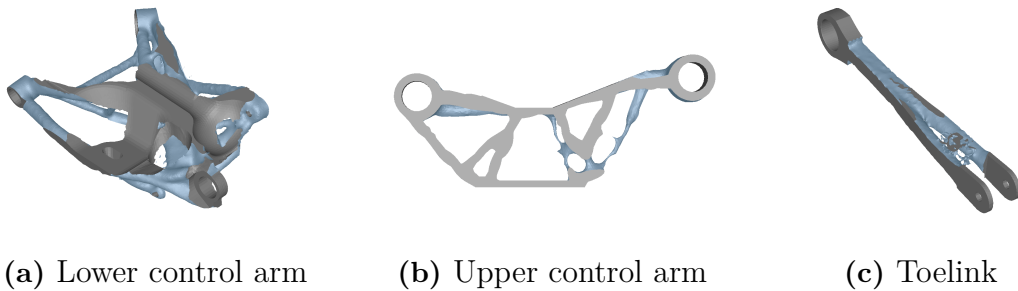


Figure D.1: Topology of the optimized components for case 1 with only BIP

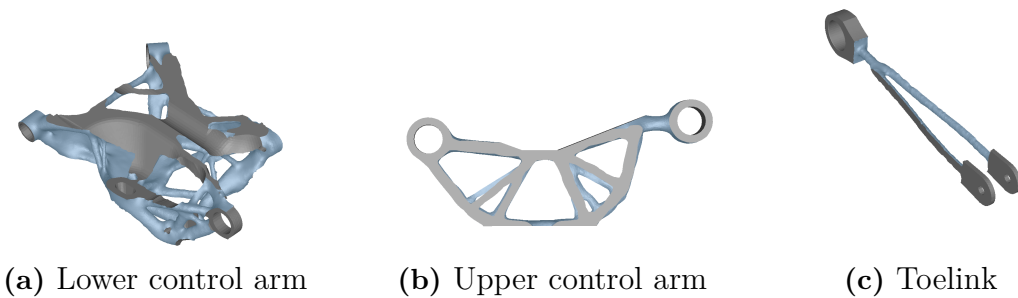


Figure D.2: Topology of the optimized components for case 1 with only DOC

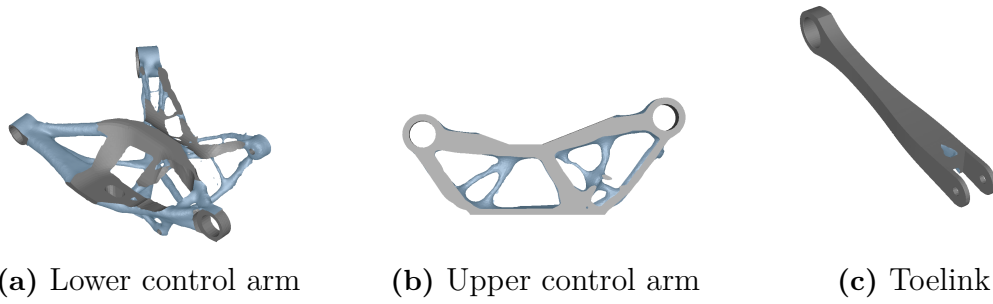


Figure D.3: Topology of the optimized components for case 1 with only SAC

In Figure D.4 the topology of the LCA is presented for each mass constraint iteration and in Figure D.5 and D.6 the corresponding is presented for the UCA and the toelink.

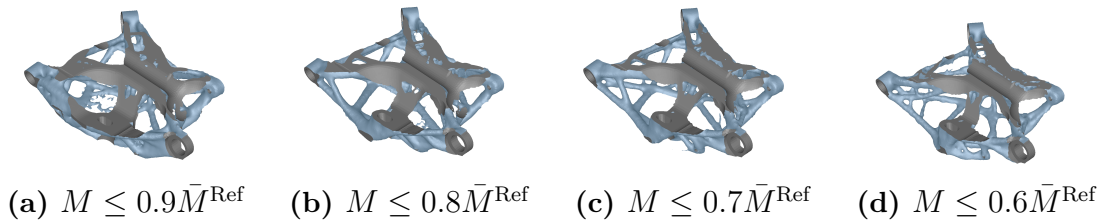


Figure D.4: Topology of the optimized LCA with $M \leq [0.6 - 0.9]\bar{M}^{\text{Ref}}$

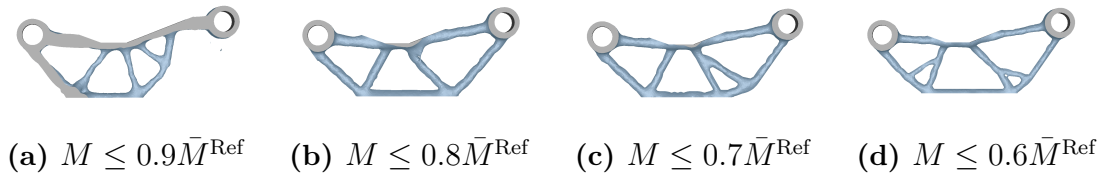


Figure D.5: Topology of the optimized UCA with $M \leq [0.6 - 0.9]\bar{M}^{\text{Ref}}$

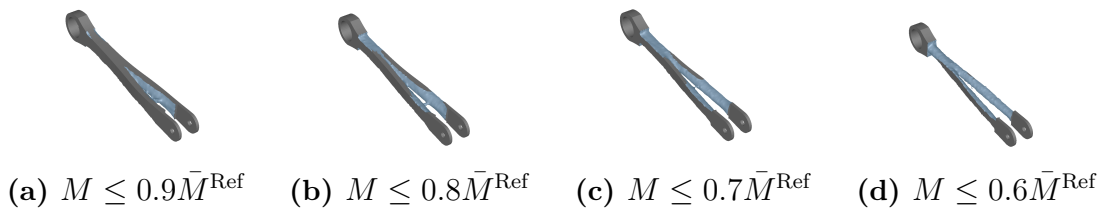


Figure D.6: Topology of the optimized Toelink with $M \leq [0.6 - 0.9]\bar{M}^{\text{Ref}}$

E

Proposed workflow for development

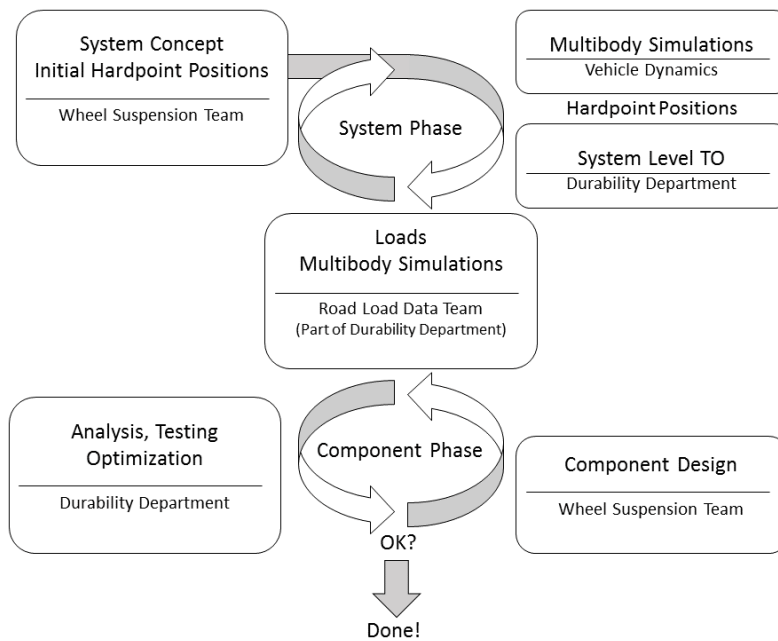


Figure E.1: Proposed workflow